UNIVERSIDAD DE ALCALÁ

ESCUELA POLITÉCNICA SUPERIOR

DEPARTAMENTO DE ELECTRÓNICA

TESIS DOCTORAL

"Ultra-Long Range Brillouin Optical Time Domain Analysis"

Xabier Angulo Vinuesa

2014

UNIVERSIDAD DE ALCALÁ

ESCUELA POLITÉCNICA SUPERIOR

DEPARTAMENTO DE ELECTRÓNICA

"Ultra-Long Range Brillouin Optical Time Domain Analysis"

Autor

Xabier Angulo Vinuesa

Directores

Dra. Sonia Martín López
Dr. Miguel González Herráez

2014

TESIS DOCTORAL

Agradecimientos

En primer lugar, me gustaría agradecer a las dos personas que hicieron posible mi llegada al grupo de investigación CSIC-UAH y que sin su intermediación, todo este trabajo no hubiera sido posible. Me refiero al Dr. Miguel González-Herráez, por haberse tomado la molestia de leer el e-mail que envié allá por abril año 2010 buscando desesperadamente hueco en un grupo de investigación y, al Dr. Pedro Corredera, quien aceptó acogerme y financiarme incluso después de mi sincera respuesta a su pregunta acerca de los sensores distribuidos Brillouin y Raman. Evidentemente, este agradecimiento inicial no sería en absoluto completo si no incluyo a la persona que considero más me ha ayudado, enseñado y guiado a lo largo de estos cuatro años, la Dra. Sonia Martín-López. A los tres, os quiero trasladar un agradecimiento realmente sincero y excepcional por vuestro constante apoyo y trabajo.

En segundo lugar, quisiera trasladar mi agradecimiento a todos los estamentos e instituciones que me han financiado y facilitado los medios para poder desarrollar esta tesis doctoral de manera satisfactoria bajo unas condiciones verdaderamente privilegiadas y excepcionales: a la empresa ICYFSA, al Instituto de Física Aplicada del CSIC, al proyecto de investigación de la Comunidad de Madrid FACTOTEM-2, al Instituto de Óptica del CSIC a través de su antigua directora, la Dra. Susana Marcos, y su actual director, el Dr. Joaquín Campos, a la empresa Omnisens a través de los Dres. Etienne Rochat y Mark Niklés, al Departamento de Electrónica de la UAH a través de su directora, la Dra. Sira Palazuelos y a la empresa FOCUS. Asimismo, es de recibo extender estos agradecimientos al Prof. Pascal Szriftgiser, por acogerme con inmensa hospitalidad en sus laboratorios en mi breve estancia realzada en la Universidad Lille 1 (Francia). Quisiera, del mismo modo, dar un agradecimiento especial al Prof. Luc Thévenaz, una verdadera eminencia en el campo de los sensores distribuidos de fibra óptica, por el excelente trato que me ha otorgado en mis estancias en el EPFL de Lausanne (Suiza), así como sus sabios consejos y comentarios.

No me gustaría pasar por alto la inestimable colaboración del Dr. Marcelo Soto en una de mis estancias en el EPFL. Quisiera mencionar lo muchísimo que he aprendido acerca de sensores distribuidos de fibra óptica gracias a sus extensos conocimientos y remarcar el verdadero placer que ha supuesto haber compartido horas de trabajo. Asimismo, no quiero dejar de mencionar la inestimable colaboración del Dr. Juan Diego Ania-Castañon en sus excelentes trabajos de simulación que han sido aplicados en muchos de los resultados obtenidos.

Es obligatorio agradecer a todos los miembros del tribunal por ceder parte de su valioso tiempo a la evaluación y rigurosa lectura del trabajo de tesis: los Dres. José Capmany, Fernando Naranjo, Luc Thévenaz, Manuel López-Amo, Carmen Vázquez, Pedro Corredera y Óscar Esteban.

En igual medida, quisiera intentar nombrar a todas las personas que he conocido a lo largo de esta aventura y que han contribuido de manera desinteresada a que muchas veces no desistiese en el empeño: a mis compañeros de despacho del CSIC Ayalid, Manuela, Antonio, Sergio, Luis, Berta y Elisa; a mis antiguos compañeros de grupo del CSIC Massimo, Pedro Mex, Javi, Ana y Juan; al genial Grupo de Comunicaciones Ópticas de la Universidad Pública de Navarra, que siempre me ha tratado como a uno más y con el que me lo he pasado en grande en los diferentes congresos en los que hemos coincidido y en las breves visitas que he realizado a su centro de investigación: Rosana, Ander, Sergio, Dani, Javi, Alayn, Patxi, Manolo, Ana Margarida, Montse y en especial a Mikel; a los integrantes del GFO del EPFL que hicieron mis estancias es Suiza realmente agradables: Andrey, Nikolay, SangHoon y Alexandra.

No me quiero olvidar de Alexia, Alejandro y Hugo. Sin su inestimable ayuda no hubiera sido capaz de finalizar el desarrollo del prototipo de sensor de fibra en el que he estado trabajando en los últimos meses. Asimismo, quisiera agradecer al resto de miembros del grupo de Fotónica de la Universidad de Alcalá, Laura, Arantxa, Oscar, Fernando, Juan y Marco, por acogerme tan bien en el grupo en esta última fase de mi investigación.

Me gustaría reservar unas líneas de agradecimiento especial a toda mi familia y amigos por su apoyo incondicional tanto en las buenas como en las malas decisiones que he tomado a lo largo de mi vida personal y profesional. Mila esker danoi bihotz bihotzetik! ¡Muchas gracias a todos de todo corazón!

Y por último, quiero dar un sentido y especial agradecimiento a Marta, ya que sin su constante apoyo nada de esto tendría sentido ni hubiera sido posible. Gracias por aguantarme. ¡Eres la mejor!

Resumen

Nuestro estilo de vida actual, basado en la industrialización y el consumo, requiere de grandes infraestructuras que puedan dar servicio a todas las necesidades asociadas al entorno: autopistas, líneas ferroviarias de alta velocidad, presas, gasoductos, oleoductos, estaciones de aerogeneración, líneas de alta tensión, etc. Evidentemente, la seguridad de las citadas estructuras es una prioridad ya que decenas, cientos, e incluso miles de vidas pueden estar en riesgo en caso de accidente.

Ese creciente requisito en términos de seguridad, está aumentando de manera considerable el desarrollo y aplicación de sensores de fibra óptica en detrimento de los típicos sensores eléctricos. Este reemplazo se debe a ciertas ventajas que tienen los dispositivos basado en fibra óptica: pequeño tamaño y ligereza, menor coste, baja atenuación, capacidad de multiplexación, inmunidad al ruido electromagnético o resistencia a temperaturas extremas.

Evidentemente, no todos los sensores de fibra óptica son aplicables a cualquier tipo de estructura o aplicación. En el campo de las grandes infraestructuras ($>$ 25-30 km), los sistemas de fibra basados en la tecnología BOTDA (Brillouin Optical Time Domain Analysis) están tomando cada vez mayor protagonismo debido a sus cualidades en rango de medida ($>$ 50 km) y resolución ($<$ 10 m). Este tipo de sensores, denominados distribuidos por su capacidad de "convertir" cada sección de fibra en un sensor simplemente introduciendo luz por ambos extremos de la propia fibra, proporcionan información de variaciones de temperatura y deformación, y por consiguiente de cualquier magnitud asociada a ambas.

La necesidad de introducir dos señales de luz en la fibra objetivo dificulta la aplicación de este tipo de sistemas en ciertas infraestructuras de muy larga distancia ($>$ 100 km), donde la fibra tenga que ir y volver a la estación de sensado ($>$ 200 km) sin posibilidad de que la luz sea amplificada por algún elemento intermedio. Además, cada vez se demanda más la posibilidad de monitorizar grandes estructuras ($>$ 100 km) con resoluciones por debajo del metro, lo que dificulta considerablemente la implementación de los sistemas BOTDA.

En este trabajo de tesis, se desarrolla un estudio cuidadoso de todos los problemas asociados al incremento de distancia y resolución en sistemas BOTDA y, consecuentemente, se proponen técnicas aplicables para evitarlos. En particular, abordaremos en profundidad los desafíos y las constantes de diseño de los sistemas BOTDA asistidos por Raman.

La amplificación Raman en sistemas BOTDA implica un aumento del rango de sensado pero, desgraciadamente, introduce un ruido en la señal detectada denominado RIN (Relative Intensity Noise). Para evitar los problemas asociados a la transferencia de RIN, propondremos diferentes métodos capaces de eliminar parcialmente las características típicas del ruido RIN.

Gracias a la aplicación de estas nuevas técnicas y procedimientos de optimización, se demuestra de manera experimental el sensado a lo largo de 100 km con 0,5 metros de resolución y, por primera vez, una medición lineal de 240 km de fibra (120 km de fibra sensible) con una resolución de 5 metros.

Abstract

Our current lifestyle, based on industrialization and consume, requires big infrastructures that can provide service to all the generated associated necessities: freeways, high-speed railways, dams, pipeline transport for oil and gas, wind farms, high power lines, etc. Obviously, the safety of the cited structures is a priority since tens, hundreds, or even thousands of lives are at risk in case of accident.

That increasing requirement in terms of security is enlarging considerably the development and application of optical fiber sensors in detriment of the standard electric sensors. This replacement arises due to the advantages that optical fiber devices have: reduced size and weight, low cost, small attenuation, multiplexing ability, immunity to electromagnetic noise or resistance to extreme temperatures.

Obviously, not any optical fiber sensor is suitable for all kind of structures or applications. In the field of big infrastructures ($>$ 25-30 km), systems based on Brillouin Optical Time Domain Analysis (BOTDA) technology are becoming more prominent due to their attributes in terms of range ($>$ 50 km) and resolution ($<$ 10 m). These kind of sensors, denominated as distributed because of their ability to "convert" every section of the fiber into a sensor by just introducing light on each side of the fiber itself, provide information of temperature and strain variations and, therefore, of any other associated magnitude.

The necessity to introduce two light signals on the target fiber, makes difficult the application of these kind of systems over very long range infrastructures ($>$ 100 km) where the fiber has to go back and forth to the sensing unit ($>$ 200 km) without being possible to amplify the light by any intermediate element. Also, the demand for monitoring large structures ($>$ 100 km) with sub-metrical resolutions is considerably increasing, which considerably complicates the implementation of BOTDA systems.

In this thesis work we develop a careful study of all the associated issues to the increment of range and resolution in BOTDA systems and, consequently, we propose applicable techniques to avoid them. In particular we will address in depth the challenges and design constants of Raman assisted BOTDA systems.

Raman amplification in BOTDA implies some increase in sensing range but, unfortunately, introduces a noise on the detected signal known as Relative Intensity Noise (RIN). To avoid the issues related to RIN transfer, we will propose different methods capable of partially removing typical RIN noise features.

Thanks to the application of these new techniques and optimization procedures, it is experimentally proven the sensing over 100 km with 0.5 meter resolution and, for the first time, a linear measurement of 240 km fiber length (120 km sensing length) with 5 meter resolution.

Contents

List of Figures

Chapter 1

Introduction

1.1 Motivation

The scientific progress developed from the beginning of the 20^{th} century, has allowed to supply our society with different structures/infrastructures that make our daily life much more comfortable. In the industrialized countries, it is common to find infrastructures such as freeways, skyscrapers, high-speed railways, dams, dikes, etc. Moreover, the current lifestyle, mainly based in consume, demands the production and transport of large amounts of energy, which at the same time require pipeline transport for oil and gas, high power lines, wind farms, solar power stations, etc.

Because of the importance that these structures have in our daily routine, it is necessary to control their safety and efficiency since hundreds or even thousands of lives depend on them. In order to develop that monitoring, until the end of the 20^{th} century, the use of electrical sensors has been widely developed. Unfortunately, this kind of sensing has some associated issues especially when dealing with some specific and/or large structures:

- In large structures, where the sensors heads and the interrogation units are usually far from each other, when electric cables are employed to communicate both elements they transfer noise to the signal and also a great amount of attenuation, thus limiting the maximum distance among the sensing elements.
- If hundreds or thousands of sensing points are required due to the size of the target structure, the conventional electric sensors require a couple of cables per sensing head, which is translated as complex, heavy, difficult to handle and expensive systems.
- Some environments, such as rail transport infrastructures, are highly affected by electromagnetic interferences due to the intense electric fields generated during train motion. These kind of interactions directly influence the measuring quality of the electric sensors, which is translated as bad readings that may cease the activity of the infrastructure inappropriately.
- The electrical monitoring systems are sensitive to environmental variations, so the hostile nature of some surroundings can easily damage their lifetime if they are not properly installed or protected.

Due to the cited drawbacks, sometimes it is quite difficult or even impossible to continuously monitor some of the infrastructures. This could lead to serious accidents or the necessity to apply some other more expensive controlling techniques. Under such circumstances, in the 90's, the development of sensors based on optical fibers started in order to take advantage of the benefits of light guiding structures:

- Standard optical fibers present very low attenuation values (from 0.20 dB/km to 0.35 dB/km), which means that the target signal can be transported over very long distances without distorting its features.
- The sensors based on optical fibers can be wavelength-multiplexed in a relatively easy way, which allows a single fiber to monitor tens or even of hundreds of points. In addition, the fiber itself can act as distributed sensor, which allows to control tens of kilometers with resolutions in the order of meters.

- Optical fibers are immune to electromagnetic noise, which favors their installation in environments affected by intense electric fields, such as rail transport infrastructures.
- Since optical fibers are based on silica, they have great resistance to high or low temperatures. This feature makes optical fibers very useful when measuring under extreme environmental conditions.

All the cited benefits, have converted the monitoring and control of large infrastructures through optical fiber sensors in one of the most preferred options for different companies. In fact, the standard optical fiber installation for data transmission present over new constructed facilities can be, sometimes, potentially employed for sensing purposes.

Among the different sensors based on optical fibers that are currently applied in real-world applications, we can find the Bragg gratings and the ones based on linear or non-linear scattering processes, such as Rayleigh, Raman or Brillouin scattering. Bragg gratings reflect a temperature/strain-dependent light wavelength and can be multiplexed over the target fiber. The sensors based on linear or non-linear scattering have the special ability to obtain temperature and strain measurements every few meters over a conventional fiber, which allows to sense over very long distances providing a large amount of sensing points. Among the distributed sensors, the ones based on Brillouin scattering stand out due to their good performance in terms of range and resolution.

One of the most studied and developed Brillouin distributed sensor is the one based on analyzing the retrieved information as a function of time. This element is known as BOTDA, acronym that comes from Brillouin Optical Time Domain Analysis. A BOTDA, proposed for the first time in 1989, has attracted great interest in the lasts decades among the academic and industrial sectors due to its benefits when targeting very long distances ($>$ 25-30 km) with resolutions ranging a few meters ($<$ 10 m). As a result of this intense interest on these systems, the demand in terms of range and resolution has considerably increased. Some applications require ranges exceeding 100 km with, in some cases, sub-metrical resolutions. In addition, some applications such as offshore wind farms, require to monitor distances beyond 70 km with the impossibility to connect any electrical amplification stage at the furthest point since no electrical power supply is present on the installation. This means that it is necessary to monitor fiber spans beyond 140 km going forth and back from the sensing unit.

This thesis dissertation concentrated on enlarging the sensing range of BOTDA systems beyond 100 km, maintaining a resolution in the order of meters, or even below the meter, so it can be properly applied to the most demanding commercial applications. For such purpose, we propose to combine distributed Raman amplification, a range extension technique already tested by several research groups, with some other measuring and/or range and resolution enhancing procedures (Vector BOTDA (VBOTDA), pulse coding, "de-noising" and Differential Pulse-width Pair (DPP) technique) so the target specifications are achievable. In all cases, it will be necessary to take special care of the associated detrimental phenomena (Self-Phase Modulation (SPM), Modulation Instability (MI), depletion and Relative Intensity Noise (RIN) transfer) that manifest and degrade the performance of the system.

1.2 Objectives

From the previously cited motivations, the following objectives have been addressed over the thesis work:

- Study of the linear and non-linear effects that are necessary to develop Raman-assisted BOTDA systems, especially the non-linear Raman and Brillouin scattering phenomena.
- Properly identify all the non-desired effects that manifest within the fiber when developing high resolution and long range BOTDA systems in order to avoid them in future systems. The cited phenomena are SPM, MI, depletion and RIN noise.
- Validate the application of First-order Raman amplification on BOTDA systems and combine it with Second-order Raman assistance and pulse coding, so the measuring range can be fully extended for ultra-long linear sensing range applications.
- Develop and test data treatment and measuring techniques ("de-noising" and VBOTDA) that reduce the detrimental effect of RIN transfer produced by the high power Raman Fiber Lasers (RFL) employed to provide long range distributed Raman amplification. As a consequence, the resolution enhancer DPP technique could also be applicable in order to reach sub-metrical resolutions.

1.3 Structure of the Work

The work is divided in six chapters. The four main ones correspond with the four main objectives treated in this thesis dissertation and defined in the previous section:

- Chapter 2: "Linear and Non-Linear Effects in Fiber Optics" deals with all the theoretical basis needed to properly understand the linear and non-linear effects produced within the sensing fiber when BOTDA systems are developed. A special focus will be denoted to the Stimulated Brillouin and Raman Scattering processes (SBS and SRS respectively) since they are the main non-linear effects employed in long or ultra-long range Raman-assisted BOTDA setups.
- Chapter 3: "BOTDA: Principles, Limitations and State of the Art" describes the actual state of the art of BOTDA systems and focuses on the undesired effects that arise in high-resolution long-range Raman-assisted BOTDA systems, such as SPM, MI, depletion and RIN transfer. It will be necessary to avoid or at least minimize such effects in order to achieve the objectives given in terms of range and resolution.
- Chapter 4: "Optimization of Long Range Raman-Assisted BOTDA Systems" focuses on our own works on trying to validate and test the combination of First- and Second-order Raman assistance techniques together with pulse coding in order to fully extend the sensing range of BOTDA systems. It is demonstrated a proper performance of a 2 meter resolution 100 km long First-order Raman-assisted BOTDA (using simple and analytical optimization procedures) and a 5 meter resolution 240 km linear long (120 km sensing range) First- and Second-order Raman-assisted pulse-coded BOTDA.

- Chapter 5: "RIN Reduction in Long Range Raman-Assisted BOTDA Systems" deals with the development of original methods to avoid the transfer of RIN from high-power RFLs (commonly employed in long range Raman-assisted BOTDA systems) to the BOTDA probe wave. Its reduction through a VBOTDA scheme and a novel numerical technique denominated as "de-noising", opens the gate for enhancing the resolution until sub-metrical levels even in very long range setups and also provides the opportunity to develop real-time measurements over such long distances.

Chapter 2

Linear and Non-Linear Effects in Fiber Optics

2.1 Introduction

In this chapter we will describe and develop in sufficient detail all the physics behind optical fibers. In order to have a better view on how optical fibers behave when dealing with the systems described along this thesis dissertation, it is necessary to understand their linear and non-linear response by describing the most dominant elements that arise. In the case of non-linearities, it will be necessary to avoid their appearance since, as we will describe later on, they have a detrimental effect on the proper performance of our systems. Another phenomena that manifest within the fiber, known as scattering, encompasses the main description of this chapter since they are the basis of the thesis. Raman and Brillouin scattering will be pictured deeply so that a proper understanding can be acquired.

2.2 Response of Fiber Optics to an Electromagnetic Field

The phenomenon of light propagation in a material medium, such as an optical fiber, like any other phenomenon where an electromagnetic field is present, can be described by Maxwell's equations [1]:

$$\nabla \times \mathbf{E} = -\frac{\partial \mathbf{B}}{\partial t} \tag{2.1}$$

$$\nabla \times \mathbf{H} = \mathbf{J} + \frac{\partial \mathbf{D}}{\partial t} \tag{2.2}$$

$$\nabla \cdot \mathbf{D} = \rho \tag{2.3}$$

$$\nabla \cdot \mathbf{B} = 0 \tag{2.4}$$

where $\mathbf{E}$ and $\mathbf{H}$ are the electric and magnetic field vectors, $\mathbf{B}$, $\mathbf{J}$ and $\mathbf{D}$ are respectively the magnetic induction, the current density and the electric displacement vectors and ρ is the charge density. The spatial derivative is expressed through the ∇ operator.

The definition of both electric displacement and magnetic field vectors ($\mathbf{D}$ and $\mathbf{H}$) should be included in order to complement Maxwell's differential equations. Therefore, on one hand, it is necessary to take into account the induced polarization by the field in the medium when analyzing the electric density flux ($\mathbf{D}$) in a dielectric media. This electric polarization comes motivated by the reorientation of the bond charges of the material when crossing an electric field. Therefore, $\mathbf{D}$ is expressed as:

$$\mathbf{D} = \epsilon_0 \mathbf{E} + \mathbf{P} = \epsilon \mathbf{E} \tag{2.5}$$

where ϵ_0 and ϵ represent the electric permittivity in vacuum and in the medium, and $\mathbf{P}$ is the induced electric polarization. On the other hand, the magnetic flux density ($\mathbf{B}$) arises as an answer to the magnetic field ($\mathbf{H}$) within the medium, which comes determined by:

$$\mathbf{H} = \frac{\mathbf{B}}{\mu_0} - \mathbf{M} = \frac{\mathbf{B}}{\mu} \tag{2.6}$$

where μ_0 and μ represent the magnetic permeability in vacuum and in the medium respectively, and $\mathbf{M}$ is the induced magnetic polarization.

In order to adapt these equations to the specific case of electromagnetic wave guidance in fiber optics, some particular conditions should be considered [2]:

- Optical fibers are dielectric media, where no free charges are present, so it can be assumed that $\mathbf{J} = 0$ and $\rho = 0$.
- Optical fibers are non-magnetic media, therefore the induced magnetic polarization equals zero ($\mathbf{M} = 0$), and the flux density ($\mathbf{B}$) can be expressed as:

$$\mathbf{B} = \mu_0 \mathbf{H} \tag{2.7}$$

- Optical fibers are indeed dielectric media where no permanent polarization is present since the polarization vector ($\mathbf{P}$) is induced by the electric field. Therefore, there is always a functional relation between these two fields that can be phenomenologically expressed as a power of series of the electric field vector ($\mathbf{E}$) such as [3]:

$$\mathbf{P} = \epsilon_0 \left(\chi^{(1)} \cdot \mathbf{E} + \chi^{(2)} : \mathbf{EE} + \chi^{(3)} \vdots \mathbf{EEE} + \dots \right) \tag{2.8}$$

  where $\chi^{(1)}$ describes the linear relationship between the polarization and electric field vectors and $\chi^{(2)}$ and $\chi^{(3)}$ are tensors that describe the non-linear relationship between the same vectors.

- The medium is isotropic and in a first approximation can be assumed linear for the resolution of Maxwell's equations. Therefore, since the non-linear effects are relatively weak in silica fibers for the cases we will study here, it is possible to relate the real and imaginary parts of $\chi^{(1)}$ with the real part of the refractive index of the material (n_0) and the attenuation (α), and at the same time to assume very low attenuation for optical fibers. Thus ϵ can be considered real and in the following way [1]:

$$\epsilon(\omega) = \epsilon_0 n^2(\omega) \cong \epsilon_0 n_0^2(\omega) \tag{2.9}$$

- Strictly monochromatic waves are assumed, where the angular frequency (ω) follows:

$$\omega = \frac{2\pi}{\lambda} c = kc \tag{2.10}$$

  where $c = 1/\sqrt{\mu_o \epsilon_0}$, λ and k are respectively the speed of light, the wavelength and the wave number in vacuum.

Under all the previous assumptions, Maxwell's equations can be therefore rewritten in the following way:

$$\nabla \times \mathbf{E} = i\sqrt{\frac{\mu_0}{\epsilon_0}}k\mathbf{H} \tag{2.11}$$

$$\nabla \times \mathbf{H} = i\sqrt{\frac{\mu_0}{\epsilon_0}}kn^2\mathbf{E} \tag{2.12}$$

$$\nabla \cdot (n^2\mathbf{E}) = 0 \tag{2.13}$$

$$\nabla \cdot \mathbf{H} = 0 \tag{2.14}$$

Equations 2.11 and 2.12 couple spatial evolutions of $\mathbf{E}$ and $\mathbf{H}$ and they can be decoupled by considering wave equations for the fields. Therefore, the following wave equations can be obtained with the equivalences $\nabla \times (\nabla \times \mathbf{A}) \equiv \nabla \cdot (\nabla \cdot \mathbf{A}) - \nabla^2 \cdot \mathbf{A}$ [2]:

$$(\nabla^2 + k^2n^2)\mathbf{E} = -\nabla\left(\mathbf{E}\frac{\nabla n^2}{n^2}\right) \tag{2.15}$$

$$(\nabla^2 + k^2n^2)\mathbf{H} = (\nabla \times \mathbf{H}) \times \frac{\nabla n^2}{n^2} \tag{2.16}$$

2.3 Linear Propagation

In this section we will briefly summarize the basic concepts of linear propagation phenomena that we are interested in. Assuming a linear response of the medium, the polarization induced by a propagating electric field within the fiber (when the power levels are low or moderate) can be written as [4]:

$$\mathbf{P}(\mathbf{r}, t) = \epsilon_0 \int_{-\infty}^{+\infty} \bar{\chi}^{(1)}(t - t')\mathbf{E}(\mathbf{r}, t')dt' \tag{2.17}$$

The refractive index (n) and the attenuation (α) are related to $\chi^{(1)}(\omega)$ through [1, 4]:

$$n(\omega) = 1 + \frac{1}{2}\Re[\chi^{(1)}(\omega)] \tag{2.18}$$

$$\alpha(\omega) = \frac{\omega}{nc}\Im[\chi^{(1)}(\omega)] \tag{2.19}$$

where $\chi^{(1)}(\omega)$ is the Fourier transform of $\chi^{(1)}(t)$. Therefore, if we express the electric field ($\mathbf{E}$) in the frequency domain and assuming no losses within the fiber, we will have:

$$\nabla^2\widetilde{\mathbf{E}} + n^2(\omega)\frac{\omega^2}{c^2}\widetilde{\mathbf{E}} = 0 \tag{2.20}$$

This is the equation that we need to solve in order to know the linear behavior of light when propagating within the fiber. Even though the electric field vector has three

components (x, y and z), normally only one is employed, typically $\widetilde{E}_z(\mathbf{r},\omega)$ and it can be shown that they are all related. Since our problem has a cylindric symmetry, developing the variable separation method the obtained solution suits the following scheme:

$$\widetilde{E}_z(\mathbf{r},\omega) = \widetilde{A}(\omega)F(\rho_c)\exp(\pm im\phi_c)\exp(i\beta z) \tag{2.21}$$

where ϕ_c and ρ_c are cylindric coordinates, $\widetilde{A}(\omega)$ is an amplitude term, m is an integer and $F(\rho_c)$ gives the field distribution within the fiber section. In general, many solutions can be obtained which are denominated as modes, some of which and can be observed in Figure 2.1 [5].

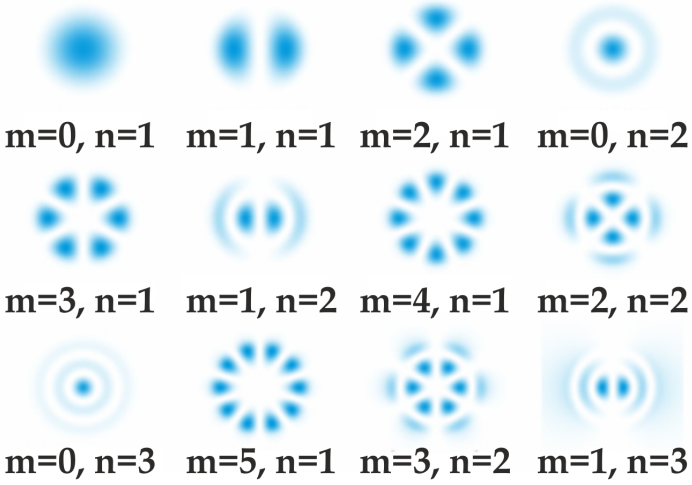

Figure 2.1: *Intensity profiles of an optical fiber, where m and n take integer values [1, 5].*

Even though many solutions are possible, through a certain control of geometry it is possible to obtain a unique mode, condition referred as single mode propagation. From equation 2.21, $F(\rho_c)$ denotes the modal distribution and β the fiber propagation constant, which is a function of the frequency ω [1]. Both elements can be obtained from the following equation and applying suitable boundary conditions:

$$\frac{d^2F(\rho_c)}{d\rho_c^2} + \frac{1}{\rho_c}\frac{dF(\rho_c)}{d\rho_c} + \left(n^2(\rho_c)\frac{\omega^2}{c^2} - \beta^2 - \frac{m^2}{\rho_c^2}\right)F(\rho_c) = 0 \tag{2.22}$$

The dependency of β with frequency comes determined by the frequential and radial reliance of the refractive index. The mode confinement within the fiber core (guidance) is only achieved when the average value of the index inside the fiber is higher than in the cladding. The fundamental mode (when referring to single mode fibers) is obtained when $m = 0$ and appears as a unique form from zero frequency until a certain ω_c frequency known as cutoff frequency, which also depends on the radial dependence of the refractive index for step-index fibers. The multi-mode condition is obtained when [1]:

$$V = \frac{2\pi a}{\lambda_c}\sqrt{n_1^2 - n_2^2} > 2.405 \tag{2.23}$$

where V is the normalized frequency, a is the core radius, λ_c is the central wavelength and n_1 and n_2 are the core and cladding refractive index respectively.

The distribution of the fundamental mode field follows a Gaussian approachable law through:

$$F(\rho_c) \simeq \exp\left(-\frac{\rho_c^2}{\rho_{cw}^2}\right) \tag{2.24}$$

where ρ_{cw} measures the effective radius that occupies the mode. The $2\rho_{cw}$ quantity is denominated as the diameter of the modal field [6].

In the usual case, the total spectral width of the signals ($\Delta\omega$) is much smaller than the central frequency. In this case, we can describe the propagation constant all along the spectral range of interest through a Taylor series:

$$\beta(\omega) = \beta_0 + \beta_1(\omega - \omega_0) + \frac{1}{2}\beta_2(\omega - \omega_0)^2 + ... \tag{2.25}$$

where β_0, β_1 y β_2 parameters give us information related to the phase and group velocities, being:

$$\beta_i = \left.\frac{d^i\beta}{d\omega^i}\right|_{\omega=\omega_0} \qquad (i = 1, 2, 3, ...) \tag{2.26}$$

2.3.1 Phase Velocity, Group Velocity and Chromatic Dispersion

Chromatic dispersion, which is directly related to the dependence of the propagation constant with frequency $\beta(\omega)$, is a phenomenon that arises as a consequence of the linear propagation of the light within the fiber. In order to explain the chromatic dispersion it is very useful to consider a spectrum centered around the frequency ω_0, as expressed in equation 2.25 and 2.26.

Phase velocity (v_p) is the ratio between the angular frequency (ω) and the propagation constant (β), and it can be understood as the propagation velocity of a harmonic wave (e.g. produced by a continuous laser) along the fiber. Group velocity (v_g), on the other hand, is defined as the derivative of the frequency versus the propagation constant, and equals the inverse of β_1:

$$v_g = \frac{d\omega}{d\beta} = \frac{1}{\beta_1} \tag{2.27}$$

Group velocity (v_g) is the velocity at which the slowly varying envelope of a harmonic wave propagates (e.g. the modulating sinusoid of a laser output). v_p and v_g are not equal in general, unless β and ω are linearly related. As stated, although they are not equal, phase and group velocities in optical fibers are very similar and almost equal to $2{\cdot}10^8$ $\mathrm{m{\cdot}s^{-1}}$ [4].

The relationship between β_2 and the group velocity is immediate:

$$\beta_2 = \frac{d}{d\omega}\left(\frac{1}{v_g}\right) = \frac{d\tau_g}{d\omega} \tag{2.28}$$

where τ_g is the group delay for unit length. β_2 measures the variation of the group delay experienced by the different spectral components around the central frequency ω_0. Therefore, β_2 is responsible for the broadening of the pulses that propagate in linear regime all along the fiber. This is the reason why β_2 is denominated as group velocity dispersion. In order to measure this parameter, it is commonly employed the chromatic dispersion coefficient (D), which is directly related with β_2:

$$D = \frac{d\beta_1}{d\lambda} = -\frac{2\pi c}{\lambda^2}\beta_2 \tag{2.29}$$

where β_2 is measured in $\text{ps}^2\cdot\text{Km}^{-1}$ and D in $\text{ps}\cdot\text{nm}^{-1}\cdot\text{km}^{-1}$.

The dispersion can be canceled at a certain wavelength, which is known as the zero dispersion wavelength (λ_0). Above this wavelength ($D > 0, \beta_2 < 0$) the fibers show a dispersion regime known as anomalous (which effect is represented in Figure 2.2(a)), and below ($D < 0, \beta_2 > 0$) the propagation is developed at normal dispersion regime. The transition between both regimes can be observed in Figure 2.2(b) for different commercial optical fibers.

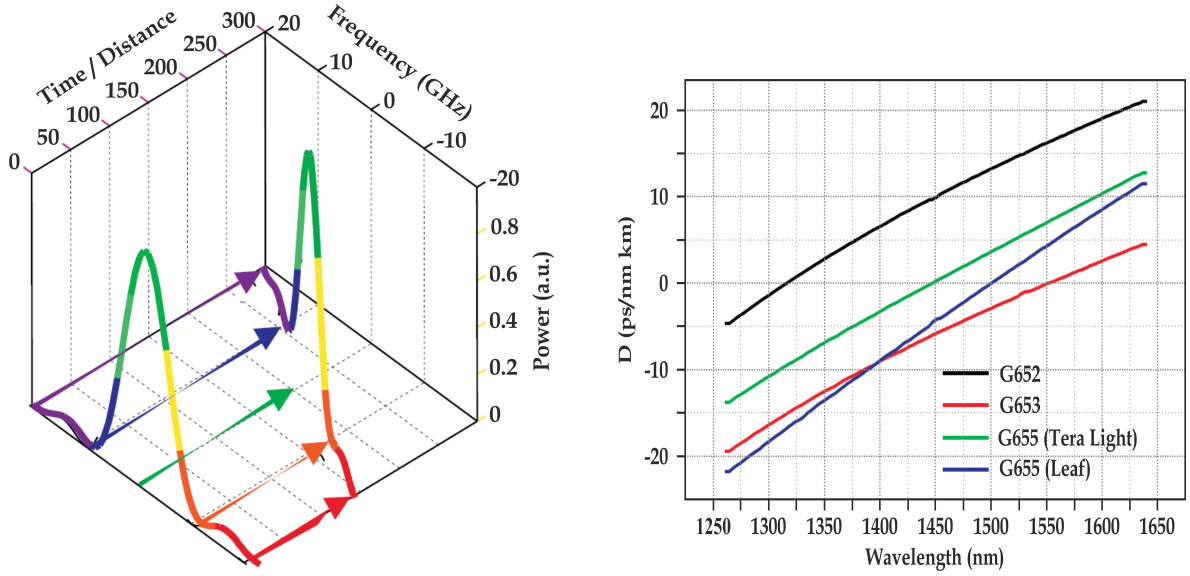

(a) Pulse behavior in an anomalous chromatic dispersion fiber.

(b) Chromatic dispersion coefficient as a function of λ for different optical fibers.

Figure 2.2: *Different representations of the chromatic dispersion effect [4].*

2.4 Non-Linear Propagation

In order to study the behavior of an intense light beam propagating through a single mode fiber it is necessary to study the relationship between the electric field ($\mathbf{E}$) and the polarization ($\mathbf{P}$) through the following equation [1]:

$$\nabla^2\mathbf{E} - \frac{1}{c^2}\frac{\partial^2\mathbf{E}}{\partial t^2} = \mu_0\frac{\partial^2\mathbf{P}_L}{\partial t^2} + \mu_0\frac{\partial^2\mathbf{P}_{NL}}{\partial t^2} \tag{2.30}$$

which is based on Faraday's rotational law (equation 2.1), the assumptions made for the electromagnetic wave guidance in fiber optics (section 2.2) and taking into account the existing small non-linearity.

In order to make the mathematical development more comprehensive, several simplifications can be considered. Firstly, we can consider that $\mathbf{P}_{NL}$ is a small perturbation compared to $\mathbf{P}_L$. Secondly, the optical field maintains its polarization all along the optical fiber, therefore a scalar approach is valid. Thirdly, the optical field is presumed to be quasi-monochromatic; thus the spectral width of the pulse ($\Delta\omega$), which is assumed to be centered at ω_0, suits $\Delta\omega/\omega_0 << 1$.

As a slowly varying envelope approximation has been assumed, it is beneficial to divide the rapidly varying parts of the electric field and the polarizations:

$$\mathbf{E}(\mathbf{r},t) = \frac{1}{2}\hat{x}[E(\mathbf{r},t)\exp(-i\omega_0 t) + c.c.] \tag{2.31}$$

$$\mathbf{P}_L(\mathbf{r},t) = \frac{1}{2}\hat{x}[P_L(\mathbf{r},t)\exp(-i\omega_0 t) + c.c.] \tag{2.32}$$

$$\mathbf{P}_{NL}(\mathbf{r},t) = \frac{1}{2}\hat{x}[P_{NL}(\mathbf{r},t)\exp(-i\omega_0 t) + c.c.] \tag{2.33}$$

where $\hat{x}$ is the polarization unit vector and $E(\mathbf{r},t)$, $P_L(\mathbf{r},t)$ and $P_{NL}(\mathbf{r},t)$ are slowly varying functions of time.

The linear component of P_L can be obtained substituting equation 2.32 in equation 2.17, and its given by:

$$P_L(\mathbf{r},t) = \frac{\epsilon_0}{2\pi}\int_{-\infty}^{\infty} \widetilde{\chi}^{(1)}_{xx}(\omega)\widetilde{E}(\mathbf{r},\omega-\omega_0)\exp[-i(\omega-\omega_0)t]d\omega \tag{2.34}$$

where $\widetilde{E}(\mathbf{r},\omega-\omega_0)$ is the Fourier transform of $E(\mathbf{r},t)$.

For the non-linear polarization component ($\mathbf{P}_{NL}$), it can be considered that the non-linear response is instantaneous, so the time dependence of $\chi^{(3)}$ can be simplified, therefore:

$$\mathbf{P}_{NL}(\mathbf{r},t) = \epsilon_0\chi^{(3)}\vdots\mathbf{E}(\mathbf{r},t)\mathbf{E}(\mathbf{r},t)\mathbf{E}(\mathbf{r},t) \tag{2.35}$$

When considering the non-linear response instantaneous, the contribution of molecular vibrations in $\chi^{(3)}$ is neglected. These vibrations are due to the Raman effect, which will be explained in detail in subsection 2.5.1.2 and section 2.7, and occur with time delays in the order of $\tau_R = 60-70$ fs. The response of the fiber can only be considered instantaneous if a bandwidth much smaller than $1/\tau_R \simeq 13$ THz is given to the optimal input [1]. Usually, this assumption can be considered valid only if the employed pulses are < 1 ps. Therefore, P_{NL} can be expressed as:

$$P_{NL}(\mathbf{r},t) \approx \epsilon_0\epsilon_{NL}E(\mathbf{r},t) \tag{2.36}$$

where the non-linear contribution to the electric constant is defined as:

$$\epsilon_{NL} = \frac{3}{4}\chi^{(3)}_{xxxx}\left|E(\mathbf{r},t)\right|^2 \tag{2.37}$$

To obtain the slowly varying amplitude of $E(\mathbf{r},t)$, it is convenient to work in the Fourier domain:

$$\widetilde{E}(\mathbf{r},\omega-\omega_0) = \int_{-\infty}^{\infty} E(\mathbf{r},t)\exp[i(\omega-\omega_0)t]dt \tag{2.38}$$

which satisfies the Helmholtz equation [1]:

$$\nabla^2\widetilde{E} + \epsilon(\omega)k_0^2\widetilde{E} = 0 \tag{2.39}$$

where $k_0 = \omega/c$ and $\epsilon(\omega)$ is the dielectric constant. Therefore, equation 2.39 can be solved using the method of separation of variables, assuming a solution of the form:

$$\widetilde{E}(\mathbf{r},\omega-\omega_0) = F(x,y)\widetilde{A}(z,\omega-\omega_0)\exp(i\beta_0 z) \tag{2.40}$$

where $\widetilde{A}(z,\omega)$ is a slowly varying function of z and β_0 is the wave number. From the assumed expression, $F(x,y)$ and $\widetilde{A}(z,\omega)$ are:

$$\frac{\partial^2 F}{\partial x^2} + \frac{\partial^2 F}{\partial y^2} + [\epsilon(\omega)k_0^2 - \widetilde{\beta}^2]F = 0 \tag{2.41}$$

$$2i\beta_0\frac{\partial\widetilde{A}}{\partial z} + (\widetilde{\beta}^2 - \beta_0^2)\widetilde{A} = 0 \tag{2.42}$$

Now, it is possible to go back to the time domain considering from equations 2.24 and 2.25 that the higher-order terms are small if $\Delta\omega << \omega_0$ and that $\beta \approx \beta_0$. Therefore, through the inverse Fourier transform it can be concluded that:

$$A(z,t) = \frac{1}{2\pi}\int_{-\infty}^{\infty}\widetilde{A}(z,\omega-\omega_0)\exp[-i(\omega-\omega_0)t]d\omega \tag{2.43}$$

Using the Fourier transform, $\omega-\omega_0$ can be replaced by $i(\partial/\partial t)$ in the time domain, then the resulting equation for $A(z,t)$ becomes:

$$\frac{\partial A}{\partial z} + \beta_1\frac{\partial A}{\partial t} + \frac{i\beta_2}{2}\frac{\partial^2 A}{\partial t^2} + \frac{\alpha}{2}A = i\gamma|A|^2A \tag{2.44}$$

where A has been already normalized so that $P = |A|^2$. This equation is commonly known as Non-Linear Schrödinger's Equation (NLSE) [1,7] due to its similarities to Schrödinger's equation with non-linear potential. γ, defined as the nonlinear parameter, is expressed as:

$$\gamma = \frac{n_2\omega_0}{cA_{eff}} \tag{2.45}$$

where A_{eff} is known as the effective core area and is defined as:

$$A_{eff} = \frac{(\int\int_{-\infty}^{\infty} |F(x,y)|^2 \, dxdy)^2}{\int\int_{-\infty}^{\infty} |F(x,y)|^4 \, dxdy} \tag{2.46}$$

The effective area (A_{eff}) measures the equivalent non-linear area that the field occupies inside the fiber. The typical value for this parameter is 72 μm^2 for conventional Single Mode Fibers (SMF) at 1550 nm.

Before concluding this section, it is important to introduce the concept of non-linear effective length (L_{eff}). The effective length is an equivalent "lossless" fiber distance that the light needs to cover in order to create the same non-linear effect as a losing fiber. Its value comes determined from the following expression:

$$L_{eff} = \int_0^L \exp(-\alpha z) dz = \frac{1 - \exp(-\alpha L)}{\alpha} \tag{2.47}$$

For short fiber lengths it is usually considered that $L_{eff} \simeq L$. On the other hand, for long fiber ranges, $L_{eff} \simeq 1/\alpha$. So, for considerably long fibers, in the third window propagation region, we obtain that $L_{eff} \simeq 22$ km.

2.4.1 Non-Linear Refraction

Non-linear refraction is understood as the variation produced by the intensity of the incident wave on the refractive index of a material. The dependence of the refractive index of a fiber with intensity can be expressed as [8]:

$$n(I) = n_0 + n_2 I \tag{2.48}$$

As stated in the previous section (2.4), the value of n_2 is very small in optical fibers ($\simeq 2 \cdot 10^{-20}$ m^2W^{-1}). However, the obtained modulation in the refractive index for high powers and long distances is enough to notice phase differences (e.g. when $PL_{eff} \simeq 1$ W·km, the introduced non-linear phase reaches $\phi_{NL} \simeq \pi/2$).

2.4.1.1 Self-Phase Modulation - SPM

In common literature, [1, 7], Self-Phase Modulation (SPM) is known as the non-linear refraction effect that arises within the same signal that modulates the fiber index. In order to study SPM it is convenient to introduce some simplifications before starting to work with the NLSE (2.44). They allow to make it mathematically more appropriate to handle and they do not suppose a great physical variation of the system. Firstly, we must consider a time-scale with a reference point that travels at the same velocity as the envelope wave of the light pulse does, known as group velocity (v_g) (see equation 2.27). Mathematically, it is defined as the inverse of the first derivative of β. If the duration of the pulse is also normalized to the input pulse width T_0, another time variable can be defined [8]:

$$\tau = \frac{t - z/v_g}{T_0} \tag{2.49}$$

from which the shape of the propagating wave along the fiber can be expressed. In addition, the amplitude of the slow variation can be expressed in terms of a normalized amplitude U as [8]:

$$A(z,\tau) = \sqrt{P_0}U(z,\tau) \tag{2.50}$$

where P_0 is the peak power of the signal. In addition, if the losses within the fiber and the dispersion of the group velocity are considered inexistent, the equation 2.44 can be rewritten as:

$$\frac{\partial U}{\partial z} = i\gamma P_0 |U(z,\tau)|^2 U(z,\tau) \tag{2.51}$$

At the output of the fiber, $z = L$, the solution of 2.51 is:

$$U(L,\tau) = U(0,\tau)\exp(i\phi_{NL}) \tag{2.52}$$

where ϕ_{NL} is the non-linear phase that introduces the SPM and comes determined by the pump power and the non-linear coefficient of the fiber:

$$\phi_{NL} = \gamma P_0 |U(0,\tau)|^2 L \tag{2.53}$$

As we can see, the modification of the power at the refractive index affects the phase of the signal. The introduced non-linear phase will depend on the instantaneous power of the signal and, therefore, its effect will not just depend on the power of the signal but also on its shape. Actually, it can be considered the variation of the instantaneous frequency with the intensity of the signal:

$$\Delta\omega(\tau) = -\frac{\partial\phi_{NL}}{\partial\tau} = -\gamma P_0 L \frac{\partial}{\partial\tau}(|U(0,\tau)|^2) \tag{2.54}$$

If we consider a pulse at the input of the fiber and we observe the expression 2.54, it can be noticed how the instantaneous frequency will displace to the red-color region in the rising edge of the pulse ($\Delta\omega < 0$) and to the blue-color region in the falling edge ($\Delta\omega > 0$). This is effectively evidenced as a broadening of the pulse spectrum although, not in the temporal shape, as shown in Figure 2.3 [9].

Also the combination of the dispersion and the refraction can be considered. The dependence of the temporal shape with the chromatic dispersion, as mentioned in subsection 2.3.1, determines that in the anomalous dispersion the group delay is greater for longer wavelengths and smaller at shorter wavelengths. This makes the rising edge of the phase-shifted pulse to go slower than the falling edge, therefore compressing the pulse. In the case of the normal dispersion, the group delay evolves inversely to the frequency, thus the pulse will suffer an additional temporal broadening (see Figure 2.3).

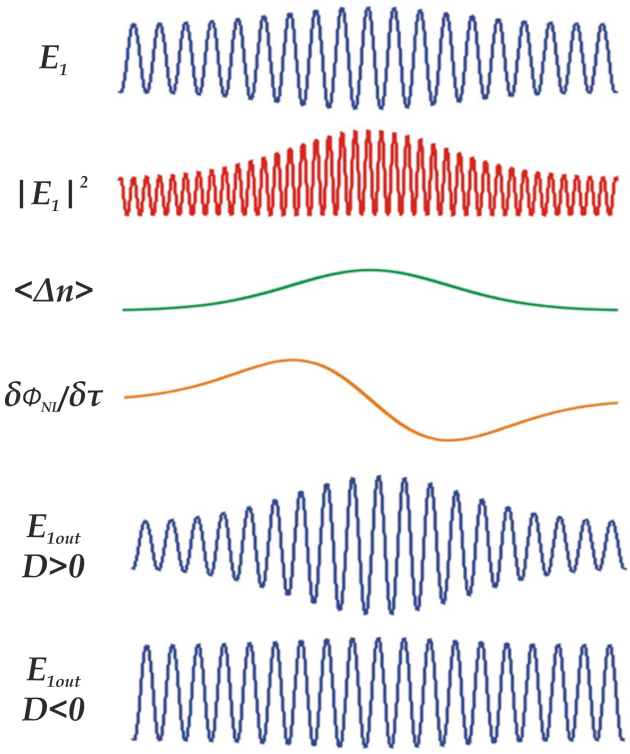

Figure 2.3: *Qualitative illustration of the effect of SPM.*

2.4.1.2 Modulation Instability - MI

Traditionally, Modulation Instability (MI) is known as the phenomenon that manifests with the appearance of two side lobes in the spectral domain of a continuous pump wave. From the temporal domain point of view, this can be translated as the apparition of a series of ultrashort pulses from a continuous wave input. To observe the MI phenomenon, it is necessary that the propagation of the light occurs in the anomalous dispersion regime ($\beta_2 < 0, D > 0$). The theoretical explanation of this phenomenon can be found if a study of the solution of the equation 2.44 is developed. If the losses within the fiber are considered zero, the following expression can be obtained [4]:

$$i\frac{\partial A}{\partial z} = \frac{\beta_2}{2}\frac{\partial^2 A}{\partial T^2} - \gamma|A|^2 A \tag{2.55}$$

where $T = t - z/v_g$. If this equation is solved, the following stationary solution can be found [4]:

$$A(z,T) = \sqrt{P_0}\exp(i\gamma P_0 z) \tag{2.56}$$

As we can see, the effect of the SPM in a continuous beam consists of modifying the phase of the wave at the output of the fiber. In order to study the stability of the solution, a small perturbation is introduced, a [4]:

$$A(z,T) = \left(\sqrt{P_0} + a(z,T)\right)\exp(i\gamma P_0 z) \tag{2.57}$$

By substituting 2.57 in 2.44 and disregarding the power terms greater than 1 in a, the following equation can be obtained [4]:

$$i\frac{\partial a}{\partial z} = \frac{\beta_2}{2}\frac{\partial^2 a}{\partial T^2} - \gamma P_0(a + a^*) \tag{2.58}$$

If this new equation is solved in the frequency domain, we find that as the a^* (complex conjugate of a) term appears the Fourier components of the $\pm\Omega$ frequencies are coupled. Therefore, the solutions of the differential equation 2.58 should have the following shape [4]:

$$a(z,T) = a_1 \exp[i(kz - \Omega T)] + a_2 \exp[-i(kz - \Omega T)] \tag{2.59}$$

where k is the wave number and Ω the frequency of the perturbation. The following step is to substitute the new solution 2.59 in the linear differential equation 2.58. If the exponential factors are grouped we obtain [4]:

$$\begin{aligned} \exp[i(kz - \Omega T)]\left(-ka_1 + \frac{\beta_2}{2}\Omega^2 a_1 + \gamma P_0 a_1 + \gamma P_0 a_2\right) + \\ + \exp[-i(kz - \Omega T)]\left(ka_2 + \frac{\beta_2}{2}\Omega^2 a_2 + \gamma P_0 a_2 + \gamma P_0 a_1\right) = 0 \end{aligned} \tag{2.60}$$

Therefore, it can be deduced that one and each of the terms that multiply the complex exponentials should be zero. From this condition two homogeneous coupled equations are obtained [4]:

$$\left(-k + \frac{\beta_2}{2}\Omega^2 + \gamma P_0\right) a_1 = -\gamma P_0 a_2 \tag{2.61}$$

$$\left(k + \frac{\beta_2}{2}\Omega^2 + \gamma P_0\right) a_2 = -\gamma P_0 a_1 \tag{2.62}$$

This system has no trivial solution only when the wave number and the frequency of the perturbation verifies the following relationship [4]:

$$k = \pm\frac{1}{2}|\beta_2\Omega|\sqrt{\Omega^2 + \frac{4\gamma P_0}{\beta_2}} \tag{2.63}$$

Observing the last expression, it can be appreciated how determinant is the dispersion regime of the light traveling through the fiber. If the sign of β_2 is positive, then the wave number is real at any frequency around the central frequency. In that case, all the solutions should have constant amplitude and it can be confirmed that the stationary solution of the equation 2.55 is stable in the presence of small perturbations. On the contrary, if the propagation regime is anomalous $\beta_2 < 0$, for $|\Omega| < \sqrt{4\gamma P_0 {\beta_2}^{-1}}$ the values of k are pure imaginary, and therefore the amplitude of the perturbation increases exponentially as light travels through the fiber.

The effect of the power gain that suffers a signal separated in frequency Ω comes determined by [4]:

$$g_{mi}(\Omega) = |\beta_2\Omega|\sqrt{\frac{4\gamma P_0}{|\beta_2|} - \Omega^2} \tag{2.64}$$

where $g_{mi}(\Omega) = 2\Im(K)$ so the factor 2 converts g_{mi} to power gain.

If we develop a study of the evolution of the function $g_{mi}(\Omega)$ with frequency, we observe that two maximums are produced at $\Omega_{max} = \pm\sqrt{2\gamma P_0/|\beta_2|}$. The gain at that region is $g_{mi}(\Omega_{max}) = 2\gamma P_0$ [4].

The cited influence of the dispersion and the pump power in the MI gain (g_{mi}) has already been demonstrated experimentally by e.g. Martin-Lopez in her thesis dissertation [4]. With smaller dispersion coefficient (D) the gain sidebands become broader while the gain remains constant (Figure 2.4(a)). In case the pump power is increased, the gain sidebands widen too but also increase their level (Figure 2.4(b)).

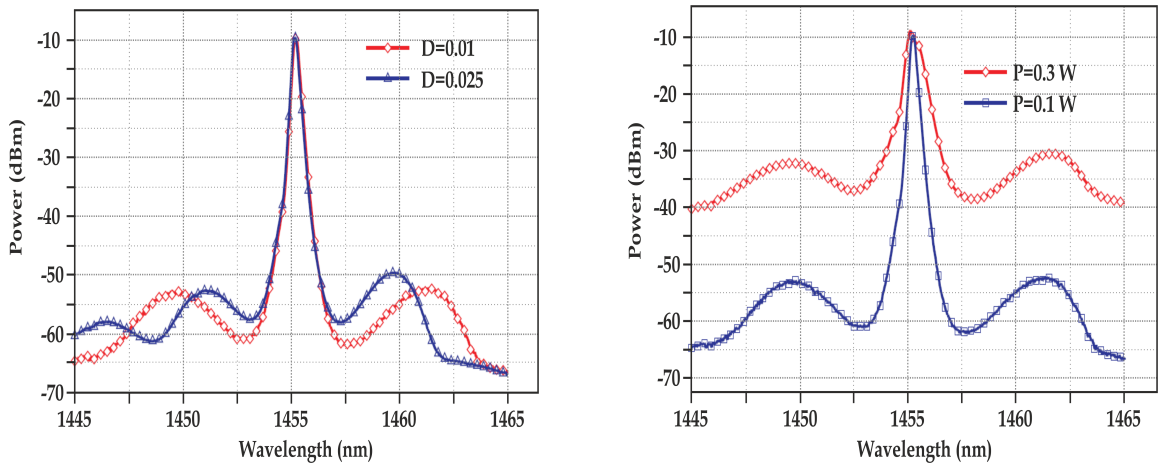

(a) (b)

Figure 2.4: *Pulse spectrum gain variation as a result of MI effect as a function of dispersion (a) and pump power (b) [4].*

2.5 Scattering Effects in Fiber Optics

The physical process known as scattering describes the deviation that a wave suffers from its straight trajectory when encountering different non-uniformities through the medium as it travels along.

The mentioned deviation or scattering can have a different nature depending on the intensity of the variables present on the phenomenon. If light is considered as an electromagnetic wave that travels through a dielectric medium such as an optical fiber, the scattering can be considered linear (Spontaneous - subsection 2.5.1) if the light power is lower than a certain threshold level or non-linear (Stimulated - subsection 2.5.2) if it is higher.

2.5.1 Linear or Spontaneous Scattering Effects

When talking about spontaneous scattering effects, it is implied that the optical properties of the medium where the light beam is traveling through remain unaltered. This reaction only arises when the power of the mentioned light beam is lower than a certain threshold level; above that level, the scattering effect is considered stimulated, which will be described in detail in forthcoming sections (2.6 and 2.7). Therefore, the spontaneous scattering effect is generated by the mechanical or thermal excitation of the medium with an intensity that is proportional to the intensity of the incident light.

If we consider an inhomogeneous medium such as optical fibers, the scattering process will remove some photons of the incident light producing at the same time scattered photons that may be shifted in direction, phase and frequency. Depending on the energy transfer from the medium to the new scattered photons, the following classification can be developed:

- Elastic Scattering: The scattered photons maintain their energy, therefore having the same frequency as the incident light.
  - Rayleigh Scattering: It is the unique elastic scattering phenomenon since it does not produce a frequency shift. It arises from non-propagating density fluctuations of the medium which could result from degree variations of molecular organization states.

- Inelastic Scattering: In this case, the scattered photons have a different frequency since an energy transference arises from or to the medium. From a quantum mechanical point of view, it is the interaction of photons with phonons, that is, discrete quantities of light and medium excitation respectively. When the scattered photons are downshifted in frequency, they are commonly known as the Stokes components. On the contrary, when they are upshifted, so the incident photons gain energy from the medium, they are labeled as anti-Stokes components.
  - Brillouin Scattering: It is an inelastic scattering process originated from propagating pressure waves, originated by acoustic phonons, which frequency shift is determined by the acoustic velocity in the medium.
  - Raman Scattering: It is a highly inelastic scattering process since the interaction is developed between photons and optical phonons. This arises since the nature of the process is based in the interaction between light and molecular vibrational modes.

Figure 2.5 shows the different types of scattering present in a dielectric medium under monochromatic light conditions.

In the following subsections we will describe in detail the spontaneous Brillouin and Raman scattering, omitting the Rayleigh scattering, since the main development of this thesis dissertation is based on Brillouin and Raman phenomena.

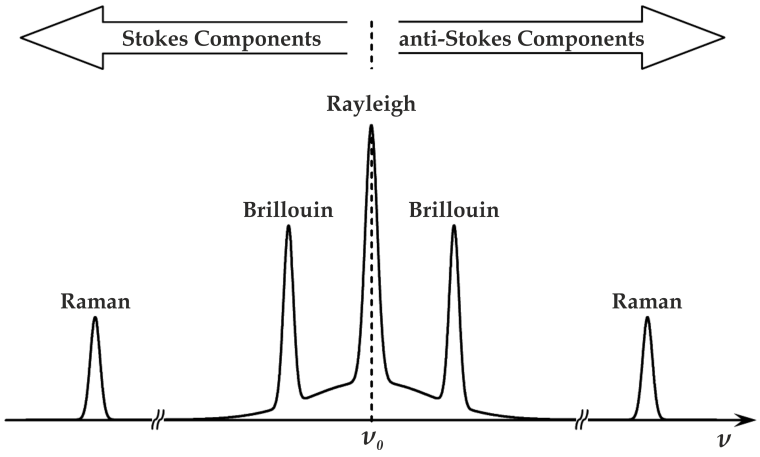

Figure 2.5: *Different spectral components arisen from scattered light in an inhomogeneous medium.*

2.5.1.1 Spontaneous Brillouin Scattering

The spontaneous Brillouin scattering is based on the motion of a pressure wave (Δp), therefore we should analyze it from the acoustics point of view. The wave equation for the pressure wave can be written as [10]:

$$\frac{\partial^2 \Delta p}{\partial t^2} - \Gamma \nabla^2 \frac{\partial \Delta p}{\partial t} - v_a^2 \nabla^2 \Delta p = 0 \tag{2.65}$$

where Γ is the damping parameter and v_a is the acoustic velocity in the medium, that can be expressed as:

$$v_a = \sqrt{\frac{K}{\rho}} = \sqrt{\frac{1}{C_s \rho}} \tag{2.66}$$

where K is the bulk modulus, ρ is the density of the medium and C_s is the adiabatic compressibility [7].

The intensity of the acoustic wave varies spatially as:

$$|\Delta p(z)|^2 = |\Delta p(0)|^2 \exp(-\alpha_a z) \tag{2.67}$$

where α_a is the acoustic absorption coefficient:

$$\alpha_a = \frac{|\mathbf{q}|^2 \Gamma}{v_a} = \frac{\Gamma_B}{v_a} \tag{2.68}$$

where $\Gamma_B = |\mathbf{q}|^2 \Gamma$ is the acoustic damping coefficient, which is inversely proportional to the acoustic damping time (τ_p) or average lifetime of the acoustic phonon in the medium:

$$\tau_p = \frac{1}{\Gamma_B} \tag{2.69}$$

The light, is therefore scattered by these acoustic waves, which field obeys the driven wave equation [7]:

$$\nabla^2\mathbf{E} - \frac{n^2}{c^2}\frac{\partial^2\mathbf{E}}{\partial t^2} = \mu_0\frac{\partial^2\mathbf{P}}{\partial t^2} \tag{2.70}$$

where n is the refractive index of the medium, c is the speed of light in vacuum and μ_0 is the magnetic permittivity in vacuum. The polarization $\mathbf{P}$ will depend on the density variation Δp of the thermally excited pressure disturbance:

$$\Delta p = \Delta p_0 \exp[i(-\mathbf{q}\cdot\mathbf{r} - \Omega_a t)] + c.c. \tag{2.71}$$

where $\Omega_a = v_a\,|\mathbf{q}|$, which is the frequency of the acoustic wave, is satisfied being $\mathbf{q}$ the scattered wavevector.

The scattered field from a incident monochromatic lightwave suits the following equation if equation 2.71 is substituted in equation 2.70:

$$\begin{aligned}\nabla^2\mathbf{E} - \frac{n^2}{c^2}\frac{\partial^2\mathbf{E}}{\partial t^2} = -\frac{\gamma_e C_s}{c^2}\{&(\omega-\Omega_a)^2 E_0\Delta p^* \exp[i(\mathbf{k}-\mathbf{q})\cdot\mathbf{r} - i(\omega-\Omega_a)t] + \\ &+(\omega+\Omega_a)^2 E_0\Delta p \exp[i(\mathbf{k}+\mathbf{q})\cdot\mathbf{r} - i(\omega+\Omega_a)t] + c.c.\}\end{aligned} \tag{2.72}$$

where E_0, ω and $\mathbf{k}$ are the amplitude, frequency and wavevector of the incident light respectively. γ_e is the electrostrictive constant and comes determined by:

$$\gamma_e = \left(\rho\frac{\partial\epsilon}{\partial\rho}\right)_{\rho=\rho_0} \tag{2.73}$$

The Brillouin Stokes and anti-Stokes scatterings are represented through a wavevector and a frequency that can be obtained from the right side of equation 2.72:

- Stokes Scattering: $\mathbf{k}' = \mathbf{k} - \mathbf{q}$ $\omega' = \omega - \Omega_a$
- anti-Stokes Scattering: $\mathbf{k}' = \mathbf{k} + \mathbf{q}$ $\omega' = \omega + \Omega_a$

where the wavevector and the frequency are related through:

$$\omega = |\mathbf{k}|\,\frac{c}{n} \qquad\qquad \omega' = |\mathbf{k}'|\,\frac{c}{n} \tag{2.74}$$

As it can be seen, energy and momentum conservation should be fulfilled, which means that the frequency and the wavevector of both incident light and acoustic vector should have particular magnitudes and directions. The representation of the mentioned structure can be observed in Figures 2.6 and 2.7 for the Brillouin Stokes and anti-Stokes scatterings respectively [7].

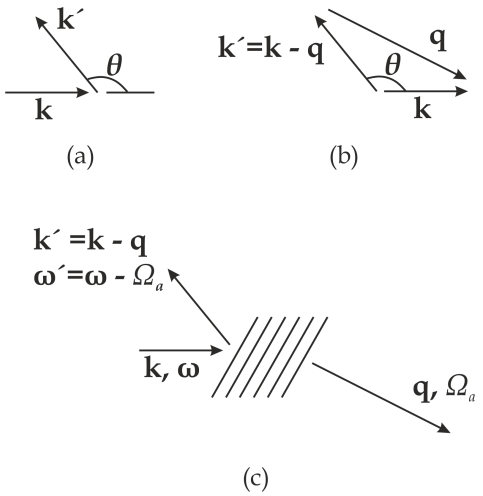

Figure 2.6: *Illustration of the Brillouin Stokes scattering.*

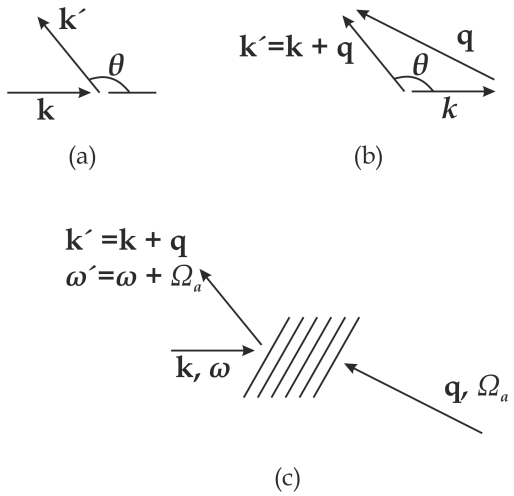

Figure 2.7: *Illustration of the Brillouin anti-Stokes scattering.*

On one hand, Figures 2.6(a) and 2.7(a) show the relative orientation of the incident and scattered fields, and on the other hand Figures 2.6(b) and 2.7(b) show the relation between the wavevectors of the acoustic, incident and scattered waves. Therefore, it can be appreciated that the Stokes or anti-Stokes components manifest as a scattering of light from an acoustic wave co- and counter-propagating to the incident light (Figures 2.6(c) and 2.7(c) respectively).

It can be assumed that $|\mathbf{k}'| \approx |\mathbf{k}|$ for both Stokes and anti-Stokes components since the acoustic wave (Ω_a) has a much smaller frequency than the optical waves. Therefore, the acoustic frequency can be expressed as:

$$\Omega_a = 2\,|\mathbf{k}|\,v_a sin\left(\frac{\theta}{2}\right) = \frac{4\pi n v_a}{\lambda_p} sin\left(\frac{\theta}{2}\right) \tag{2.75}$$

Equation 2.75 shows that the frequency shift depends on the scattering angle. Since in a single mode fiber, the only relevant directions are the forward and backward directions, the maximum frequency (Ω_B) will be in the backward direction ($\theta = \pi$) and it vanishes in the forward direction ($\theta = 0$). That is why Brillouin scattering arises only in the backward direction. The Brillouin Frequency Shift (BFS) of the backward scattered wave is represented by:

$$\nu_B = \Omega_B/2\pi = \frac{2nv_a}{\lambda_p} \tag{2.76}$$

Due to the finite duration of the phonon life (equation 2.69), it should be noted that in the frequency domain, the Brillouin components are not strictly monochromatic (see Figure 2.8) and suit a Lorentzian spectral profile given by [1]:

$$S(\nu) \propto \frac{(\Delta\nu_B/2)^2}{(\nu_0 - \nu_B)^2 + (\Delta\nu_B/2)} \tag{2.77}$$

where $\Delta\nu_B = \Gamma_B/2\pi$ is the Full-Width at Half Maximum (FWHM) Brillouin spectral linewidth.

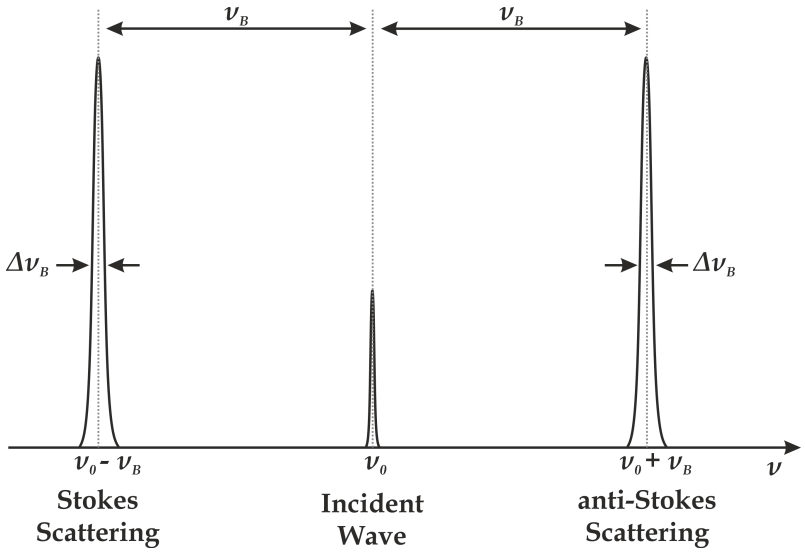

Figure 2.8: *Graphical representation of the spontaneous Brillouin backscattering spectrum.*

In Table 2.1 the typical values of Brillouin shift (ν_B) and linewidth ($\Delta\nu_B$) for Brillouin spectrum are detailed at different standard telecommunication windows [11]:

Wavelength [ν_0] (nm)	Brillouin Shift [ν_B] (GHz)	Brillouin Linewidth [$\Delta\nu_B$] (MHz)
514	34	100
832	22	70
1320	13	35
1550	11	30

Table 2.1: *Standard Brillouin scattering values for SMF at different wavelengths.*

2.5.1.2 Spontaneous Raman Scattering

As stated in the previous subsection (2.5.1.1), Brillouin scattering arises due to density variations within the medium. In the case of Raman scattering, it occurs by the interaction of light with resonant modes of the molecules in the medium. Since the molecule's modes can be vibrational or rotational, the Raman scattering can manifest in such ways; vibrational Raman scattering or rotational Raman scattering. Nonetheless, the vibrational mode is dominant over the rotational mode when generating the Raman scattering [12].

The typical description of the Raman scattering is usually done in terms of quantum energy levels. If a molecule located in a ground level vibrational state (state '1' in Figure 2.9(a)) is excited by an incident photon with an ω_p frequency to an intermediate virtual state, the photon will be absorbed and consequently a new photon will be emitted at frequency ω_S and a phonon will be reflected at Ω_R. Since the energy should be conserved, ω_S, that corresponds to the Stokes Raman scattering (Figure 2.9(a)), will equal to $\omega_S = \omega_p - \Omega_R$, where Ω_R is the frequency associated to the vibrational mode. If the molecule already has a vibrational energy (state '2' in Figure 2.9(b)), the incident photon is able to absorb an amount of energy from the medium, which turns into an upshifted frequency photon ($\omega_{AS} = \omega_p + \Omega_R$). This process corresponds to the anti-Stokes Raman scattering (Figure 2.9(b)).

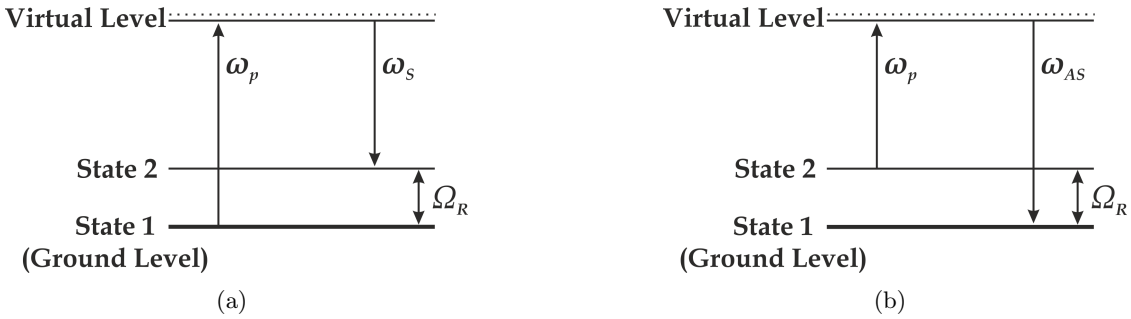

Figure 2.9: *Illustration of the spontaneous Raman scattering processes; Stokes scattering (a) and anti-Stokes scattering (b).*

The Raman Frequency Shift (RFS) in optical fibers ($\simeq 13$ THz) is about three orders of magnitude higher than the BFS ($\simeq 11$ GHz). This arises since in the quantum mechanical approach, the vibrational modes are represented by optical phonons, which actually have much higher energy than the acoustic phonons involved in the Brillouin scattering.

The transition rate for the Stokes and anti-Stokes process (W_S and W_{AS} respectively) due to thermal excitation is proportional to [13]:

$$W_S \propto N_0(1 + N_\Omega) \tag{2.78}$$

$$W_{AS} \propto N_0 N_\Omega \tag{2.79}$$

where N_0 is the incident photon number, proportional to the light intensity (i.e. $N_0 \propto |E_0|^2$) and N_Ω is the Bose-Einstein thermal population factor:

$$N_\Omega = \frac{1}{\exp(h\nu_R/k_B T_{abs}) - 1} \tag{2.80}$$

where h is the Planck constant, k_B is the Boltzmann factor, ν_R is the vibrational frequency and T_{abs} is the absolute temperature. The ratio of the unbalance between the Stokes and anti-Stokes intensities is $\exp(-h\nu_R/k_B T_{abs})$, which demonstrates that the anti-Stokes components tend to equal the Stokes component at high temperatures and that disappears when T_{abs} tends to 0.

This property has been used to develop distributed temperature sensors, where the Raman anti-Stokes intensity is used to identify the temperature distribution and the Stokes component, which is practically temperature independent [14], can be employed as reference for local loss variations.

2.5.2 Nonlinear or Stimulated Scattering Effects

In the previous subsection (section 2.5.1), spontaneous scattering effects were discussed, where the induced polarization is proportional to the applied field. As stated, this only arises when the properties of the medium remain unchanged, i.e. the incident light intensity is low. In case the applied electric field is high, the nonlinear material response to the light should be taken into account [7].

Thus, the scattering processes generated by thermal or quantum-mechanical fundamental effects are labeled as Spontaneous and the effects generated due to high-intensity light presence are denominated Stimulated, where the stimulated processes (e.g. Stimulated Brillouin Scattering (SBS) or Stimulated Raman Scattering (SRS)) are more efficient than the spontaneous ones.

Considering a high light intensity, the polarization will follow the nonlinear function described in equation 2.8, which derives into the following perturbed wave based on equation 2.30 [12].

$$\nabla^2\mathbf{E} - \frac{n^2}{c^2}\frac{\partial^2\mathbf{E}}{\partial t^2} - \frac{\alpha n}{c}\frac{\partial\mathbf{E}}{\partial t} = \mu_0\frac{\partial^2\mathbf{P}_{NL}}{\partial t^2} \tag{2.81}$$

where n is the refractive index of the medium, c is the speed of light in vacuum and μ_0 is the magnetic permittivity in vacuum.

Stimulated scattering effects such as SBS or SRS are the main fundamental processes employed in order to create the sensors developed along this thesis dissertation, therefore they will be analyzed in independent sections.

2.6 Stimulated Brillouin Scattering - SBS

In a SBS process, an intense coherent light (e.g. laser pump) enhances the scattering process. In this enhancing process photons from the source are annihilated producing an exponential enhancement in the Stokes wave due to an equivalent exponential growth of the amplitude of the acoustic wave.

SBS can be originated by two mechanisms:

- Brillouin Generator: In this case no external wave is introduced to the medium. The SBS arises from the generation of the spontaneous Brillouin scattering Stokes wave which is going to be recurrently amplified.
- Brillouin Amplifier: This procedure, in which is mainly based this thesis work, consists on introducing an external wave, usually known as probe wave in a counter-propagating direction to the pump signal. The probe wave will be amplified if its frequency equals the Brillouin Stokes frequency.

During this procedure, as stated in the first paragraph, the acoustic wave can be controlled by an optic wave through two different mechanisms; the electrostriction and the optical absorption. The optical absorption only arises in lossy media [7], therefore electrostriction appears to be the proper mechanism in optical fibers for the generation of SBS.

2.6.1 Electrostriction

The predisposition of some elements, such as silica, to compress in the presence of an electric field is known as electrostriction. At the same time, the electrostriction is related to the phenomenon where molecules are liable to move or re-orientate under the presence of an electric field in order to maximize their potential energy. If we consider that the

force acting over molecules (**F**) is acting just over a unique molecule (macroscopic point of view), under the presence of an electric field (**E**) the molecule develops a dipole moment that increases its potential energy (Δu) [7], therefore:

$$\Delta u = \frac{1}{2}\Delta\epsilon_{var} \left|\mathbf{E}\right|^2 \tag{2.82}$$

where $\Delta\epsilon_{var}$ is the variation of the dielectric permittivity and $\left|\mathbf{E}\right|^2$ is proportional to the intensity of the electric field. Therefore, the force acting over the dipole is given by:

$$\mathbf{F} = -\nabla u = \frac{1}{2}\epsilon_0\alpha_p\nabla(\mathbf{E}^2) \tag{2.83}$$

where ϵ_0 is the permittivity in free space and α_p is the molecular polarizability.

The **F** force produces an internal pressure known as electrostrictive pressure (p_{el}). When the media is compressible, the electrostrictive force produces a densification (Δp) with respect to the average medium density, as well as a molecular displacement [7]. Therefore, the dielectric constant varies in the following way:

$$\Delta\epsilon_{var} = \frac{\partial\epsilon}{\partial p}\Delta p \tag{2.84}$$

where the work per unit developed by the force compressing the material is proportional to the electrostrictive pressure (p_{el}) as a function of the intensity of the electric field:

$$p_{el} = -\frac{1}{2}\rho_0\frac{\partial\epsilon}{\partial p}\left|\mathbf{E}\right|^2 = -\frac{1}{2}\epsilon_0\gamma_e\mathbf{E}^2 \tag{2.85}$$

being γ_e the electrostrictive constant that equals $\rho(\partial\epsilon/\partial\rho)$.

By inserting the electrostrictive pressure (p_{el}) from equation 2.85 in equation 2.72, it provides coupled-wave field equations for the three waves present on the SBS interaction: pump, probe and acoustic wave, which lead to the coupled intensity equations represented in the forthcoming subsection 2.6.3.

2.6.2 Stimulated Brillouin Scattering through Electrostriction

Electrostriction is the necessary mechanism to generate SBS in fiber optics since it can create a great amount of acoustic phonons. The produced stimulation is enhanced with the beating between the pump wave and the corresponding counter-propagating signal; the Stokes wave in case of Brillouin generator or the probe wave when talking about the Brillouin amplifier.

In case of the Brillouin generator, the frequency shift equals to the one obtained in equation 2.76 and for the Brillouin amplifier comes set by the difference between the pump and probe waves:

- Brillouin Generator: $\nu_B = 2nv_a/\lambda_p$
- Brillouin Amplifier: $\nu_B = \nu_p - \nu_S$

In order to describe the SBS generation we can define it as the nonlinear interaction among a pump wave with ν_p frequency and a counter-propagating Stokes wave with ν_S frequency. When the frequency of the resulting field from the beating of both signals equals the Brillouin shift of the medium an acoustic wave is generated through electrostriction. This acoustic wave modulates the refractive index of the medium creating a grating that scatters the pump wave through Bragg diffraction [15]. Due to the associated Doppler effect (the grating moves at acoustic velocity (v_a)), the scattered light is downshifted in frequency an amount determined by the Brillouin shift of the material. The Stokes signal will be therefore amplified by the transfer of the scattered light, which in turn strengthens the acoustic wave. This process is repeated cyclically since the Stokes wave and the acoustic wave reinforce mutually. The anti-Stokes signal will be emptied in benefit of the pump wave. Figure 2.10 illustrates the positive feedback loop that leads to the generation of SBS through electrostriction.

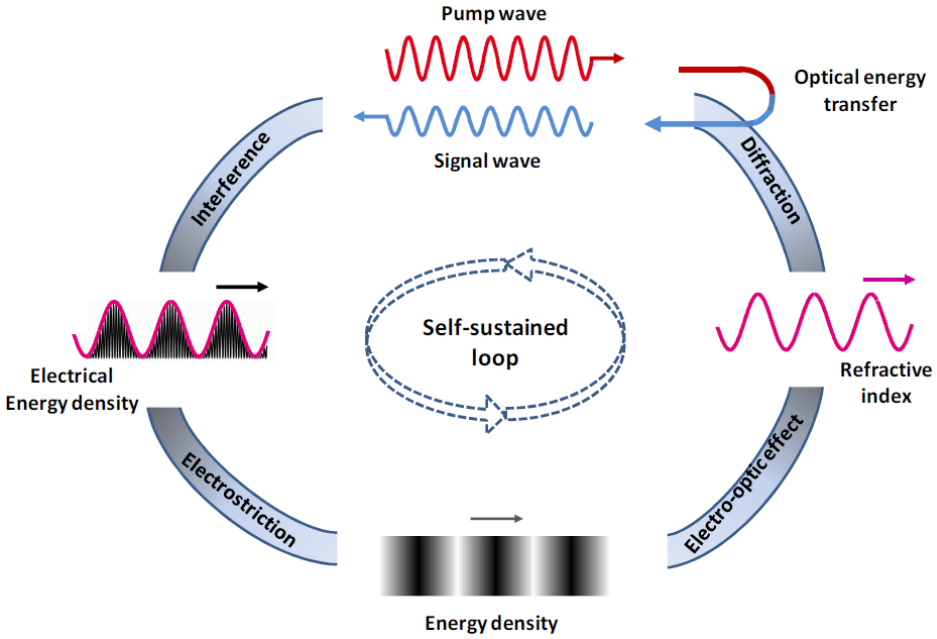

Figure 2.10: *Depiction of the generation of SBS through electrostriction [16].*

In this case, the generated Brillouin components will follow the already cited Lorentzian profile (see equation 2.77), where the peak value of the Brillouin gain coefficient will be expressed as [1]:

$$g_B(\nu) = g_{B0}\frac{(\Delta\nu_B/2)^2}{(\nu_0 - \nu_B)^2 + (\Delta\nu_B/2)} \tag{2.86}$$

where $g_{B0} = g_B(\nu_B)$ is the maximum gain at resonance, defined by:

$$g_{B0} = \frac{8\pi^2\gamma_e^2}{n_p\lambda_p^2\rho_0 c v_a \Gamma_B} \tag{2.87}$$

where $\gamma_e \approx 0.902$ is the electrostricitive constant of silica, $\rho_0 \approx 2210$ kg/m^2 is the density of silica fibers, λ_p is the wavelength of the incident light and n_p is the refractive index at λ_p [1].

2.6.3 Coupled Intensity Equations for SBS

Under steady-state conditions, applicable for a Continuous Wave (CW) or quasi-CW pump [1], SBS is governed by two coupled equations, considering as CW when any present perturbation is greater than the acoustic damping time of the medium (τ_p). First, it is necessary to consider the counter-propagating nature of the Stokes wave with respect to the pump. Second, if relatively small Brillouin shifts are assumed ($\omega \equiv \omega_p \approx \omega_S$), as well as same fiber losses for both pump and Stokes waves ($\alpha \equiv \alpha_p \approx \alpha_S$), the following expressions are obtained [1]:

$$\frac{dI_p}{dz} = -g_B(\nu) I_p I_S - \alpha I_p \tag{2.88}$$

$$\frac{dI_S}{dz} = -g_B(\nu) I_p I_S + \alpha I_S \tag{2.89}$$

The produced interference will depend on the relative polarization alignment among the interacting waves; I_p and I_S. On one hand, if no alignment is present, no interference will be produced and, on the other hand, with total alignment, maximum interference will arise. Therefore, with polarization diversity schemes, as will be described in forthcoming sections, the Brillouin gain ($g_B(\nu)$) will be reduced by a factor of 1.5 [17].

2.6.4 SBS Threshold

When estimating the Brillouin threshold, pump depletion can be neglected, which derives into an exponential decay of the pump wave, thus:

$$I_p(z) = I_p(0) \exp(-\alpha z) \tag{2.90}$$

expression that substituted in equation 2.88 and integrating it over the fiber length (L), provides the Stokes intensity, that grows exponentially in the backward direction:

$$I_S(0) = I_S(L) \exp(g_B(\nu) I_p(0) L_{eff} - \alpha L) \tag{2.91}$$

where L_{eff} is the effective interaction length, already expressed in equation 2.47. It is important to mention that when a pulsed signal is employed as pump wave, L_{eff} is dependent on the pulse width:

$$L_{eff} = \frac{v_g T_0}{2} \tag{2.92}$$

where v_g is the group velocity and T_0 the pulse width.

Equation 2.91 shows that the Brillouin Stokes wave increments exponentially as long as it travels through the fiber in the backward direction because of Brillouin amplification occurring as a result of SBS. Unless the Brillouin amplifier configuration is employed, the Stokes signal is no fed, so it grows from noise or spontaneous Brillouin scattering. This, is equivalent to injecting a fictitious photon per mode at a distance where the gain exactly equals the fiber loss [1]. Therefore, the Brillouin threshold (P_{th}^{SBS}) is found to follow [18]:

$$P_{th}^{SBS} \approx 21 \frac{A_{eff}}{g_B(\nu) L_{eff}} \tag{2.93}$$

If typical optical communication values for fibers are used at 1550 nm ($A_{eff} = 50\mu m^2$, $L_{eff} \approx 20$ km and $g_B = 5 \times 10^{-11}$ m/W), the Brillouin threshold will be ~ 1 mW, what makes SBS a dominant non-linear process [1].

2.7 Stimulated Raman Scattering - SRS

As mentioned in subsection 2.5.1.2 in Raman scattering the optic waves interact with the molecular vibrational states of the materials molecules. If an incident wave excites a molecule, its vibration will vary the refractive index of the media at the natural vibration frequency (Ω_R). As demonstrated in subsection 2.5.1.2, this process generates two side-bands (Stokes and anti-Stokes) around the pump wave (see Figure 2.11 (a)). If another field is introduced (Stokes wave) propagating at $\omega_S = \omega_p - \Omega_R$ frequency (see Figure 2.11 (b)) the pump and the Stokes waves can beat with each other modulating at the same time the total intensity of the vibration.

The modulated intensity coherently excites the molecular oscillation at $\Omega'_R = \omega_p - \omega_S$, that at the same time amplifies the Stokes wave, becoming into a self-sustained feedback process that generates a stronger molecular vibration and an amplified Stokes field.

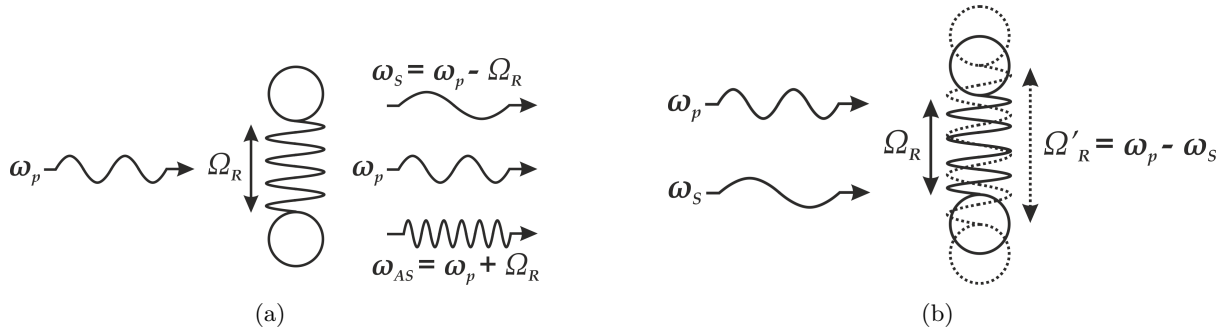

Figure 2.11: *Illustration of the SRS processes; Raman generator (a) and Raman amplifier (b).*

Compared to the SBS process, SRS can amplify the Stokes signals in a co- and counter-propagating way, where SBS can only excite in opposite direction.

As the SBS (2.6), SRS can be generated through two different processes, based on the description developed in the previous paragraphs:

- Raman Generator: A strong enough pump wave is launched within the fiber creating a spontaneous Raman scattering light. This component, that will act as a probe beam, will be re-amplified in a distributed way all along the optical fiber.

- Raman Amplifier: A co- or counter-propagating wave is introduced within the fiber at $\omega_S = \omega_p - \Omega_R$ frequency. This wave will excite the vibrational modes generating amplification on the Stokes component.

2.7.1 Raman Gain Spectrum

Based on the same approach as done in subsection 2.6.3, the Stokes wave is described by [7]:

$$\frac{dI_S}{dz} = g_R(\Omega) I_p I_S \tag{2.94}$$

where I_S is the Stokes intensity, I_p is the pump intensity and g_R is the Raman gain coefficient. The Raman gain spectrum ($g_R(\Omega)$), where Ω represents the frequency difference between the pump and Stokes waves, is the most important quantity when describing SRS. It depends on the composition of the material, which makes it vary depending on the present dopant [1]. One of the most significant features the Raman gain curve in silica fibers is that it extends up to 40 THz with a broad peak located at $\sim$ 13 THz (see Figure 2.12).

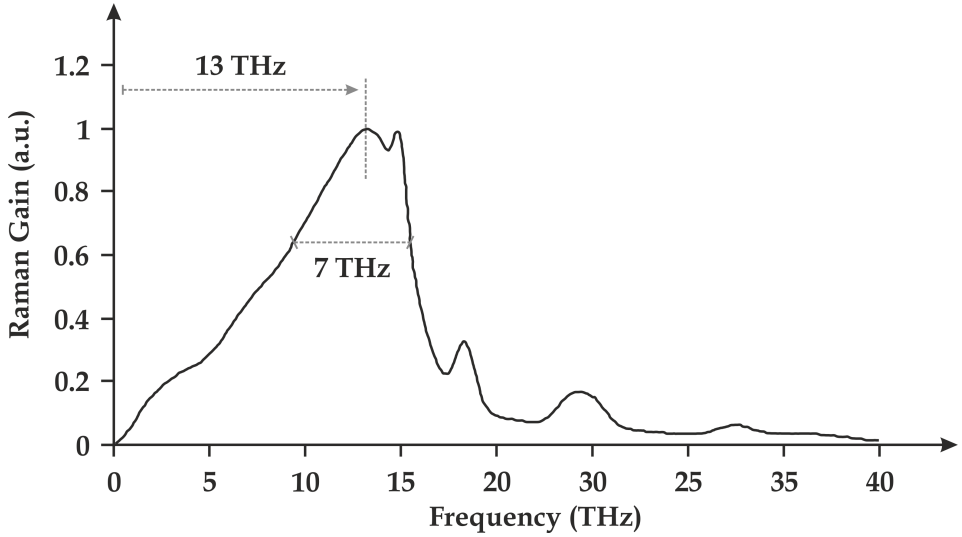

Figure 2.12: *Representation of the Raman gain trace.*

In this thesis dissertation, as will be explained in forthcoming sections, the gain profile will be employed for distributed amplification purposes. If a CW pump with ω_p frequency encounters a ω_S at the fiber input, it will be amplified as long as the frequency difference $\Omega = \omega_p - \omega_S$ is located within the Raman gain spectrum bandwidth. In an analogous way to SBS, is no Stokes component is present, the spontaneous Raman scattering acts as probe and is amplified with propagation. It is important to underline that, as the spontaneous Raman scattering generates photons within the entire bandwidth of the Raman gain spectrum, all frequency components are amplied [1].

2.7.2 Coupled Intensity Equations for SRS

Based on the coupled equations among the interaction of the pump and Stokes waves, SRS is governed by a set of two coupled equations in the CW case [1], as considered in subsection 2.6.3 for the SBS case:

$$\frac{dI_S}{dz} = g_R(\Omega) I_p I_S - \alpha_S I_S \tag{2.95}$$

$$\frac{dI_p}{dz} = -\frac{\omega_p}{\omega_S} g_R(\Omega) I_p I_S - \alpha_p I_p \tag{2.96}$$

where α_p and α_S are the fiber losses at the pump and Stokes frequencies respectively.

In the absence of losses ($\alpha_p = \alpha_S = 0$), and considering the processes trough which photons appear in and disappear from each beam, it can be merely concluded that the total number of photons in the pump and Stokes beams remains constant during SRS [1].

2.7.3 SRS Threshold

Even though pump depletion should be included for a complete description of the SRS, for the case of the SRS threshold it can be neglected, as done for the SBS case (see subsection 2.6.4) [18]. The first term on the right-hand of equation 2.96 is responsible for the pump depletion. If its solution is substituted in equation 2.95 and solved the result is:

$$I_S(L) = I_S(0) \exp(g_R(\Omega) I_0 L_{eff} - \alpha_S L) \tag{2.97}$$

where I_0 is the incident pump intensity at $z = 0$ and L_{eff} is the effective length as expressed in equation 2.47.

As equation 2.97 requires an input at $z = 0$ ($I_S(0)$), this is translated in practice as to injecting one fictitious photon per mode at the input end of the fiber. Therefore, the critical pump power to reach the Raman threshold (P_{th}^{SRS}) is given by [18]:

$$P_{th}^{SRS} = 16 \frac{A_{eff}}{g_R L_{eff}} \tag{2.98}$$

For standard telecommunication optical fibers employed at 1550 nm ($A_{eff} = 50 \mu m^2$, $L_{eff} \approx 20$ km and $g_R = 6.6 \times 10^{-14}$ m/W) the Raman threshold will be ≈ 600 mW for forward SRS. In the case of backward SRS the numerical factor 16 is replaced with 20 [1], therefore, P_{th-bw}^{SRS} will equal approximately 750 mW.

Chapter 3

BOTDA: Principles, Limitations and State of the Art

3.1 Introduction

This thesis dissertation deals with the improvement of Brillouin Optical Time Domain Analysis (BOTDA) systems in terms of range and resolution. That is why, in this chapter, it will be developed a proper description of the technique itself as well as its trade-offs when employing it as a distributed optical fiber sensor. Unfortunately, when intending to enlarge the range and/or the resolution of a BOTDA some associated issues arise, such as Modulation Instability (MI), pump depletion and Self-Phase Modulation (SPM). A full description of such phenomena will be developed and the proposed techniques to avoid them in terms of range (Raman amplification, pulse coding) and resolution (Differential Pulse-width Pair (DPP)) will also be addressed. Raman amplification also produces a non-desired effect as it produces a great Relative Intensity Noise (RIN) transfer to the probe wave. This phenomenon has also been identified as a major limitation in Raman-assisted BOTDA systems, so it will be properly addressed in this chapter too.

3.2 Brillouin Optical Time Domain Analysis - BOTDA

BOTDA is a fiber optic sensing technique that allows performing distributed measurements of strain and temperature over tens of kilometers with resolutions around 1-2 meters depending on the sensing length. At the heart of the technique is the Stimulated Brillouin Scattering (SBS) interaction, already described in section 2.6. The measurements of strain and temperature are linked to the fact that these magnitudes have a linear dependence to the frequency variation of the Brillouin Frequency Shift (BFS) [9, 19].

This measuring technique has attracted great interest in the academic and industrial sectors in the last two decades and it already has been applied for real sensing and monitoring field applications (e.g. buildings, pipelines, dams, etc.) demonstrating its performance and effectiveness.

3.2.1 BOTDA Sensing Technique

In its very beginning, the BOTDA was employed as a fiber attenuation measuring technique [20,21], substituting the widely known Optical Time Domain Reflectometry (OTDR) technique [22] due to its potential for improved performance in terms of Signal to Noise Ratio (SNR), range and resolution. Once the dependence of the BFS was related to the variation of strain and temperature, the BOTDA was utilized as a distributed fiber optic sensor [23, 24].

The original BOTDA setup can be observed in Figure 3.1. Its working principle is based on introducing within the Fiber Under Test (FUT) two counter-propagating light signals; a pulsed lightwave at $z = 0$ traveling in the $+z$ direction and a Continuous Wave (CW) at $z = L$ propagating in the $-z$ direction.

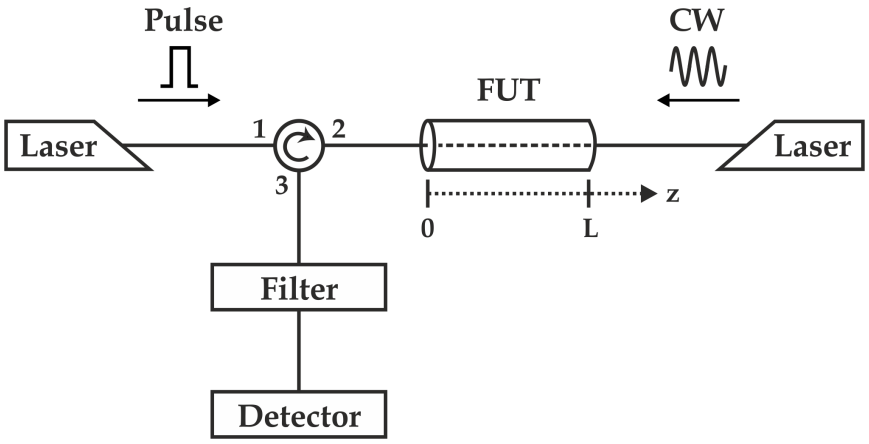

Figure 3.1: *Graphical representation of the first BOTDA [20]. FUT: Fiber Under Test; CW: Continuous Wave.*

Based on that structure (Figure 3.1) a BOTDA can operate in two different configurations [20]:

- Brillouin Gain: In this BOTDA structure, the pulsed wave (at ν_0 frequency) acts as the pump wave for the Brillouin amplification and the CW (at $\nu_0 - \Delta\nu$) as probe wave. The pump pulse generates a gain band which maximum frequency will be downshifted an amount equal to $\nu_0 - \nu_B$, where ν_B is the BFS (see Figure 3.2). When the probe wave offset equals the BFS, it is amplified by the SBS interaction. Therefore, temperature or strain variations within the fiber that vary the Brillouin amplification of the CW can be measured at the fiber input ($z = 0$) as a function of the frequency difference among the pump and probe waves ($\Delta\nu$) [19].

- Brillouin Loss: In this configuration, the pulsed signal (at ν_0) acts as the probe wave. Therefore, the CW is the pump wave of the SBS process, and it will be necessary to be positioned at $\nu_0+\nu_B$ frequency (see Figure 3.2) [25,26]. Identically to the Brillouin gain configuration, when the frequency difference between both waves equal the BFS, a Brillouin amplification will arise, although in this case it is the pulse which is amplified at the expense of the CW depletion. Therefore, temporal variations of the CW intensity can be measured at $z = 0$ in form of depletion or loss induced by SBS interaction with the pulse, which provide distributed profiles of strain and temperature. To be able to retrieve proper depletion avoiding distortion on the traces it is necessary that the power level of the CW to be much lower than the pulsed signal [27], which constitutes a drawback when ranging long fiber distances.

In both configurations, in order to fully recover the full spectrum of the interaction, it is necessary to develop a sweep of the $\Delta\nu$ frequency difference with respect to the CW intensity variations. The BFS is determined by adjusting the obtained Brillouin Gain Spectrum (BGS) to a fit that suits the Lorentzian profile of the BGS (see equation 2.86).

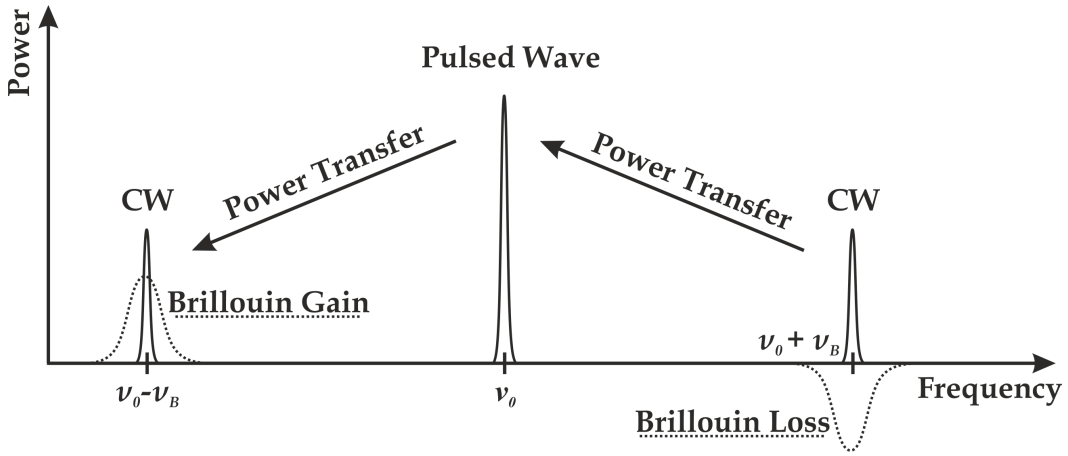

Figure 3.2: *Generation of the Brillouin Gain ($\nu_0 - \nu_B$) and Brillouin Loss ($\nu_0 + \nu_B$) curves.*

The spatial resolution of the system is defined as the smallest fiber section over which any sensible variation can be detected. In a BOTDA it will be directly proportional to the temporal width of the employed pulses, as expressed in the following equation:

$$\Delta z = \frac{1}{2}\frac{c}{n}T_0 \simeq T_0 \cdot 10^8 \tag{3.1}$$

where T_0 is the pulse width in seconds and it has been considered that the speed of light in vacuum equals $c = 3 \cdot 10^8$ m/s and that the refractive index of a standard Single Mode Fiber (SMF) is $n \simeq 1.45$. Therefore, the resolution of the system follows the relationship of ~ 1 meter per every 10 ns.

The linear dependence of the BFS with strain ($\Delta\epsilon$ - Figure 3.3(a)) and temperature (ΔT - Figure 3.3(b)) has already been reported in several publications, [9, 19] and follows the expression:

$$\Delta BFS = C_{\nu_B\epsilon}\Delta\epsilon + C_{\nu_B T}\Delta T \tag{3.2}$$

where $C_{\nu_B\epsilon} \simeq 505.5$ MHz/% and $C_{\nu_B T} \simeq 0.95$ MHz/°C at 1550 nm for typical SMFs.

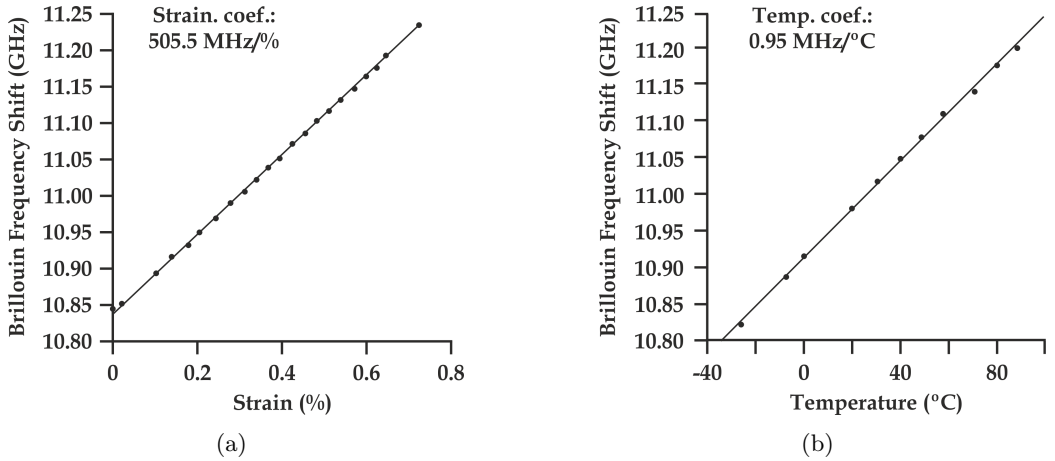

Figure 3.3: *BFS dependence on strain (a) and temperature (b) for standard SMFs at 1550 nm [9].*

In Figure 3.4 it has been schematized the operating mode of a BOTDA sensor working in the Brillouin Gain configuration.

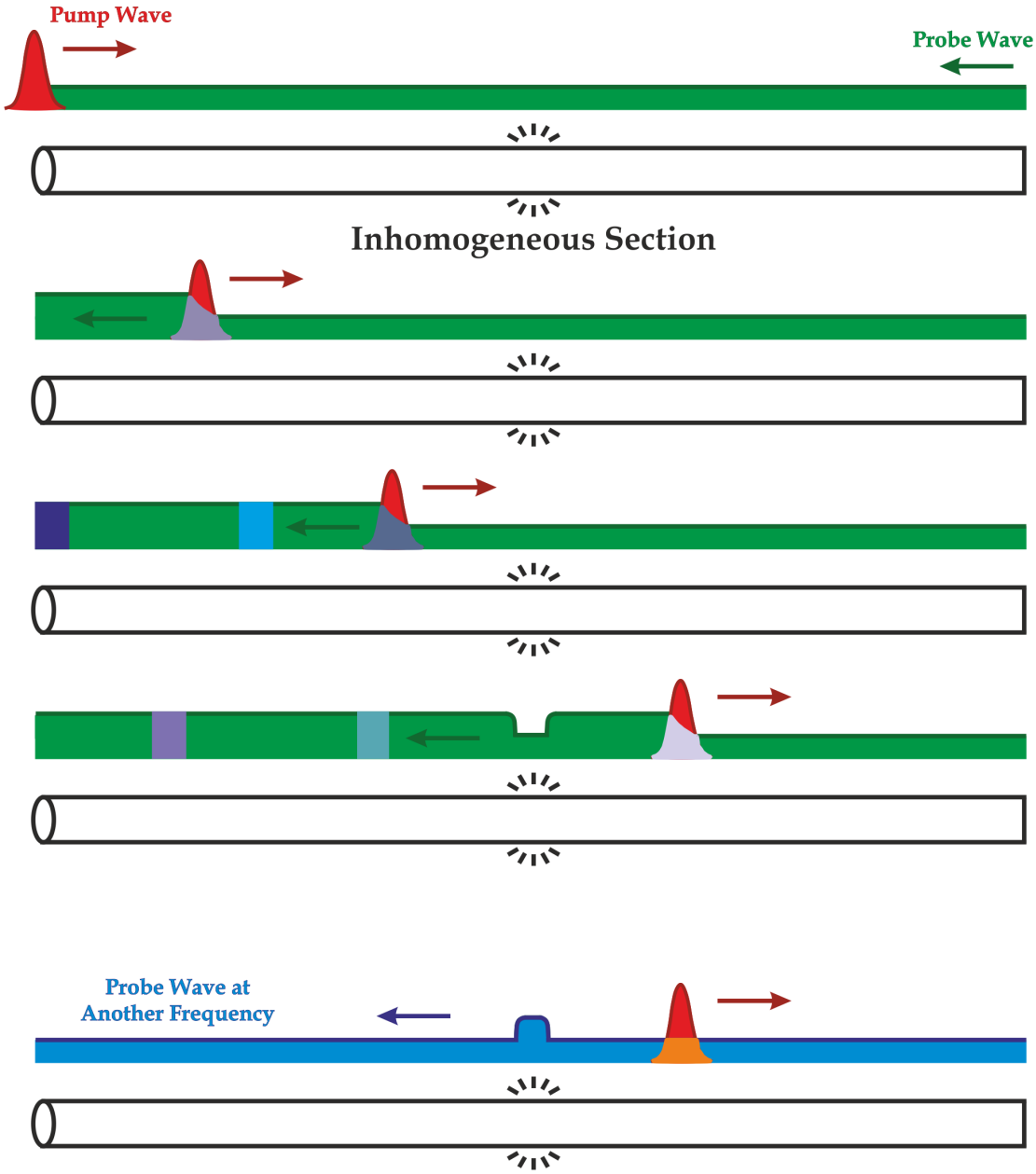

Figure 3.4: *Graphic representation of the BOTDA operation mode in the Brillouin Gain configuration. As long as the frequency difference among the pump and probe waves equals the BFS of the fiber, the probe will be amplified, unless the fiber has an inhomogeneous section (different strain or temperature), where the BFS will be different. Therefore, the amplification of the probe wave at that region will be produced at a different frequency, making possible the determination of the position and the magnitude of the inhomogeneity.*

In conclusion, the BOTDA sensing technique employs the SBS non-linear effect to develop measurements based on the pump-probe technique. A pulsed pump signal, intense enough to create a counter-propagating gain curve due to SBS within the target fiber, will interact locally with a weak CW probe wave introduced in opposite direction into the optical fiber.

The gain experienced at each location by the probe wave due to Brillouin amplification can be analyzed by recording the probe amplitude in the time domain [9]. The frequency difference between the pump and probe signals is analyzed and therefore the local amplification in a concrete inhomogeneous section can be determined. As shown in Figure 3.5, the complete gain spectrum can be reconstructed by studying the gain as a function of time and frequency.

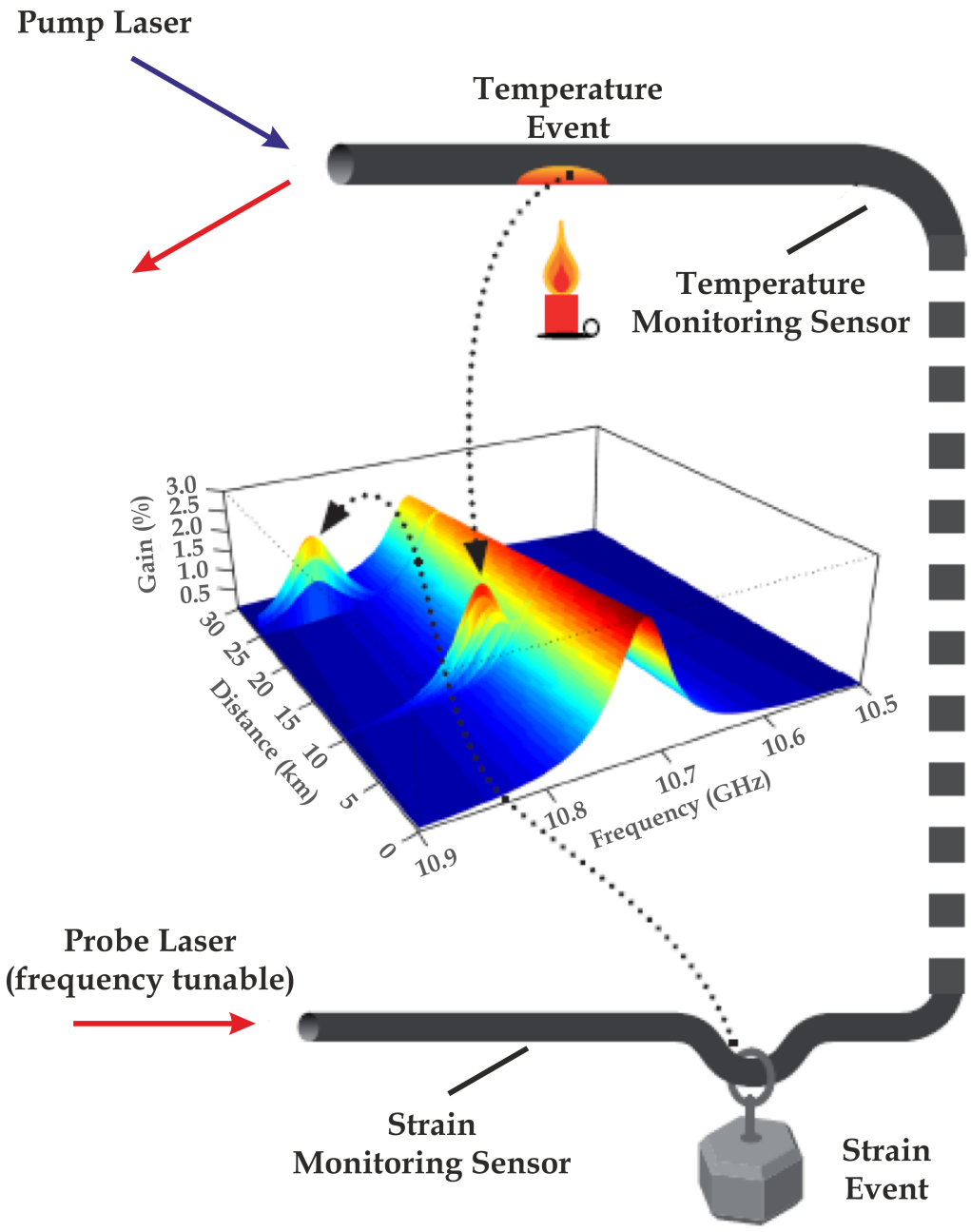

Figure 3.5: *Schematic drawing of the gain spectrum reconstruction of a BOTDA when strain and a temperature increase is applied to the fiber.*

3.2.2 BOTDA Theoretical Model

The coupled-wave equations for SBS obtained in subsection 2.6.3 can be applied to a BOTDA in order to describe the powers of the pulsed and CW signals (I_p and I_{CW} respectively) [1, 28]:

$$\frac{dI_p}{dz} = -g_B I_p I_{CW} - \alpha I_p \tag{3.3}$$

$$\frac{dI_{CW}}{dz} = -g_B I_p I_{CW} + \alpha I_{CW} \tag{3.4}$$

where $g_B(\nu)$ is the BGS and α is the fiber attenuation, already described in equations 2.86 and 2.19 respectively. In the case of the BGS at a specific fiber position, it is worth mentioning that it will depend on the polarization states of the light beams traveling within the fiber [17, 28, 29]:

$$g_B(z, \Delta\nu) = g_{B0} \frac{\gamma_f (\Delta\nu_B/2)^2}{(\nu - \nu_B)^2 + (\Delta\nu_B/2)} \tag{3.5}$$

where γ_f is the polarization factor [28].

Even though the expressions 3.3 and 3.4 are applicable for steady-state conditions, they can be transfered to the BOTDA model despite one of the signals is pulsed, since it can be considered that the pulse width is generally much longer than two times the phonon lifetime ($\sim$ 6 ns) [16]. In any other case, the full BOTDA model should be taken into account.

As stated previously, a BOTDA can work in Gain or Loss configuration. The first case arises when the pulsed signal transfers its power to the CW, setting a positive value for $g_B(\nu)$. On the other case, the power transfer is developed from the CW to the pulsed beam, where $g_B(\nu)$ will have a negative quantity. If we consider the Brillouin Gain case ($g_B(\nu) > 0$), the most employed model in long range BOTDA systems, a perturbation method can be employed to solve the system of equations 3.3 and 3.4 so the Brillouin gain received from a particular spatial location can be retrieved considering that only the fiber attenuation (α) affects the CW probe [28]:

$$I_{CW}(z) = I_{CW}(L) \exp[-\alpha(L - z)] \tag{3.6}$$

where $I_{CW}(L)$ is the input power of the CW probe and L is the sensing length. If equation 3.6 is substituted in equation 3.3 the pulsed wave has the following analytic solution:

$$I_p(z) = I_p(0) \exp(-\alpha z) G(z, \Delta\nu) \tag{3.7}$$

where $I_p(0)$ is the input peak power of the pulsed laser and $G(z, \Delta\nu)$ represents the depletion experienced by the pulsed beam due to Brillouin interaction, and comes represented by [29]:

$$G(z, \Delta\nu) = \exp\left(- \int_0^z g_B(z', \Delta\nu) I_{CW}(L) \exp[-\alpha(L - z')] dz' \right) \tag{3.8}$$

If equation 3.7 is substituted in equation 3.4, it can be integrated over Δz_i distance, interval in which the pulsed beam interacts with the CW [28, 29]:

$$\int_{I_{CW}(z)}^{I_{CW}(z+\Delta z_i)} \frac{dI_{CW}(z,\Delta\nu)}{I_{CW}(z,\Delta\nu)} = \int_{z}^{z+\Delta z_i} [-g_B(z',\Delta\nu)I_p(z',\Delta\nu)+\alpha]dz' \tag{3.9}$$

To recover the information of the BGS along the fiber, it is necessary to compare the CW light intensity with and without Brillouin interaction. This, expressed as a function of time (t) and frequency offset ($\Delta\nu$) and if considered that the gain factor (G) nearly equals 1 so the changes in the pulse intensity are mainly due to fiber attenuation (α) [14]:

$$\Delta I_{CW}(t,\Delta\nu) \propto \int_{tv_g/2}^{tv_g/2+\Delta z_i} g_B(z',\Delta\nu)Ip(z',\Delta\nu)dz' \tag{3.10}$$

where $0 < t < 2(L-\Delta z_i)/v_g$. This expression allows to directly reconstruct the BGS from measurements of the CW intensity, which has the same Lorentzian shape as the Brillouin gain coefficient ($g_B(\nu)$). Therefore, this allows to reconstruct the BGS as a function of distance by measuring the intensity contrast of the CW for different frequency offsets ($\Delta\nu$).

3.2.3 Standard BOTDA

The first distributed measurement developed through a BOTDA was developed in 1990 by Kurashima *et al.*, performing a 100 m spatial resolution sensing over 1.2 km of SMF with 3 °C of uncertainty [23]. More than twenty years have passed since then and nowadays, due to the improvements on developing BOTDA systems, usually it is possible to achieve a maximum sensing range of 50 km without any extra technique applied [30, 31]. In terms of resolution, the natural limit is given by the phonon lifetime ($\tau_p \sim 6$ ns), which sets the actual minimum resolution to ~ 1 m, as stated already in subsection 3.2.2.

One of the greatest improvements developed in the progress of BOTDA sensors, which considerably increased the stability of the measurements, was proposed by Niklès *et al.* [19,32]. As stated, the first BOTDA employed two different laser sources to generate both pump and probe signals (Figure 3.1). This configuration has a great disadvantage if the stability among the lasers is not kept since any frequency drift among the lasers will be translated as a variation of the Brillouin interaction. This turns into a decrease of the SNR or errors in the determination of the BFS.

All these issues where solved through the so-called Sideband Technique, which is based on employing a unique laser source for both pump and probe signals. The laser is modulated through an ultra-wideband integrated $LiNbO_3$ intensity Electro Optic Modulator (EOM) in order to obtain pulsed and frequency shifted double sideband waves, as shown in Figure 3.6.

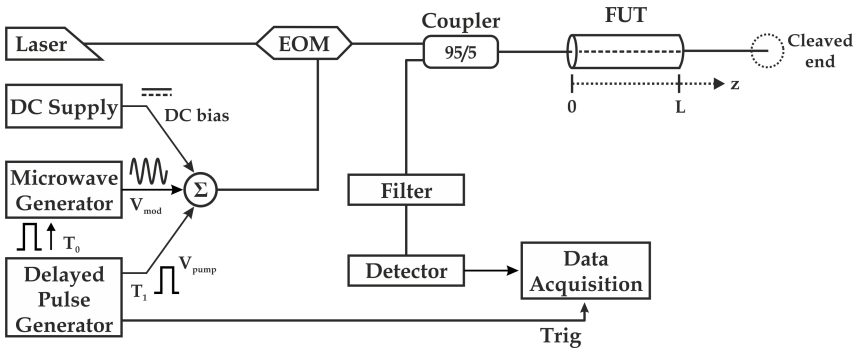

Figure 3.6: *Schematic of the Sideband Technique BOTDA [32]. DC: Direct Current; Trig: Trigger; Σ: Adder; EOM: Electro Optic Modulator; FUT: Fiber Under Test.*

The application of a microwave signal on the EOM creates equally spaced sidebands in the laser spectrum at f_m frequency (see Figure 3.7(a)). If the frequency separation of such sidebands (f_m) from the carrier wave (ν_0) equals the BFS ($\nu_B = \nu_0 \pm f_m \simeq 11$ GHz), the signal will be amplified or attenuated depending on its spectral location with respect to the probe. Therefore, if a frequency sweep with the sidebands is performed and the amplitude of the CW is recorded, the BGS can be reproduced at all the points along the fiber with good stability and SNR. This arises since the relative stability among the pump and probe waves is guaranteed.

From the cited modulation process, a minimum of three waves will be present within the fiber; two sidebands located at a frequency around the BFS (f_m) and the carrier wave (ν_0). In order to properly re-build the BGS it is necessary to develop a filtering process of the undesired waves at detection, among them the frequency sideband uninvolved in the Brillouin gain/loss process and ν_0. Rodriguez-Barrios *et al.* [33] proposed to use a "W" shaped Fiber Bragg Grating (FBG) [34] so the filtering of the undesired sideband and carrier can be done at the same time. Nowadays, usually, the non-wanted sidebands are filtered through a narrowband optical filter and the carrier element is suppressed by properly setting the Direct Current (DC) bias of the EOM. Figure 3.7(b) shows the spectrum of the modulated sidebands with the carrier element properly suppressed.

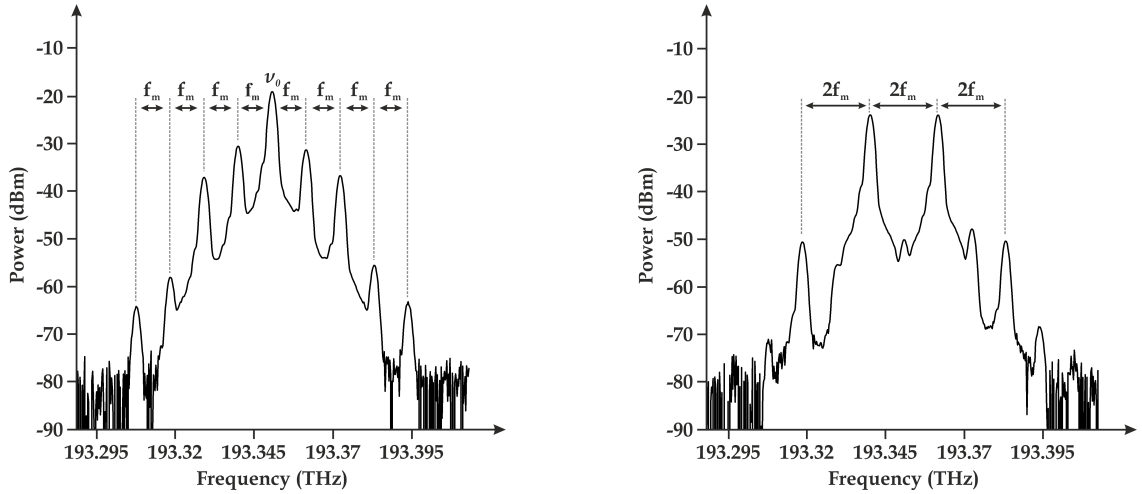

Figure 3.7: *Experimental representation of the probe wave sideband spectrum with the carrier frequency present (a) and with it suppressed (b).*

The use of a Single Sideband modulation scheme [35, 36] has already been tested and reported highlighting its benefits combined with different detecting schemes; Self-Heterodyne detection [37] and a Brillouin Loss configuration [38]. It is remarkable the Self-Heterodyne detection scheme since it considerably increases the SNR ($\sim$ 11 dB) but is also able to provide information concerning the Brillouin Phase Shift (BPS). This measurement method could be potentially beneficial in terms of RIN reduction in Raman-assisted systems as we will see in the forthcoming section 5.1.

3.3 Range Increase

As already mentioned, the increase of the sensing range could be directly linked to the increment of the power levels of the signals interacting within the sensing fiber. With increased power levels, the effect of fiber attenuation can be partially overcome. This procedure indeed improves the sensing range of relatively short range BOTDA systems ($<$ 50 km), but when trying to monitor above 50 km, as reported by Rodriguez-Barrios *et al.* [39] or Soto *et al.* [40], the performance of the system can be damaged due to associated detrimental effects; mainly MI and pump depletion. The path to avoid such drawbacks is set nowadays on the use of distributed First- [41–44] and/or Second-order Raman amplification [45–47] and/or pulse coding [40, 48–50]. Unfortunately, Raman amplification also introduces a substantial RIN transfer towards the probe wave. This is because the necessary Raman pumps, normally high power Raman Fiber Lasers (RFL), have a considerable RIN figure ($\sim$ -110 dBc/Hz). These devices have been widely employed to target long or ultra-long distances, thus RIN transfer is also considered as a major limitation when increasing the range of BOTDA systems. Recently, low noise lasers, such as Semiconductor Lasers (SL) ($\sim$ -140 dBc/Hz) have been developed that can provide high enough power levels, reducing the detrimental effect of RIN transfer [43, 44, 50], although for some extreme applications they are still not effective enough. Raman assistance and pulse coding were employed in some experimental setups of this PhD thesis and before a complete description is provided, it will be proper to describe in detail how MI and depletion affect the performance of BOTDA and Raman-assisted BOTDA distributed systems.

3.3.1 MI on BOTDA Systems

MI (subsection 2.4.1.2) is a phenomenon directly linked to the employed pump power and the dispersion of the optical fiber through which the signals travel [51, 52]. Since the fibers employed in Brillouin distributed sensing are usually long range standard SMFs with anomalous dispersion at 1550 nm, MI entirely depends on the pump power level creating a depletion of the pump signal, which manifests as the buildup of two sidebands at each side of the center beam wavelength [53]. Under this condition, a power exchange between the pump and the generated sidebands arise, a phenomenon known as the Fermi-Pasta-Ulam (FPU) recurrence [54]. The detrimental effect of MI in distributed fiber sensors has been studied by Alasia in his thesis dissertation [55], although in that case, the effect was studied by seeding two sidebands on the pump spectrum and observing their evolution with the input power [56]. For our particular case, as the pump and probe signals travel always in opposite directions, as explained in Figure 3.1, the generated sidebands due to MI are only seeded from noise. This process translates as a recurrent signal depletion.

As demonstrated by Martins *et al.* in [53] over 10 km, for pump powers < 26 dBm (400 mW), the effect of MI is negligible, as the pump wave contains 90 % of the total power. On the contrary, for higher power levels, the pump signal is depleted in favor of the generated noise sidebands. However, as already tested in several works dealing with FPU [54, 57] when either the range or the pump power is increased, the power transfer is reversed after certain distance which is translated as a power return from the sidebands to the central pump wave. After some more distance, the phenomenon again transfers power from the pump to the sidebands, and so on, resulting into an oscillatory power pattern in the pump pulse. This behavior can be observed on the simulation of Figure 3.8 [53], which can be obtained from the Non-Linear Schrödinger's Equation (NLSE) (see equation 2.44) and noise as a seed.

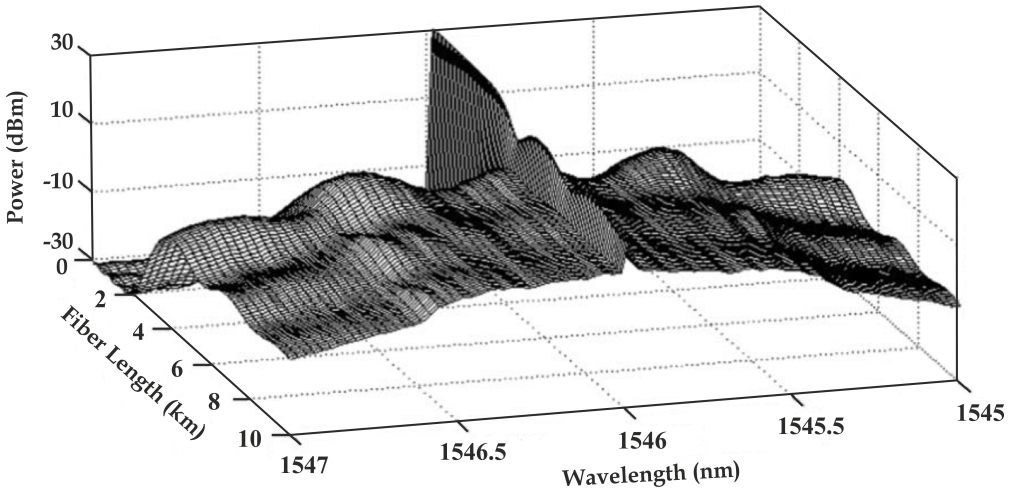

Figure 3.8: *Simulation of the input pulse spectrum evolution along 10 km under the effect of MI [53].*

The experimental evolution of the power transfers, from the sidebands to the central pump wave and vice versa, are detailed in Figure 3.9 at the end of the fiber, as a function of the pump power [53].

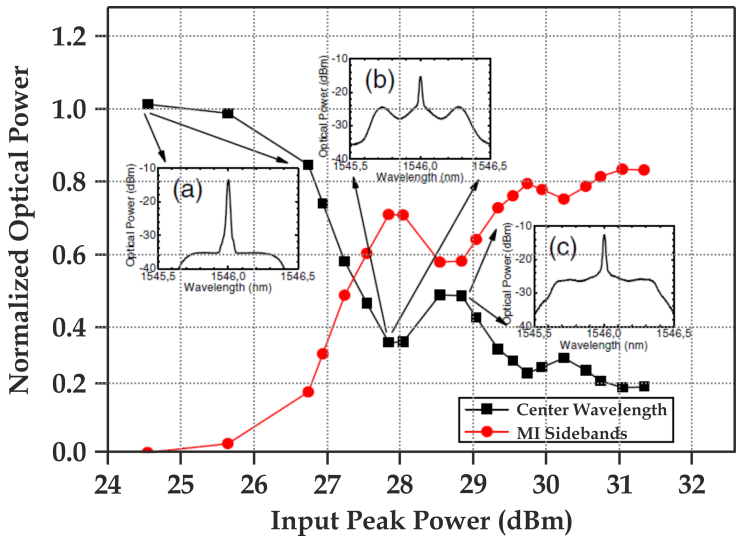

Figure 3.9: *Normalized optical power of the peak and sidebands at the end of the fiber for different input pump powers. Inset figures: spectrum for input pump powers of (a) 24.5, (b) 27.8, and (c) 28.8 dBm [53].*

3.3.2 Depletion

Pump depletion refers to the frequency-dependent loss of the pump due to the pump-probe power transfer. This effect has already been reported in several works [58–61] although it is Prof. Thévenaz *et al.* who have developed a detailed study of such phenomenon [62].

Depletion can be understood as a gradual power transfer from the higher frequency wave to the lower one. If we consider a Brillouin gain BOTDA configuration (pump wave is the pulsed wave and the CW is the amplified probe) the amplitude of the pump pulse will depend on the pump-probe frequency difference in presence of a cumulated energy transfer between the interacting waves [62]. As the pump pulse interacts continuously with the CW signal, this effect will be higher on it than on the CW since it only interacts with the other wave during the pulse length. Also, this effect will be more severe for the pump wave at the end of the fiber since the energy transfer is distributed all along the fiber.

Practically, the described dynamic is translated as an uncontrolled amplitude change of the pump pulse, which at the same time does not certify a constant pulse power when the pump-probe frequency difference is scanned. In conclusion, the measured BGS will be distorted, especially if the central Brillouin gain frequency is shifted with respect to the gain spectrum in the preceding fiber section, e.g. a temperature difference, fiber elongation, etc.

The quantity of the suffered depletion (d) can be expressed as [62]:

$$d = \frac{P_{p0} - P_p}{P_{p0}} \tag{3.11}$$

where P_{p0} is the pump power when no Brillouin interaction arises and P_p is the pump power under maximum Brillouin interaction. For the case of the Brillouin loss BOTDA the expression for the suffered depletion can be equally employed although d will have a negative sign.

As it can be seen in Figure 3.10 when a depleted pump wave is employed to scan the frequency difference ($\delta\nu$) of an inhomogeneous section of fiber, the measured gain frequency difference will have an error (ν_e) regarding to the real BGS.

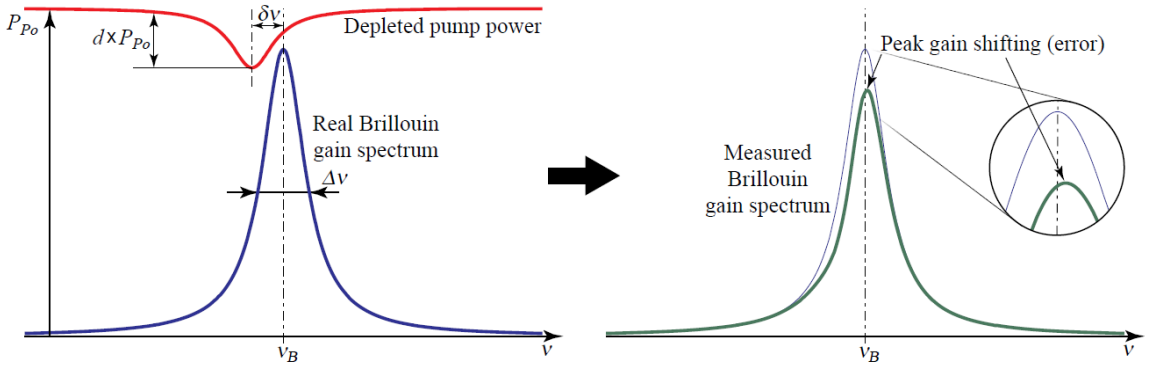

Figure 3.10: *Representation of the Brillouin pump depletion when trying to determine the BGS [62]. As represented on the right-hand figure, depletion causes a shift in the gain peak determination.*

The acceptable depletion coefficient (d) for a given tolerable systematic error (ν_e) of the measured Brillouin gain frequency can be expressed through the following expression if the systematic error is much smaller than the gain spectral width ($\Delta\nu$) [62]:

$$d_{max} = \frac{(1+4\xi^2)[16\xi e^2 - (1+4\xi^2)e]}{12\xi e^2 - 2(1+2\xi^2)e + \xi} \tag{3.12}$$

where $\xi = \delta\nu/\Delta\nu$ and $e = \nu_e/\Delta\nu$.

Considering the case of having two probe wave sidebands present simultaneously within the fiber, as the case of the Sideband Technique explained in subsection 3.2.3, the depletion factor d will be determined as follows [62]:

$$1 - d = \exp\left(\frac{g_B}{A_{eff}}(P_{iS} - P_{iAS})L_{eff}\right) \tag{3.13}$$

where P_{iS} and P_{iAS} are the two probe waves at the gain and loss frequencies at $z = L$ position, g_B is the Brillouin gain and A_{eff} and L_{eff} are the effective area and length respectively.

By reversing equation 3.13, the following equation can be obtained:

$$P_{iS} - P_{iAS} < -\ln(1-d)\frac{A_{eff}}{g_B L_{eff}} \overset{L\to 1}{=} -\ln(1-d)\frac{A_{eff}}{g_B}\alpha \tag{3.14}$$

where α is the fiber attenuation.

Equation 3.14 shows that the system does not depend on the CW probe power and also that it is robust to depletion when two probe wave sidebands with equal amplitude are present in the fiber at the same time ($P_{iS} - P_{iAS} = 0$). Also, it can be concluded that for low attenuations the effect of depletion will be increased (short fibers) and for long fibers the interaction among the pump and probe waves will be affected by the attenuation, thus reducing the effect of pump depletion. It is important to note that one of the probe sidebands should be filtered before detection as the interaction among the pump wave and both probe sidebands is equal but in opposite amplitude.

The use of a two sideband probe wave has no real limit in terms of depletion, except the SBS threshold of the two sidebands set on several milliwatts. In case both sidebands are not totally symmetric, a maximum power difference of 40 μW can be considered under standard conditions based on the limit provided by equation 3.14 [62].

3.3.3 Acceptable Power Levels

After the study of the MI and depletion phenomena, it can be concluded the acceptable power levels for long range BOTDA systems so no undesired effects arise. The most limiting effect when configuring the power level of the pump wave is MI. As seen in subsection 3.3.1, the limit for the appearance of MI is set below 26 dBm (400 mW), where the pump signal contains 90 % of the total power. For long range BOTDA systems, > 75 km, the maximum power level is reduced so no MI manifests at all, lowering it until 20-23 dBm (100-200 mW) [47, 63]. This power limit might be lower if SPM is a concern, as we will show later.

For the case of the probe wave, as stated in the previous subsection (3.3.2), theoretically there is no limitation when two symmetric sidebands are employed in the interaction. Nevertheless, the power level of the probe wave is going to be limited by the SBS threshold. It is important to consider an unbalance on the two probe sidebands, which could imply a depletion effect. This arises especially in ultra-long range BOTDA systems, since the distance that the optical waves must travel is considerable. Long fiber lengths can produce an unbalance on the waves due to a cascaded SBS process, as it will be addressed in subsection 4.2.1. In such terms, it has been demonstrated that typically pump depletion effects can be neglected if the minimum power difference between the Brillouin pump and probe signal is approximately 10 dB or less than 10 % [42, 49, 62].

3.3.4 Raman Amplification

One of the most employed techniques in BOTDA technology to enhance the sensing range is distributed Raman amplification. This technique, based on Stimulated Raman Scattering (SRS - section 2.7), induces distributed gain along the fiber compensating mainly attenuation (α) and therefore maintaining the pump and/or probe levels high enough to ensure sufficient gain. Spontaneous Brillouin scattering sensors have been using Raman assistance since the beginning of 2000 [64–67], although for standard BOTDA it was employed for the first time by Rodriguez-Barrios *et al.* [39] in terms of First-order Raman amplification and by Martin-Lopez *et al.* [45] through Second-order Raman amplification.

3.3.4.1 First-Order Raman Amplification

Distributed Raman amplification is able to generate amplification of the signals within the fiber as it uses the whole fiber span as an amplifier. This is developed since the energy coming from one or several high-power CW pumps is transfered to a signal propagating at longer wavelengths. The characteristic gain curve seen in section 2.7, Figure 2.12, implies that a Raman pump emitting at 1455 nm ($\sim$ 206 THz) will provide amplification at 1550 nm ($\sim$ 193 THz; 13 THz difference), window at which our developed BOTDAs work.

On the Raman amplification scheme, that can be observed in Figure 3.11, it is possible to develop three different configurations based on how the Raman pump is introduced within the fiber:

- Co-Propagating Amplification (X on - Y off on Figure 3.11): When the Raman pump propagates in the same direction as the pulsed signal.

- Counter-Propagating Amplification (X off - Y on): In this case, the Raman pump is introduced in opposite direction to the pulsed wave.

- Bi-Directional Amplification (X on - Y on): The pump is introduced on both sides of the fiber.

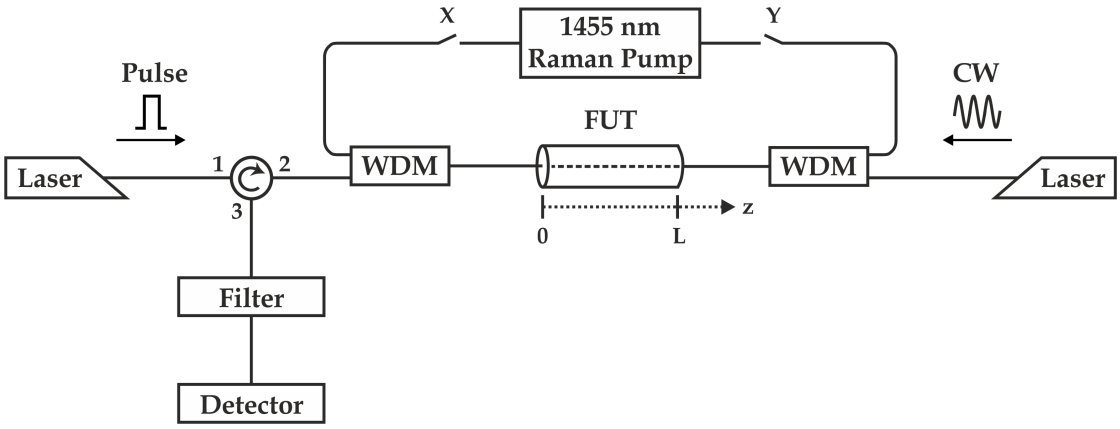

Figure 3.11: *Schematic of the First-order Raman-assisted BOTDA [39]. WDM: Wavelength Division Multiplexing; FUT: Fiber Under Test; CW: Continuous Wave.*

The evolution of the powers of all the signals present on the system ($P_P^{\pm}$: forward [+] and backward [-] Raman pump; $P_B^{\pm}$: Brillouin pump [+] and probe [-]) can be obtained if the Amplified Spontaneous Emission (ASE) and the Rayleigh backscattering are neglected, and if the Brillouin pump and probe wave powers are considered small with respect to the Raman pump wave powers, so that Raman pump depletion is omitted, the obtained equations are [39]:

$$\frac{dP_P^+(z)}{dz} = -\alpha_P P_P^+(z) \tag{3.15}$$

$$\frac{dP_P^-(z)}{dz} = +\alpha_P P_P^-(z) \tag{3.16}$$

$$\frac{dP_B^+}{dz} = -\alpha_B P_B^+(z) + g_R P_B^+(z)[P_P^+(z) + P_P^-(z)] \tag{3.17}$$

$$\frac{dP_B^-}{dz} = \alpha_B P_B^-(z) - g_B P_B^+(z) P_B^-(z) - g_R P_B^-(z)[P_P^+(z) + P_P^-(z)] \tag{3.18}$$

where α_P is the fiber optic attenuation at the wavelength of the Raman pump (1455 nm) and α_B is the attenuation at 1550 nm. g_R and g_B are the Raman and Brillouin gain coefficients respectively. Again, Brillouin pump depletion has been neglected.

The analytical solution of the probe wave is expressed as [39]:

$$\begin{aligned} P_B^-(z) = P_B^-(L)\exp\Bigg[& \frac{P_R^-(L)g_R}{\alpha_R} - \alpha_B L + \alpha_B z - \frac{P_R^+(0)g_R}{\alpha_R}\exp(-\alpha_R L) + \\ & + \frac{P_R^+(0)g_R}{\alpha_R}\exp(-\alpha_R z) - \frac{P_R^-(L)g_R}{\alpha_R}\exp(-\alpha_R(z-L)) - \\ & - P_B^+(0)g_B \exp\left(\frac{P_R^+(0)g_R}{\alpha_R} - \frac{P_R^-(L)g_R}{\alpha_R}\exp(-\alpha_R L)\right)\cdot \\ \cdot \int_L^z & \exp\left(\frac{P_R^-(L)g_R}{\alpha_R}\exp(\alpha_R(z-L)) - \frac{P_R^+(0)g_R}{\alpha_R}\exp(-\alpha_R z) - \alpha_B z\right)\Bigg] \end{aligned} \tag{3.19}$$

where it can be concluded that the probe wave has no solution, so it has to be integrated numerically or making extra assumptions on the non-analytic term. The resultant model was compared to the experimental results obtained with 75 km and 2 meter resolution, as shown in the set of Figures 3.12.

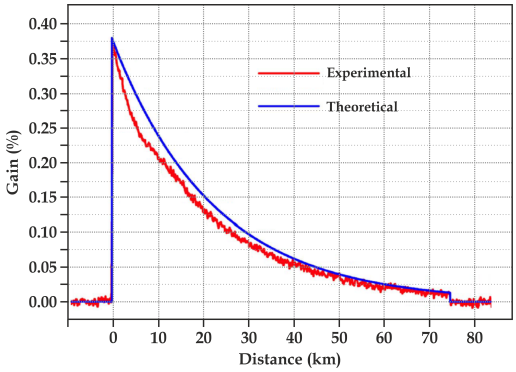

(a) No Raman Assistance.
Pulse Peak Power = 6.7 dBm (4.7 mW)
CW Power = -22.8 dBm (5.2 μW)
Raman Pump = - dBm (0 mW)

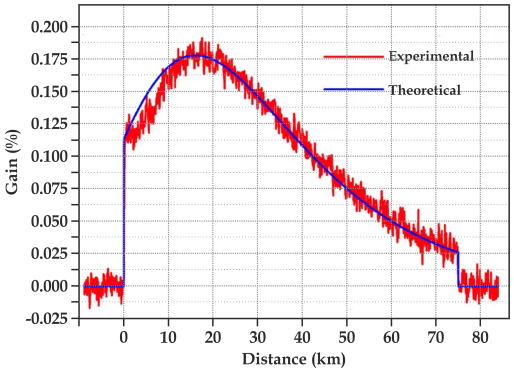

(b) Co-Propagating Raman Assistance.
Pulse Peak Power = 2.8 dBm (1.9 mW)
CW Power = -27.7 dBm (1.7 μW)
Raman Power = 25.5 dBm (355 mW)

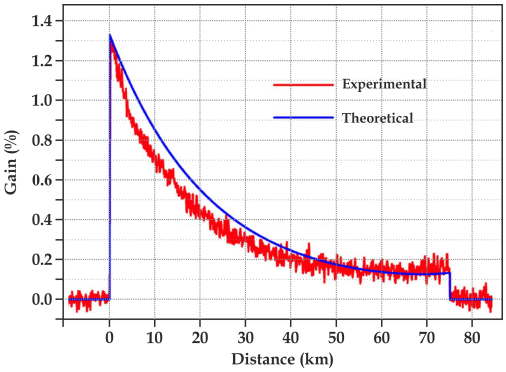

(c) Counter-Propagating Raman Assistance.
Pulse Peak Power = 12.7 dBm (18.8 mW)
CW Power = -36 dBm (0.25 μW)
Raman Power = 24.8 dBm (302 mW)

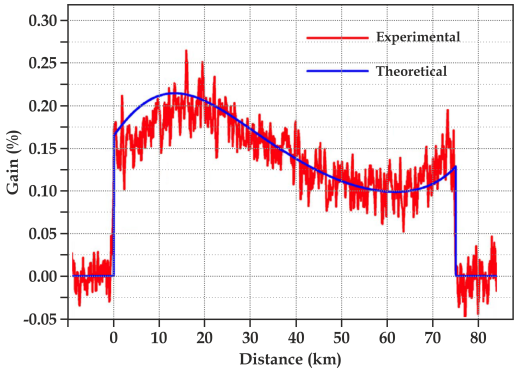

(d) Bi-Directional Raman Assistance.
Pulse Peak Power = 5 dBm (3.2 mW)
CW Power = -24 dBm (0.4 μW)
Total Raman Power = 27.8 dBm (610 mW)

Figure 3.12: *Experimental and theoretical BOTDA gain responses for different First-order Raman configurations: No Raman (a); Co-Propagating (b); Counter-Propagating (c); Bi-Directional (d) [39].*

All the results were obtained for SMF and always employing power levels that ensure absence of any pump depletion phenomenon or undesired non-linear effects. In the non-assisted configuration (Figure 3.12(a)), the effect of fiber attenuation decreases the acquired gain exponentially. Thus, at the far end of the fiber, the contrast is so small that a large uncertainty in the Brillouin shift determination will occur. This issue, as expected, can be solved through Raman amplification through the following three possible configurations. In the case of the co-propagating Raman amplification (Figure 3.12(b)), the average gain level is decreased although the maximum value is achieved at the 15-20 km. This reduces the impact of attenuation at the end of the fiber and therefore provides a better SNR. In the third configuration, counter-propagating Raman assistance (Figure 3.12(c)), the maximum gain remains at the beginning of the fiber, although the overall gain level is considerably increased (it is almost triples the gain levels of the non-assisted Raman configuration) since the amplification is provided to the CW probe. This scheme

should be carefully considered since could lead to large pump depletion. Lastly, the bi-directional amplification configuration Figure 3.12(d) obtains a fairly acceptable and flat gain level. These last features could be considered the most suitable ones for sensing purposes as the indetermination of the measurement will be similar at every fiber position. In all three amplified setups, the increase of the noise level is important and should be carefully treated. It arises from the RIN figure of the RFL ($\sim$ -110 dBc/MHz), and will be properly addressed in the forthcoming subsection 3.3.5.

3.3.4.2 Second-Order Raman Amplification

Through bi-directional First-order Raman amplification (subsection 3.3.4.1) we have seen that it is almost possible to yield a quasi-transparent propagation of the amplified signal in a BOTDA system along 75 km. Such response is really beneficial if employed for sensing purposes since, as mentioned in the previous section, the indetermination of the detected inhomogeneity will be similar in all fiber regions. This leads to the idea that higher order Raman amplification schemes could provide a fully transparent response all along the fiber length, thus fully reducing the indetermination of the measurement.

The use of higher Raman amplification schemes had already been proposed by Ania-Castañon [68] in order to achieve virtual transparency in optical fibers for telecommunication applications. This is possible because the gain can be distributed uniformly all along the fiber which leads to an ideally lossless transmission if the gain is set to match the losses, as can be observed in the theoretical results shown in Figure 3.13 for 100 km [68]. The simulations are based in a scheme that uses two equal pumps around 1365 nm which generate a stable pump at 1455 nm through a cavity created among two gratings located at 1455 nm. The new wavelength at 1455 nm has a nearly constant combined forward and backward propagating power which will provide an almost constant gain at 1550 nm [68]. This configuration has already been tested experimentally in BOTDA systems by Martin-Lopez *et al.* [45] developing a Second-order Raman amplification configuration over 50 and 100 km.

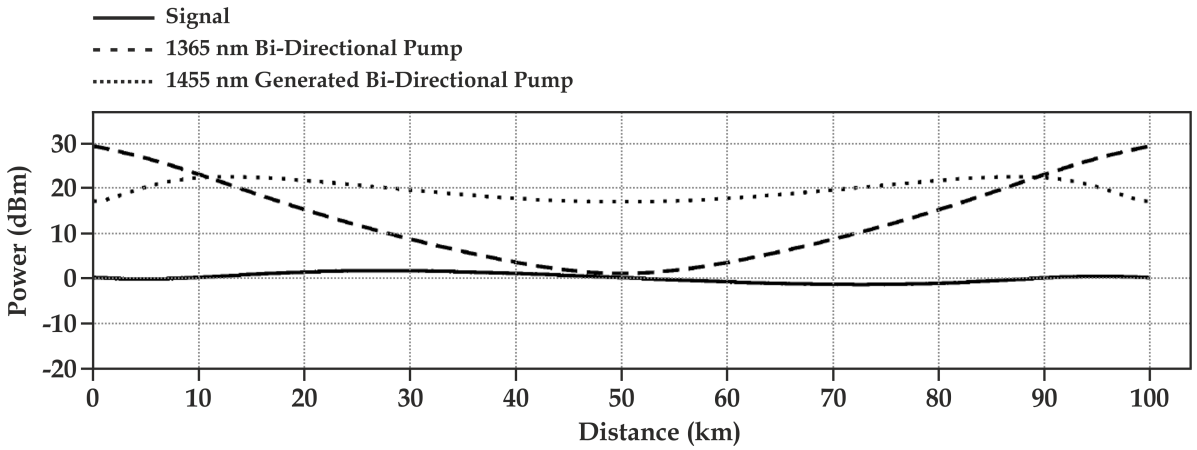

Figure 3.13: *Signal, First- and Second-order Raman pump power evolution in a 100 km cell length [68].*

The Second-order Raman amplification scheme is shown in Figure 3.14. In the cited setup, the Raman pump has an emitting wavelength of 1365 nm ($\sim$ 219 THz) which is introduced on both sides of the BOTDA fiber ends. The FBGs located at the entrance of the fiber are configured so that the central wavelength is located at 1455 nm, hence a stable secondary pump will be generated at 1455 nm ($\sim$ 206 THz; 13 THz difference) in the cavity through Raman lasing. This new wavelength presents a nearly constant power distribution all along the fiber, which at the same time will induce a fairly stable distributed Raman amplification at 1550 nm ($\sim$ 193 THz; 13 THz difference).

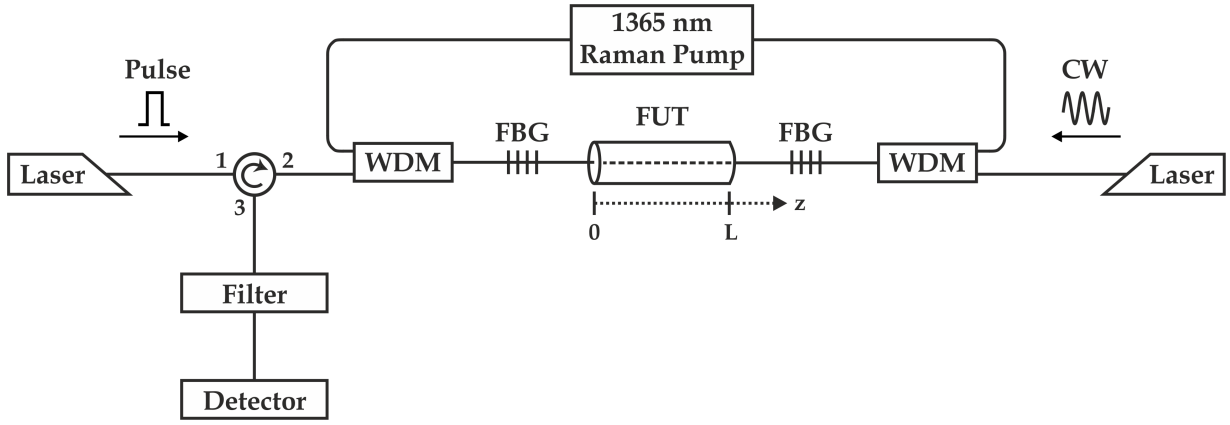

Figure 3.14: *Schematic of the Second-order Raman-assisted BOTDA [45]. WDM: Wavelength Division Multiplexer; FBG: Fiber Bragg Grating; FUT: Fiber Under Test; CW: Continuous Wave.*

The behavior of the system can be mathematically described, in a similar way to the First-order Raman amplification system 3.3.4.1, where the analytical solutions are expressed through the following set of equations [45]:

$$\begin{aligned}\frac{dP^{\pm}_{R_1}(z)}{dz} &= \mp\alpha_1 P^{\pm}_{R_1}(z) \mp g_{R_{12}}\frac{\nu_1}{\nu_2}P^{\pm}_{R_1}(z)\cdot \\ &\cdot\left(P^{+}_{R_2}(z)+P^{-}_{R_2}(z)+4h\nu_2\Delta\nu_2\left(1+\frac{1}{\exp(h(\nu_1-\nu_2)/k_BT_{abs})-1}\right)\right)\pm \\ &\pm r_1 P^{\mp}_{R_1}(z)\end{aligned} \tag{3.20}$$

$$\begin{aligned}\frac{dP^{\pm}_{R_2}(z)}{dz} &= \mp\alpha_2 P^{\pm}_{R_2}(z) \mp g_{R_{2B}}\frac{\nu_2}{\nu_S}P^{\pm}_{R_2}(z)(P^{+}_{B}(z)+P^{-}_{B}(z))\pm \\ &\pm g_{R_{12}}\left(P^{\pm}_{R_2}(z)+2h\nu_2\Delta\nu_2\left(1+\frac{1}{\exp(h(\nu_1-\nu_2)/k_BT_{abs})-1}\right)\right)\cdot \\ &\cdot(P^{+}_{R_1}(z)+P^{-}_{R_1}(z))\pm r_2 P^{\mp}_{R_2}(z)\end{aligned} \tag{3.21}$$

$$\frac{dP^{\pm}_{B}(z)}{dz} = \mp\alpha_B P^{\pm}_{B}(z) \pm g_{R_{2B}}\frac{\nu_2}{\nu_B}P^{-}_{B}(z)(P^{+}_{R_2}(z)+P^{-}_{R_2}(z)) - g_B P^{+}_{B}(z)P^{-}_{B}(z) \tag{3.22}$$

where + and − denote forward and backward propagation and also the pump and probe waves for P_B in a Brillouin Gain configuration. R_1 and R_2 identify the First- and Second-order Raman pumps, ν_i and $\Delta\nu_i$ the frequency and bandwidth for the Brillouin ($i = B$), First- ($i = 1$) and Second-order ($i = 2$) Raman pumps, α_i is the fiber attenuation at each wavelength, r_1 and r_2 are the double Rayleigh scattering coefficient of the fiber at each Raman frequency and g_{R_x} is the Raman gain coefficient at each Raman transition (when $x = 12$ it means First- Second-order transition and $x = 2B$ Second-order Brillouin transition). Finally, h is Planck's constant, K_B Boltzmann's constant and T_{abs} the absolute temperature. Quantum noise needs to be taken into account in this case as no signal is present in the fiber at 1455 nm in the initial conditions.

The evolution of the signals present on the proposed interaction is obtained by solving numerically equations 3.20, 3.21 and 3.22 with the corresponding boundary conditions. Also, some assumptions have been made based on the experimental conditions, such as 25 °C room temperature, typical gain and attenuation values for SMF, depolarized pumps and 0.5 nm reflection bandwidth FBGs [45].

In the results shown in Figure 3.15, it can clearly be seen the beneficial effect of the Second-order Raman configuration in BOTDA measurements. It compares the standard BOTDA gain trace (red line) for 50 km with a fully transparent theoretical and experimental Second-order Raman-assisted output (blue and green lines respectively). The dotted black trace corresponds to the theoretical response of First-order Raman amplification.

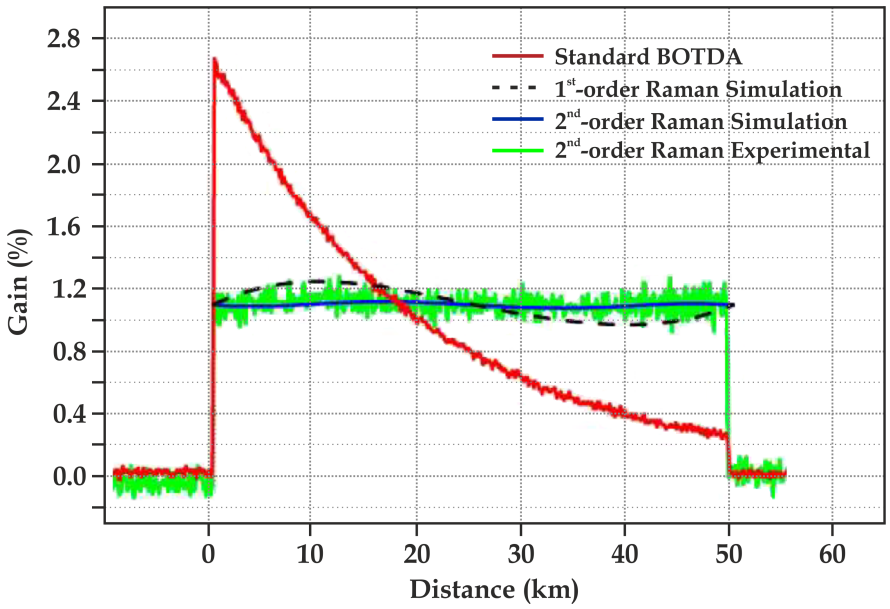

Figure 3.15: *Experimental and theoretical BOTDA gain responses for different fiber lengths in a Second-order Raman-assisted scheme [45]. Pulse Width=40 ns; Pulse Peak Power=8.7 dBm (7.5 mW); CW Power=-31.5 dBm (0.7 μW); Co- and Counter-propagating Raman Pump=23.7 dBm (235 mW).*

If a comparison is developed between the measured BFS for 75 km with First-order Raman amplification and 100 km with Second-order Raman amplification, it can be seen how the RIN transfer in the Second-order scheme is higher although it keeps constant (±3 MHz) all over the sensing distance, which considerably reduces the uncertainty of the measurement. Therefore, on both First- and Second-order assistance schemes RIN transfer has been identified as a major limitation. This issue will be addressed in more detail in the forthcoming subsection 3.3.5.

3.3.5 RIN Transfer

Several works have identified RIN transfer [69] as a major limitation in Raman amplified fiber telecommunication systems [70–72]. Obviously, this phenomenon has also a deleterious effect in Raman-assisted BOTDA systems, especially when increasing the monitoring distance. Therefore, in this section, we will analyze more deeply the effect of RIN transfer on the performance of long range BOTDA sensors, regarding First- and Second-order Raman pumping schemes.

The main issue of the RIN noise on BOTDA systems relies on the fact that the fluctuations of the pumping elements, either First- or Second-order, lead to time-dependent variations on the gain of the signal and are imprinted on the BOTDA probe [73]. The RIN is defined as the ratio of the time-averaged mean square value of the power fluctuations to the squared average power of the particular spectral component [70, 73–75]. The spectral distribution (in the electrical domain) of the pump-to-signal RIN transfer, monitored through the RIN transfer function is defined as:

$$H(\omega) = \left| \frac{RIN^{Out}_{Signal}(\omega)}{RIN^{In}_{Pump}(\omega)} \right| \tag{3.23}$$

where the corresponding RIN spectra are calculated from the ratio of the squared spectral density of the amplitude noise to the squared average power of each component [73].

Based on the RIN transfer model developed in [70], it is possible to extrapolate the behavior to our BOTDA schemes in order to quantify the RIN transfer as a function of the pump power for different pumping schemes as a function of the the signal frequency within the detection bandwidth ($\sim$ 100 MHz). Figure 3.16 shows a simulation of the RIN transfer of a First-order Raman amplification scheme at 1455 nm for 100 km standard SMF. In Figure 3.16(a) it is represented the behavior of the noise transfer for the possible three different configurations, bi-directional, co- and counter-propagating, when the pump sources are configured with 21.7 dBm (150 mW). Figure 3.16(b) simulates how the bi-directional configuration, the most employed scheme in our experimental developments, behaves at different pumping powers [42].

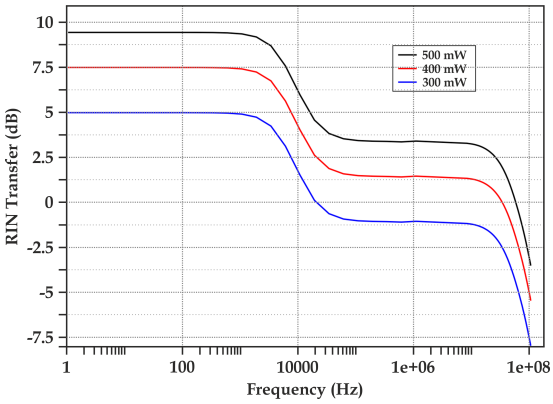

(a) First-order RIN transfer representation over 100 km as a function of the Raman pump power.

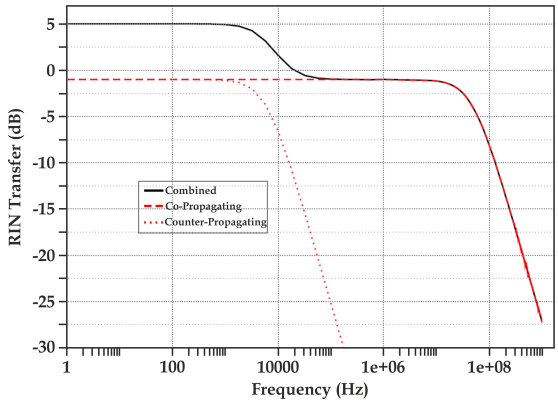

(b) Co- and Counter-propagating First-order RIN transfer for 21.76 dBm (150 mW) and its equivalent combination 24.77 dBm (300 mW).

Figure 3.16: *Theoretical representation of the First-order RIN transfer on BOTDA systems [42].*

As expected, the logarithmic RIN transfer increases very rapidly with power. In the bi-directional configuration, the RIN transfer curve shows a low-pass shape with two characteristic cutoff frequencies, one in the kHz range and the other in the tens of MHz range. As shown in Figure 3.16(b), the shape of the RIN transfer curve can be seen as the vector sum of the co- and counter-propagating cases, where the counter-propagating one, always with respect to the probe wave, shows a much lower cutoff frequency. This agrees well with the intuitive picture of co-propagating amplification, in which the pump and the signal travel with similar group velocities, favoring RIN transfer over a wider frequency range. The main limitation in terms of noise in this configuration is thus imposed by the pump power co-propagating with the probe.

Dealing with the Second-order Raman amplification scheme, based on the work developed by Alcon-Camas et al. [73], it is possible to develop the configuration already presented in subsection 3.3.4.2, where there are unique Raman sources at 1365 nm that generate a 1455 nm pump through FBG located at that very wavelength, but also to introduce at the same time trough WDMs two different pumps at 1365 nm and at 1455 nm. That configuration is very similar to the one that will be described in section 4.4. Figure 3.17 shows how the noise transfer behaves for the cited two configurations for pumping conditions similar to the ones represented in Figure 3.16(a) [73]. Figure 3.17(a) represents the amount of RIN transfer at different frequencies for 50 km fiber span and Figure 3.17(b) for different fiber lengths until 100 km.

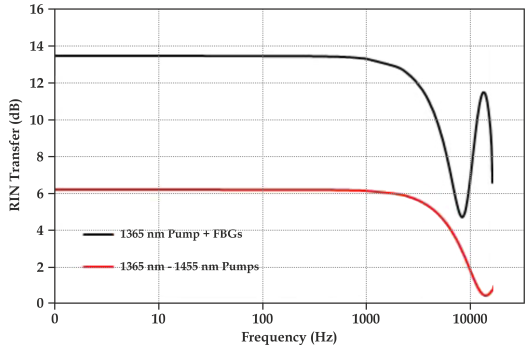

(a) Second-order RIN transfer representation over 50 km for two different pumping schemes: a unique 1365 nm pump and a combination among a 1365 nm and a 1455 nm pump.

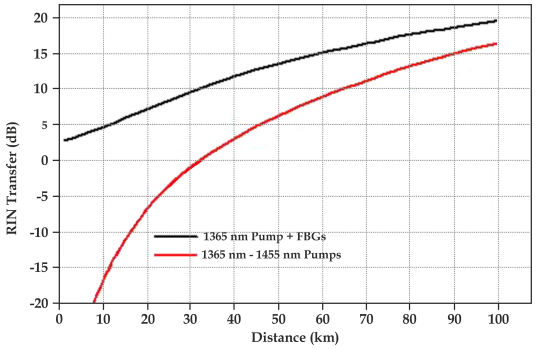

(b) Second-order RIN transfer as a function of distance for the same two configurations cited in sub-figure (a).

Figure 3.17: *Theoretical representation of the Second-order RIN transfer on BOTDA systems [73].*

As it happened with the First-order RIN transfer, the curve from Figure 3.17(a) has a low-pass appearance with a unique cutoff frequency in the kHz range. As compared, the configuration with FBGs has a greater noise level compared to the one that uses both pumps at 1365 nm and 1455 nm. The unusual behavior of the oscillations in the cavity scheme can be attributed to a combination of the presence of peaks corresponding to the cavity round-trip and the fact that oscillations in the backward-propagating components are reinforced due to the boundary confitions set by the FBG reflectors, which feed them back into the cavity [73]. If we want to extrapolate the obtained simulations to our range expectations ($>$ 75 km) we can observe on Figure 3.17(b) that as long as the distance increases, the RIN transfer grows too.

In conclusion, considering a typical RIN value of First- and Second-order Raman lasers of -110 dBc/Hz, the expected Root Mean Square (RMS) noise in this case is foreseen to

be in the order of 10^{-3}, which is in the same order as the gain to be measured. As one increases the Raman pump power, the overall RIN increases too as a function of the pump power, as observed in Figures 3.16(b), as well as a function of the measuring distance, Figure 3.17(b). The growth of RIN transfer is thus faster than the achieved gain. Hence, the use of Raman amplification should be limited to the point of overcoming the detection issues. To avoid RIN issues it is possible to employ low-RIN pumps, e.g. semiconductor lasers, like the setup described in [49] by Soto *et al.* or pump just up to the point of making the signal visible within the range of the detection setup.

3.3.6 Pulse Coding

Together and correlative to the distributed Raman amplification technique (subsection 3.3.4), it has been widely studied the so called Pulse Coding technique to enhance the SNR on BOTDA systems and consequently its sensing range. The use of optical coding as a SNR enhancer is not recent since it has been developed since the middle 1970s from the work performed by Moharir *et al.* [76]. The breakthrough was achieved by Jones [77] when employing Simplex codes (S-codes) to enhance the sensitivity of OTDRs, since it considerably improved the signal dynamic range. The transition of this technique to different time domain sensing techniques has been widely developed and exploited by Soto in his thesis dissertation [14], and tried for the first time in a BOTDA sensor over 50 km with 1 meter resolution [40].

The S-codes have a linear nature (see Figure 3.18), which in principle could denote an impossibility to be applied in non-linear systems such as distributed Brillouin Gain sensors. Nevertheless, as we already know, the interaction length in BOTDA systems is very short (tens of ns) and consequently the gain achieved quite small. This characteristic makes the Brillouin gain to be considered linear. This assumption implies that the linear dependence of ΔI_{CW} (as expressed in equation 3.10) with the pump intensity ($I_p(z', \Delta\nu)$) can increase the SNR through the use of linear optical pulse coding [77–79], such as the S-codes, without varying the spatial resolution. When using any coding technique, the interaction length will now be the code length (L_c), which is translated to the S-code as the bit number. Therefore, the CW intensity will be expressed as [48]:

$$\Delta I_{CW}(t, \Delta\nu) \propto \sum_{i=1}^{L_c} \int_{v_g t/2 + i\Delta z}^{v_g t/2 + i\Delta z} g_B(z', \Delta\nu) I_{pi}(z', \Delta\nu) dz' \tag{3.24}$$

where i denotes the bit number position ($i \in [1, L_c]$). Based on equation 3.24 it can be concluded that the measured ΔI_{CW} will correspond to a linear combination of the fiber response to pump signal pulses composed through the S-code. Consequently, the S-coded BOTDA traces will be represented as [48]:

$$\begin{pmatrix} \eta_1(t) \\ \vdots \\ \eta_i(t) \\ \vdots \\ \eta_{Lc}(t) \end{pmatrix} = S \begin{pmatrix} \Psi_1(t) \\ \vdots \\ \Psi_i(t) \\ \vdots \\ \Psi_{Lc}(t) \end{pmatrix} + \begin{pmatrix} e_1(t) \\ \vdots \\ e_i(t) \\ \vdots \\ e_{Lc}(t) \end{pmatrix} \tag{3.25}$$

where S is the S-matrix [80], $\eta_i(t)$ is the ith coded-BOTDA trace, $\Psi_i(t)$ is the single-pulse BOTDA trace delayed and ith multiple of the bit with respect to $\Psi_1(t)$ and $e_i(t)$ is the amplitude of the uncorrelated zero-mean noise added to each coded-BOTDA trace. The decoding process is developed through the following relationship [48]:

$$\begin{pmatrix} \widehat{\Psi}_1(t) \\ \vdots \\ \widehat{\Psi}_i(t) \\ \vdots \\ \widehat{\Psi}_{Lc}(t) \end{pmatrix} = S^{-1} \begin{pmatrix} \eta_1(t) \\ \vdots \\ \eta_i(t) \\ \vdots \\ \eta_{Lc}(t) \end{pmatrix} \tag{3.26}$$

where $\widehat{\Psi}_i(t)$ is the estimated single-pulse BOTDA trace $\Psi_i(t)$. A graphical example of a S-code transform technique using a S-matrix of order 3 can be seen in the following picture:

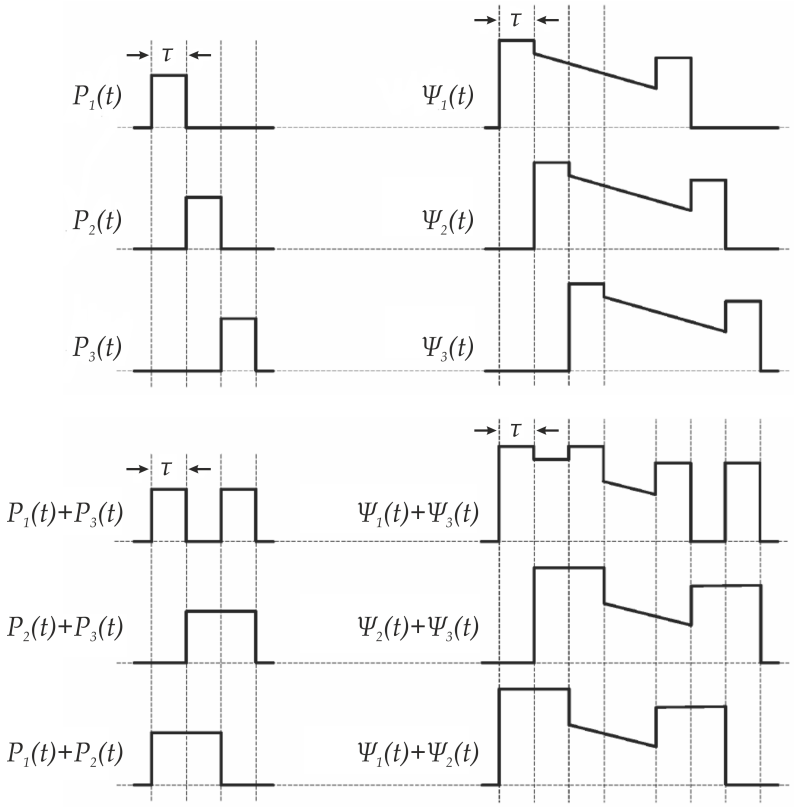

Figure 3.18: *Example of the S-code transform using a S-matrix of order 3 [80].*

The estimated single-pulse BOTDA traces are afterwards inversely time-shifted and averaged, and the obtained final decoded trace has an enhanced SNR compared to the same BOTDA trace obtained with a single-pulse. The coding gain (g_{cod}) is expressed as [48]:

$$g_{cod} = \frac{L_c + 1}{2\sqrt{L_c}} \tag{3.27}$$

With this SNR enhancement, there will be an improvement of the local frequency error (σ_ν), that comes determined by [81]:

$$\sigma_\nu = \frac{1}{SNR}\sqrt{\frac{3}{4}\delta\Delta\nu_B} \tag{3.28}$$

where δ represents the frequency sampling step. Actually, the expression is subject to the condition that $\delta << \Delta\nu_B$, which is equivalent to require a large number of frequency sampling points ($\delta \geq 3$) [81].

The SNR enhancement is notably represented in the results obtained by Soto *et al.* [40] and depicted in Figure 3.19. Employing a 511 bit S-code the signal to noise ratio is increased in more than 10 dB.

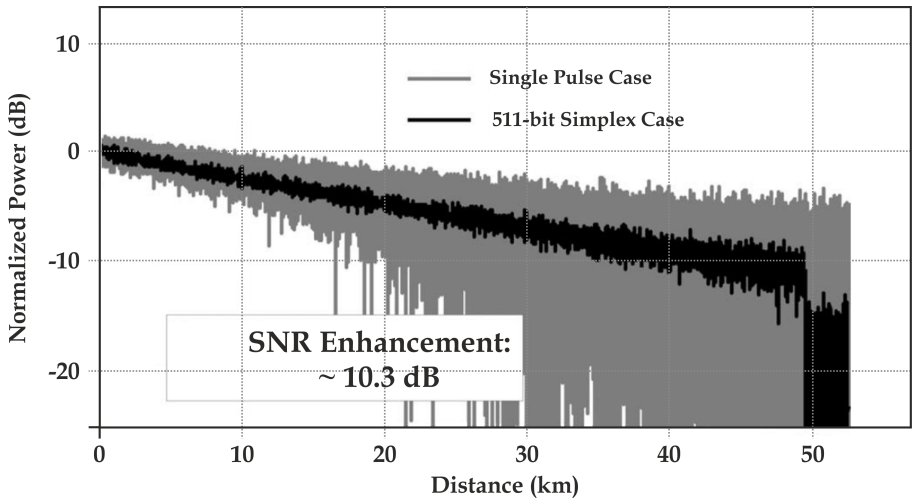

Figure 3.19: *Experimental comparison of the results obtained with a simple pump pulse BOTDA and a S-code system [40].*

3.4 Resolution Increase

If in terms of sensing range the logic path to follow can be focused on increasing the power levels of the signals present within the fiber, when talking about resolution, as we already know, it directly depends on the width of the employed pulses as shown in equation 3.1. Once again, this is not as trivial as it seems. The real resolution limit will be related to the phonon lifetime (subsection 3.2.2). Together with the pulse width, it is important to take into account the SPM induced on the Brillouin pump signal, which is going to be broadened as a function of the distance. These effects limit the resolution for long range systems to approximately 2 meters. To overcome such limitations it will be necessary to apply techniques to avoid such restrictions. In this thesis dissertation it was employed the DPP technique [82], since its features allow it to be employed in long range BOTDA systems. As done in the previous section (3.3), before explaining in detail the DPP technique, a study of the pulse width reduction and SPM effects will be provided.

3.4.1 Pulse Width Reduction

As cited several times, the resolution of a BOTDA comes determined through the width of pulses employed in the pump signal. It would be logic to think that the shorter the pulses, the higher the resolution will be, as far as the bandwidth of the receiver is wide enough.

Unfortunately, Brillouin sensors are limited in terms of resolution due to the acoustic phonon lifetime within the fiber (τ_p). This constant equals approximately 6 ns [16], and implies a limit to the spatioal resolution $\sim$ 1 meter. Obviously, to obtain sub-metrical resolutions it would be necessary to employ pulses below 10 ns, but in such circumstances the acoustic wave would not fully respond to the optical excitation of the pulses. In the frequency domain, the gain/loss experienced by the CW will broaden and lose efficiency as a consequence of the convolution between the BGS and the spectrum of the pulse itself [83], as can be seen in Figure 3.20.

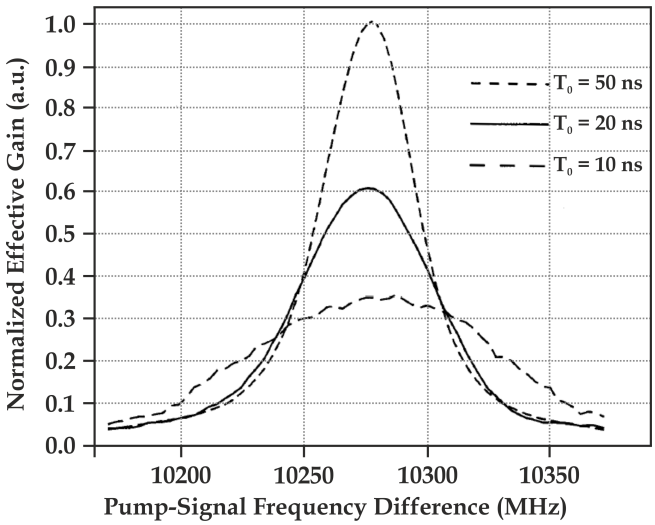

Figure 3.20: *Experimental results of the spectral pump pulse broadening effect when reducing its temporal width [83].*

Therefore, assuming a perfectly rectangular pulse with T_0 duration, this new convolution can be expressed as:

$$\overline{g_B}(\Delta\nu) = 2\exp(-\pi\Delta\nu_B T_0)[cos(\pi\Delta\nu_B T_0) - cos(2\pi\Delta\nu_B T_0)]g_B(\Delta\nu) \tag{3.29}$$

where $\Delta\nu_B$ is the BGS linewidth and $g_B(\Delta\nu)$ is the local BGS (2.86). Since the Lorentzian spectrum is replaced by the new $\overline{g_B}(\Delta\nu)$, when pulses shorter than 10 ns are employed their spectral width will be similar to the natural BGS [83], which leads to two main drawbacks on the BOTDA performance. Firstly, the Brillouin peak is reduced and consequently the CW gain contrast and the SNR of the BOTDA are decreased. Secondly, the spectral broadening of the measured BGS increases the uncertainty of the BFS determination which is translated as a larger uncertainty in the measurement.

3.4.2 SPM on BOTDA Systems

The precision of the measured variable in a BOTDA system (strain or temperature), can be linearly scaled with the spectral broadening of the effective gain, which is roughly obtained from the convolution among the pulse spectrum and the natural Brillouin gain spectrum. As already cited in subsection 2.4.1.1, SPM produces small phase chirps during intensity transitions in the pulses (leading and trailing edges) [84]. The frequency broadening associated to the phase modulation produces a reduction in the gain peak and uncertainties in the BFS determination. The SPM-induced spectral broadening of the pulses already had been reported in different works on coherent optical time-domain reflectometer systems [85, 86] but it was Foaleng-Mafang *et al.* who reported it for the first time in BOTDA systems [84].

SPM (phenomenon explained in subsection 2.4.1.1) is a consequence of the Kerr effect in fiber. Kerr effect produces an intensity dependent refractive index, causing the optical pulse to self-modulate its own optical phase as a function of its intensity profile. Since the pulse creates a time varying refractive index, this also produces a time dependent variation of the non-linear phase (ϕ_{NL}), which is translated as instantaneous frequency variations all along the pulse, which can be expressed as [84]:

$$\Delta\omega(t) = \frac{d\phi_{NL}(z,t)}{dt} = -n_2\frac{\omega}{c_0}z\frac{dI(t)}{dt} \tag{3.30}$$

Equation 3.30 shows that signals which constantly change their temporal transitions will suffer more from SPM. Therefore, theoretically, a rectangular pulse with constant intensity and instantaneous transitions, will show no pulse broadening ($\Delta\omega(t) = 0$). An interesting pulse in terms of spectral efficiency is the Gaussian shaped pulse. This contour varies constantly in intensity, but shows the best time-bandwidth product, thus the best time-frequency resolution [84]. A Gaussian envelope's intensity can be expressed as:

$$I(t) = \left|A\exp(-t^2/\tau^2)\right|^2 = I_0\exp(-2t^2/\tau^2) \tag{3.31}$$

with a $1/e$ width τ. Therefore the instantaneous frequency chirp imposed on the Gaussian pulse by SPM based on equation 3.30 shows the following expression [84]:

$$\Delta\omega(t) = 4n_2\frac{\omega}{c_0}zI_0\frac{t^2}{\tau^2}\exp(-2t^2/\tau^2) = 4\gamma zP\frac{t}{\tau^2}\exp(-2t^2/\tau^2) \tag{3.32}$$

where c_0 is the vacuum light velocity, ω is the central angular frequency of the optical pulse, I_0 and P are the peak intensity and the peak power respectively and γ is the non-linearity factor described in equation 2.45. As we already know, in a long fiber, the distance $z = L$ should be replaced by the effective length of the fiber L_{eff} (equation 2.47).

With all the previous statements, and considering $\tau_{max} = T_0/\sqrt{8\ln 2}$, it can be concluded that the maximum frequency variation of the instantaneous frequency is [84]:

$$\Delta\omega_{max} = 1.43\frac{\gamma PL_{eff}}{T_0} \tag{3.33}$$

For typical long range BOTDA systems ($\gamma = 1\text{W}^{-1}\text{km}^{-1}$, $P = 100$ mW, $L_{eff} = 20$ km and $T_0 = 10$ ns), the value of $\Delta\omega_{max}$ rounds $2\pi \cdot 29$ MHz, which is close to the Brillouin natural linewidth.

Based on the previous assumptions, the frequency spectrum of the Brillouin gain linewidth after experiencing SPM can be obtained through the Fourier transform of the convolution between the real pump source spectrum after SPM ($g_{SPM}(\Delta\tau)$) and the natural BGS. The suffered SPM by the pump pulse can be obtained by computing the pulse spectrum evolution along the fiber, considering the time origin always at the pulse center, and it is expressed as [84]:

$$g_{SPM}(\Delta\nu) = FT\left\{ \underbrace{A\exp(-t^2/\tau^2)}_{Gaussian\ amplitude\ term} \underbrace{\exp[i\gamma L_{eff} P\exp(-2t^2/\tau^2)]}_{SPM\ term} \right\} \tag{3.34}$$

As we have seen, the detrimental effect of SPM depends on the pulse shape and duration, but also depends on the power of the employed pulsed signal. Therefore, it is important to consider SPM as a drawback when enhancing the sensing range of a BOTDA system, although in this case it has been included within the Resolution Increase section due to its dependence not only with the power levels but with the shape and size of the employed pulses.

The next figures will show how SPM broadens the Brillouin gain spectrum in an experimental setup developed by Foaleng-Mafang *et al.* [84] for different pulse powers and widths along 25 km of SMF.

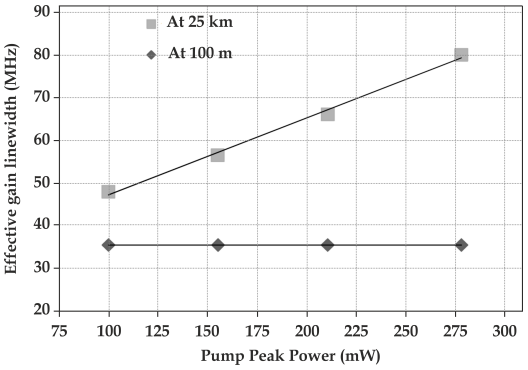

(a) Gaussian pulse peak power relationship on Brillouin gain broadening due to SPM.

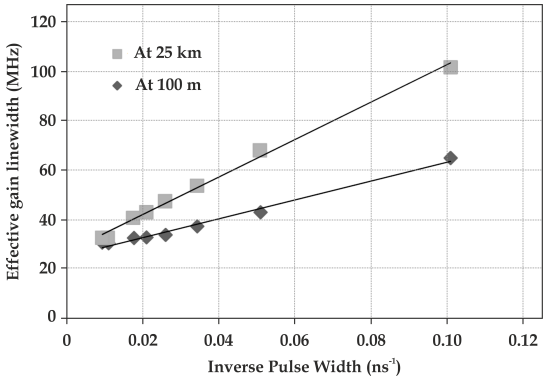

(b) Gaussian pulse width relationship on Brillouin gain broadening due to SPM.

Figure 3.21: *Experimental results of SPM on BGS width at the beginning and end of 25 km SMF as a function of the peak power and the inverse pulse width [84].*

As seen in Figures 3.21(a) and (b), when the employed pulse has a Gaussian shape, as expected, the BGS broadens as long as the fiber length increases. It also increases with higher peak power and smaller pulse width. Therefore, it can be concluded that SPM spoils the performance of long range and high resolution BOTDA systems. When trying to increase the resolution of the system it is important to have in mind the effect of SPM since below 20 ns (0.05 ns^{-1}) the effect starts to become more detrimental.

Based on the theory, the use of rectangular pulses should avoid all the cited effects. As seen in Figure 3.22 it has been experimentally demonstrated by Foaleng-Mafang *et al.* such statement. Unfortunately, in some occasions it is impossible to retrieve completely rectangular pulses, that is why SPM needs always to be taken into account when dealing with high resolution BOTDA systems.

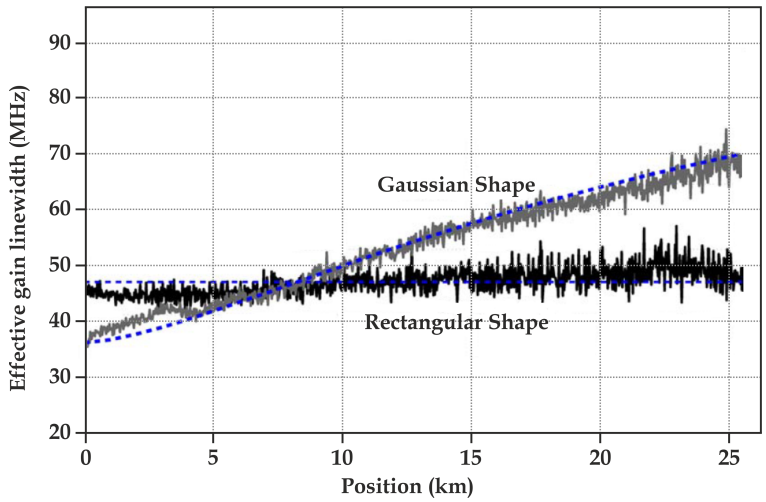

Figure 3.22: *Experimental and theoretical representation of the comparison of SPM for rectangular and Gaussian pulses [84].*

3.4.3 Differential Pulse-width Pair Technique

As mentioned in subsection 3.2.3 the natural resolution limit of a BOTDA lays on two times the phonon lifetime ($\tau_p \sim 6$ ns). Several applications require the monitorization of long range structures with resolutions below the meter (e.g. crack control in large structures), which involves the necessity of developing resolution increase techniques [87].

In the last years several techniques have been developed, such as the dark pulse technique [88], the dynamic grating technique [89], the differential pre-excitation technique [90], the Brillouin echoes [16, 91–93] and the DPP technique [82, 94, 95]. They are all based on the pre-excitation of the acoustic wave in order to avoid the phonon lifetime limitation. From the previous techniques the most proper in terms of application to long range systems is the DPP technique since it is based on the subtraction of gain traces obtained with slightly different pulse widths, which will have a duration much longer than the phonon lifetime (typically 4-6 times larger). Due to this procedure, the impairments due to SPM are also avoided.

The general solution of the acoustic wave ($A_a(z,t)$) can be expressed as [82]:

$$A_a(z,t) = \frac{1}{2}\Gamma_{B1} g_B \exp(-\Gamma_B t) \int_0^t E_p(z,t') E_S^*(z,t') \exp(\Gamma_B t') dt' \tag{3.35}$$

where E_p and E_S are the amplitudes for pump and Stokes wave respectively, Γ_B is the damping coefficient of the acoustic wave and Γ_{B1} is the damping time of the phonon field ($\Gamma_{B1} = 1/2\tau_p$).

Based on the expression obtained in equation 3.35, it can be concluded that when two Brillouin gain curves are obtained through two different pulse-width signals (τ and $\tau+\delta\tau$), the common term will be removed and the inhomogeneous section will manifest [82]. The schematic representation of such dynamic is shown in Figure 3.23, where $I(0,t,\tau)$ and $I(0,t,\tau+\delta\tau)$ indicates the temporal Brillouin gain at $z=0$ obtained with differential pulse widths (τ and $\delta\tau$), and $I(0,\delta\tau)$ designates the difference between them. As stated previously, the subtraction among the Brillouin gain signals will show a section equivalent to the pulse width difference ($\delta z = c\delta\tau/2$) [82].

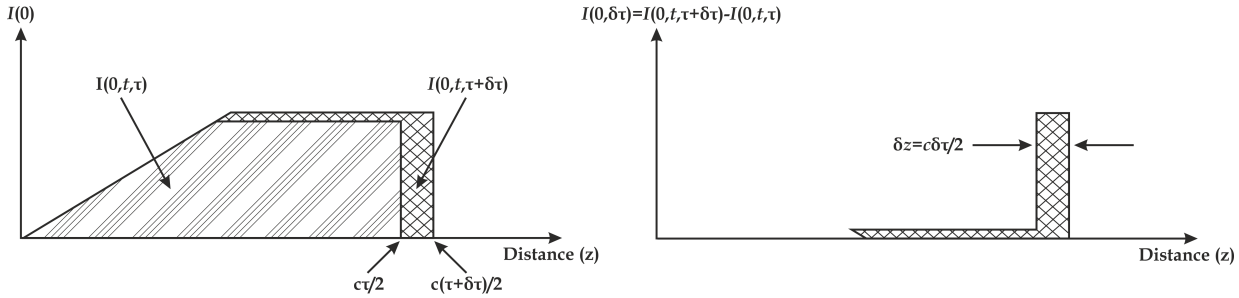

Figure 3.23: *Working principle of the DPP technique in BOTDA systems to obtain high resolution measurements [82]. It is appreciable how the resulting resolution is determined by the difference among the obtained gain curves with different pulse widths.*

3.5 Summary

All along this chapter it has been reported the essentials of the BOTDA technique as well as its limitations when improving its performance in terms of range and resolution.

Since range increase is directly linked to a raise of the power levels of the signals interacting within the fiber, it is important to control their amplitude so MI and/or depletion do not arise. The limit for the pump wave will be set by MI to 20-23 dBm (100-200 mW) [47,63] and the probe wave will be restricted in terms of spontaneous Brillouin scattering as well as depletion, considering acceptable a minimum power difference between the pump and probe waves of approximately 10 dB or less than 10 % [42, 49, 62]. The proposed and described techniques to overcome such issues are Fisrt- and Second-order Raman amplification and pulse coding.

Resolution will be fully defined by the width of the employed pump pulses. The natural resolution restriction for standard BOTDA systems is set by the phonon lifetime, 10 ns (see section 3.4), which equals to a determination of 1 meter. In long range BOTDA systems, the width of the pulses will also be limited by SPM, which in return increases the maximum acceptable width to approximately 20 ns or 2 meters or requires very square-shaped pulses. To be able to increase the resolution of long or ultra-long BOTDA schemes a pre-excitation of the acoustic wave is necessary. The DPP technique has been described as a simple method to achieve this purpose.

Chapter 4

Optimization of Long Range Raman-Assisted BOTDA Systems

4.1 Introduction

In section 3.3, it has been detailed the obstacles that a standard Brillouin Optical Time Domain Analysis (BOTDA) faces when increasing its sensing range. As cited, the main issue is based when increasing the power levels of the signals interacting within the fiber since non desired phenomena such as Modulation Instability (MI) (subsection 3.3.1) and/or depletion (subsection 3.3.2) arise. Therefore, it is necessary to employ assistance techniques so that longer distances are achievable; Raman amplification (subsection 3.3.4) and/or pulse coding (subsection 3.3.6) in this case. In this chapter we will detail the experimental works developed all along this thesis dissertation based on range increase techniques, where both First- and Second-order Raman amplification techniques where employed as well as pulse coding.

When developing BOTDA systems, it is important to take into account some aspects that arise within the experimental setup that provide the gate to obtain optimum results. The first one, is the proper determination of the power levels of all the signals within the fiber. It is evident that when targeting extremely long distances the power levels of the signals interacting should be increased, although a non-controlled raise could provoke the appearance of undesired effects, such as MI or pump depletion, that spoil the proper performance of the system. Together with the power levels, it is important to control the Extinction Ratio (ER) of the employed pump pulses since if pump power is leaked when the pulse is supposed to be switched-off, even if the escape is small it will distort the retrieved signal due to the long fiber length employed. Lastly, it is determinant to control the Relative Intensity Noise (RIN) transfer from the employed Raman pumps to the detected signals. This issue will be addressed in the next chapter 5, since it has been identified as a major limitation in long range Raman-assisted BOTDA systems.

4.2 Analysis of Requirements

In order to provide better understanding of the processes happening in the proposed systems, First- and Second-order Raman amplifications, it will be necessary to develop numerical simulations of the procedure. For that intention, it is necessary to consider all the signals present in the interaction; two symmetrical probe wave sidebands (which ensure robustness to to pump depletion as explained in subsection 3.3.2), a pump wave together with a certain amount of leakage (which also involves power transfer among the probe wave sidebands and consequently the real pump depletion) and the set of Raman pumps (co- and counter-propagating) for each First- or Second-order pumps. Therefore, the whole system could be defined through steady-state equations, considering absence of Rayleigh scattering, spontaneous Raman scattering and pump depletion. The consequent set of equations has already been addressed in subsections 3.3.4.1 and 3.3.4.2 for First- and Second-order Raman systems respectively.

In case a unique probe wave sideband is considered, it could be plausible to develop a semi-analytical evaluation of the systems, which provides a first-hand estimation of the adequate power levels needed. Also, it is possible to apply the same supposition to the necessary ER of the pump pulses, since the developed treatment is for signal-to-background, which is comparable to a probe wave sideband unbalance in case two sidebands are present.

4.2.1 Power Levels

In the proposed systems, Self-Phase Modulation (SPM) will probably set the limit of the employed power levels of the pump pulses before MI becomes dominant. This arises since our pulse shaping methods provide far from squared pulses. As stated in subsection 3.4.2, SPM leads to small phase chirps during intensity transitions in the pump pulse that eventually become important in long fiber systems. The frequency broadening associated with this phase modulation leads to a reduced peak gain and uncertainties in the determination of the Brillouin shift, but leaves the temporal intensity distribution of the pump pulse unchanged, hence the spatial resolution is preserved.

Considering a Gaussian pulse, the peak excursion of the instantaneous frequency will be given by equation 3.33 ($\Delta\omega_{max} = 1.43\gamma P L_{eff}/T_0$). For a perfectly transparent setup, the effective length should be replaced by the physical length of the fiber. A good contrast can be preserved along the fiber by bounding the maximum broadening to 10 MHz, so in the perfectly transparent case, this limits the pump power to approximately 1.46 dBm (1.4 mW). In a non-assisted configuration, the power limit to avoid significant spectral broadening in the pump could remain at approximately 7.78 dBm (6 mW).

In terms of the probe wave, the most limiting phenomenon is depletion. Even though the analytical model developed in subsection 3.3.2 is not adapted to the Raman-assisted case, we can have an idea of the required parameters in our system by comparing the conventional case and the case of perfect transparency. The fraction of power lost by the pump through depletion can be directly calculated from the theoretical Brillouin loss induced by the probe, therefore, based on equation 3.11, depletion can be expressed as [42]:

$$d = 1 - \exp\left(-\frac{g_B}{A_{eff}} P_B^-(L) L_{eff}\right) \tag{4.1}$$

where g_B is the Brillouin gain coefficient and A_{eff} is the effective area of the fiber. The expression comes from the fact that the gain on the probe can be considered negligible in all cases. For a perfectly transparent setup, we can obtain a similar expression by simply replacing L_{eff} by L. We can now set the acceptable depletion to values below 10 % which has been proven to give acceptable frequency errors below 1 MHz [62]. For typical fiber characteristics ($g_B = 5 \cdot 10^{-11}$ m/W, $A_{eff} = 70$ μm^2) and $L = 100$ km, we can infer that the power levels should be in the order of 1 μW or below in the perfect transparency Raman-assisted configuration, while it is possible to reach up to 7 μW in the conventional non-assisted setup.

In long fiber configurations, high Continuous Wave (CW) probe power levels could produce a problem related to the CW interaction of the two probe sidebands and their respective spontaneous Brillouin scattering components. In particular, when the CW probe power increases beyond the threshold of amplified spontaneous Brillouin scattering, the energy transferred from the probe waves to their respective Stokes components could strongly unbalance the power among the two sidebands, as illustrated in Figure 4.1, where the energy transferred from the high frequency probe sideband to its Stokes component (at the pump wavelength) is expected to be transferred to the lower-frequency probe sideband, which in turn transfers energy to the lowest Stokes component. This also reinforced the fact that the ER has to be high in order to avoid this cascaded process.

In our sensing schemes, depletion will be produced on the probe sideband at higher frequency, while the lower-frequency sideband would not be significantly affected due to Brillouin gain/loss compensation. This cascaded energy transfer might quickly unbalance the power of the two probe waves, and thus compromise the robustness of the two-sideband probe technique against pump depletion within the useful sensing fiber section [62].

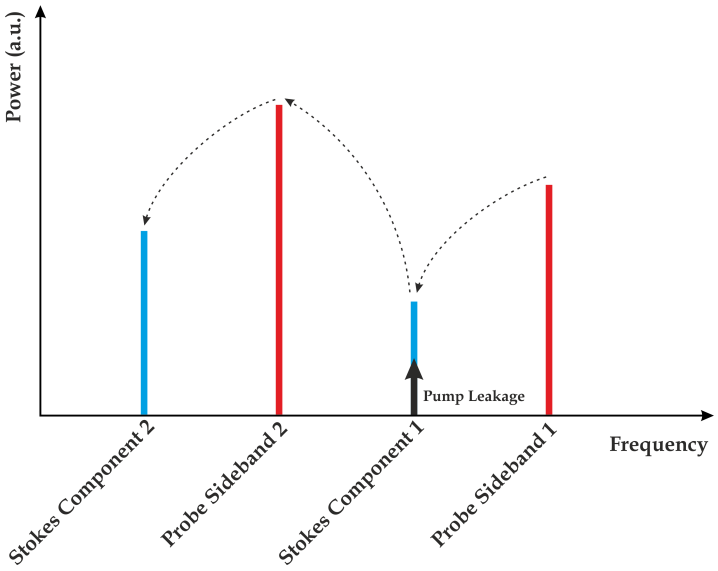

Figure 4.1: *Power imbalance resulting from the stimulated Brillouin scattering process occurring in a very long fiber when two high-power probe sidebands are employed. At the same frequency as the first Stokes component (initiated from spontaneous Brillouin scattering) the pump leakage is is present too [47].*

4.2.2 Extinction Ratio - ER

In conventional BOTDA setups, the Brillouin pump pulse is obtained by external modulation of a master laser using an Electro Optic Modulator (EOM) [32]. When the modulator receives the logical low part of the pulse on its input, also known as the "off" state of the EOM, a certain amount of pump power is released which comes characterized by the Extinction Ration (ER) of the modulator. Even though this leakage is small, it may have a very significant impact on the measurement when targeting long ranges (> 75 km) and high resolutions (≤ 2 meters). The employed pulse train has a temporal width of tens of ns, which determines a spatial resolution of meters (see subsection 3.4), and a repetition rate of hundreds of Hz or few kHz, which ensures that two pulses are not present at the same time within the fiber and therefore distorting the measurement. The cited pulse train structure is the reason why the liberated CW power by the modulator has to be many orders of magnitude smaller since the gain created by this CW background is distributed along the whole fiber length (≥ 100 km in this case) while the amplification created by the pump pulse remains limited to the resolution of the measurement.

In long and ultra-long range BOTDA systems the retrieved gain is considerably small, so the nonideality of the proposed case (CW leakage) can be treated as a superposition of the ideal case (short pulse with infinite ER) with a CW background generated by the continuous amplification of the probe by the CW background of the pump. Using the analysis performed in subsection 3.3.4.1 for the Raman amplification configuration [39] we can only quantify the Signal to Background Ratio (SBR) numerically. However,

the requirements in terms of ER can be easily understood by comparing a conventional setup and a perfectly transparent Raman amplification configuration, which consists in an arrangement with effectively zero loss (subsection 3.3.4.2 [45]).

For a conventional setup, the worst case of SBR is obtained in the far end of the fiber, where the pump is more attenuated, and is given by [42]:

$$\frac{\Delta P_B^-|_{pulse}}{\Delta P_B^-|_{leak}} = \frac{\Delta z \exp(-\alpha L)}{\kappa L_{eff}} \tag{4.2}$$

where ΔP_B^- is the detected change in probe wave power, α is the fiber attenuation, κ is the ER of the modulator, Δz is the pump pulse length, L is the fiber length and L_{eff} is the effective length, as defined in equation 2.47. In the aforementioned expression, we have assumed that the change on the Brillouin probe is small in all cases and that the fiber is perfectly homogeneous. Obviously, for the best results, this contrast should be made as high as possible, although a good trade-off can be obtained by setting this ratio to ≥ 1. For a conventional 20 km setup with 2 m resolution and $\alpha = 0.2$ dB/km, the previously stated expression implies ERs already in the order of 40 dB, which are still attainable with conventional EOMs.

As mentioned before, we cannot find analytically this ratio in a Raman-assisted configuration. However, for comparison, we can find a similar expression for a perfectly transparent fiber, regime very similar to the Second-order Raman amplification configuration demonstrated in subsection 3.3.4.2 [42]:

$$\frac{\Delta P_B^-|_{pulse}}{\Delta P_B^-|_{leak}} = \frac{\Delta z}{\kappa L} \tag{4.3}$$

An analysis of this expression shows that Raman assistance is less stringent in terms of ER requirements. For comparison, with the same criterion as before, a 100 km setup with 2 m resolution requires ERs of 47 dB in the case of perfect Raman amplification (complete transparency) and 60 dB in the conventional non-assisted case. These values are anyway not standard in EOMs, although possibly attainable in Acousto Optic Modulators (AOM) [96]. The improvement in this issue in the case of Raman assistance comes from the fact that the contrast is kept constant along the fiber, while it diminishes toward the fiber end in regular setups.

As we will see in the first developed experimental setup, it is possible to significantly enhance the SBR by introducing a Non-linear Optical Loop Mirror (NOLM) after the modulator to enhance the ER of the pulses [97]. As stated previously in subsection 3.3.4.2, this device works as a saturable absorber where the transmission grows with the power. In the working range, the output of this device scales with the cube of the input power [98], leading in theory to a tripling of the ER in dBs. In practice, however, the achieved ER is limited due to Rayleigh scattering and other non-ideallities to approximately 60 dB.

Another important aspect regarding ER lays on the fact that the wavelength of the pump pulses equals the wavelength of the 'Stokes 1" component present in Figure 4.1. Therefore, is a perfect ER is not achieved, in long range BOTDA systems the depletion issue addressed in the previous section will be reinforced degrading the performance of the setup.

4.3 First-Order Raman-Assisted BOTDA

In the work developed by Rodriguez-Barrios *et al.* in [39], a complete study of a First-order Raman-assisted BOTDA scheme was presented over 75 km of sensing distance with 2 meter resolution. In that very work the gate for extending the range until 100 km was kept open although, as expected, it would be necessary to overcome the addressed analysis of requirements first (section 4.2) so the target 100 km range is achieved.

4.3.1 Experimental Setup

The employed setup for this work is depicted in Figure 4.2, and it is similar to the one reported by Rodriguez-Barrios *et al.* in [39]; however, this one has a couple of key improvements in the pulse generation setup and the Raman pump tuning. In all the developed setups of this thesis dissertation, the pump and probe waves are generated with a controlled frequency difference from a unique source that is split and modulated [32] so any frequency disturbance on the master source does not affect the frequency difference between the pump and probe signals. In this particular case, the master source of our BOTDA is a 6 dBm (4 mW) Laser Diode (LD) ($\sim$ 1 MHz linewidth), which emits at 1553.59 nm.

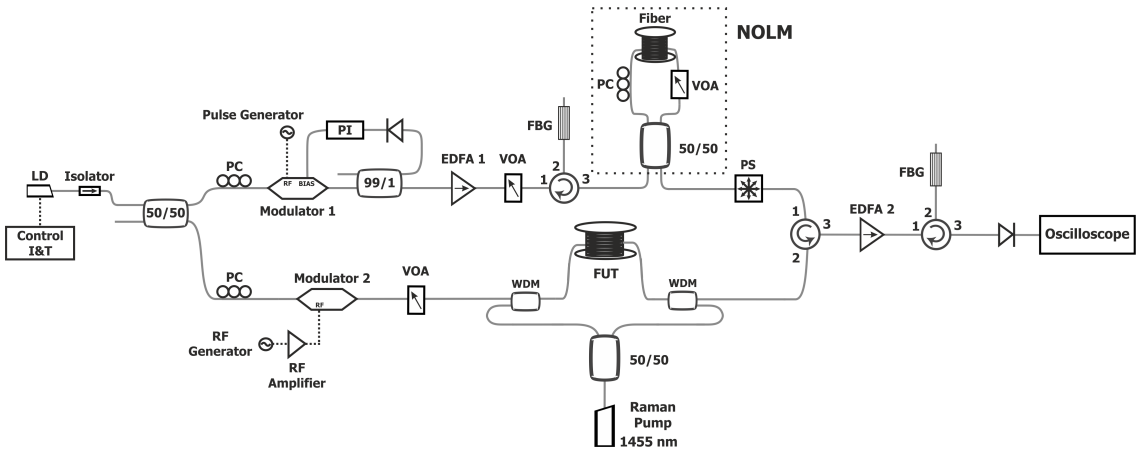

Figure 4.2: *Schematic representation of the experimental setup of the 100 km BOTDA system [42]. LD: Laser Diode; I&T: Current and Temperature; PC: Polarization Controller; PI: Proportional-Integrator; RF: Radio Frequency; EDFA: Erbium Doped Fiber Amplifier; VOA: Variable Optical Attenuator; FBG: Fiber Bragg Grating; WDM: Wavelength Division Multiplexer; FUT: Fiber Under Test; NOLM: Non-linear Optical Loop Mirror; PS: Polarization Scrambler.*

The pump wave is pulsed with 30 ns pulses, which are amplified by an Erbium Doped Fiber Amplifier (EDFA) which will produce an optically Amplified Spontaneous Emission (ASE) noise [99]. The broadband nature of this emission requires a filtering of the undesired frequencies, hence a Fiber Bragg Grating (FBG) is employed after the EDFA for such purpose. Since the measurement distance is 100 km, the repetition rate of the pulses has to be lower than 1 kHz, which means that a very low duty cycle is used, $\sim 10^{-5}$, thus ERs in the order of 10^5 are necessary to properly measure the variations on the probe wave (see subsection 4.2.2). For this matter, two systems are used to ensure this ER in the pump. Firstly, an electronic Proportional-Integrator (PI) circuit is employed in the modulator to set its working point to minimum transmission [100], which allows 25-30 dB of extinction. Since this is not good enough, a NOLM is employed [98], which together with

the PI provides the necessary ER in the pump pulses; > 50 dB. This device also produces a small compression of the pulses obtaining a pedestal-free narrow pulse [98, 101], which alters the original 30 ns width to 20 ns. In summary, the pump signal supplied to the fiber is composed by 20 ns pulses with a repetition rate of 700 Hz. The probe signal is obtained from the lower frequency sideband of the Amplitude Modulated (AM) master source, as the Brillouin Gain configuration is desired. The carrier frequency is suppressed by properly setting the Direct Current (DC) bias of the modulator, and the higher frequency sideband is filtered before detection employing for that purpose a narrowband FBG. Even though depletion issues are controlled based on the description given in subsection 3.3.2 by properly setting the pump and probe powers through Variable Optical Attenuators (VOA) located on each branch of the setup, our system has an extra advantage against that matter since both sidebands propagate within the Fiber Under Test (FUT), which compensates the depletion of the pump signal by the detected probe [62].

In order to achieve Stimulated Brillouin Scattering (SBS), both pump and probe signals are introduced in the sensing fiber in opposite directions together with the Raman pumps through suitable Wavelength Division Multiplexers (WDM). The Raman pumps are obtained by splitting the output of a Raman Fiber Laser (RFL), thus a bi-directional configuration is used for the Raman amplification process. As already mentioned in section 2.7, the maximum gain peak in Raman assistance manifests at 13 THz from the pump, which means that in order to produce amplification in the 1550 nm region, the RFL should emit at 1455 nm. As suggested in subsection 3.3.5, the Raman pump should be below 27 dBm (500 mW), therefore, in our experimental setup we configured the RFL at 26.8 dBm (480 mW), 23.8 dBm (240 mW) through each branch. Although this Raman pump power is below the value needed for a perfect end-to-end compensation of the losses, it guarantees the best trade-off between amplification and RIN transfer for our RFL in this fiber segment. As we already know, the Brillouin interaction has a large sensitivity to polarization [102], so it is necessary to employ a Polarization Scrambler (PS) in order to mitigate such effect, since it scrambles the polarization state of the entering signal into all possible states. The 100 km fiber is composed by four Single Mode Fiber (SMF) spools of 25 km each with an effective area of $70\mu m^2$ and a similar Brillouin Frequency Shift (BFS) located at approximately 10.67 GHz for the pump wavelength ($\sim$ 1554 nm). The peak power of pump and probe were 3.29 dBm (2.133 mW) and -37,7 dBm (0.17 μW), respectively, with 26.8 dBm (480 mW) of Raman pump which is equivalent to 23.8 dBm (240 mW) at each pump-probe branch, which ensures the avoidance of any undesired effect; MI, SPM or depletion.

4.3.2 Results

Figure 4.3(a) shows a comparison between the measured and the calculated gain at each point of the fiber at maximum gain, following the model developed in subsection 3.3.4.1, where the good agreement between both traces verifies the proper operation of the system. The pump power used is slightly below the value necessary for a good compensation of the losses. However, this ensures a good behavior of the setup in terms of RIN. As can be seen, the power levels used are in good agreement with the simple derivations provided in the previously developed analytical study. In Figure 4.3(b), the evolution of the retrieved BFS along the sensing distance is depicted where frequency shift is comprised between 10.6725 GHz and and 10.6825 GHz. The abrupt variation along the first kilometers is most probably due to some longitudinal variation in the construction parameters of the fiber,

probably the GeO_2 doping or an excess of strain when rolling the spool. The uncertainty of the measurement can be determined by analyzing the difference in the retrieved Brillouin shift for consecutive measurements. In this case the difference is smaller than 1.2 MHz, which is equivalent to a temperature uncertainty below 1.2 °C/24 $\mu\epsilon$ in case of strain measurements considering a 1 MHz/°C and 0.05 MHz/$\mu\epsilon$ sensitivity respectively for the target fiber.

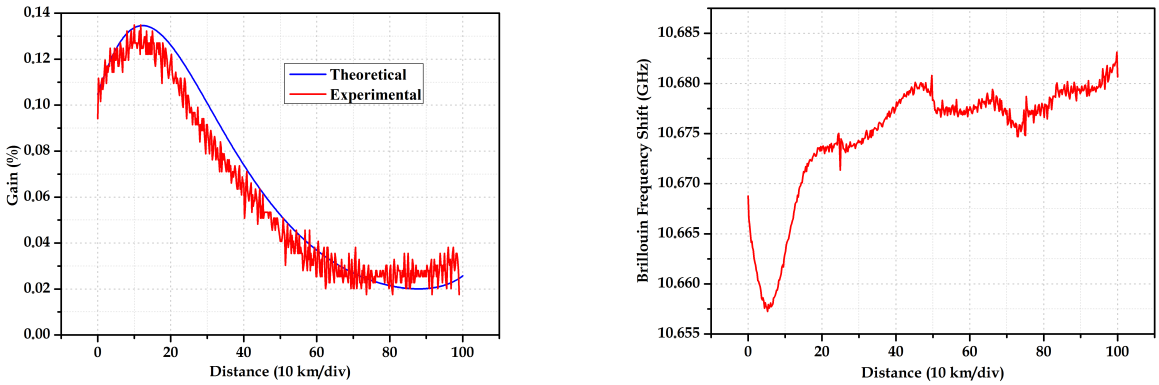

(a) (b)

Figure 4.3: *First-order Raman-assisted BOTDA results for the maximum gain value at each position (a) and for the BFS (b) for 100 km SMF. The gain is compared with theoretical simulations [42].*

Figure 4.4 shows a representation of the full frequency sweep developed from 10.58 GHz until 10.74 GHz for the target fiber. It is noticeable that the gain as a function of the frequency fits the expected Gaussian profile, and no appreciable depletion is visible. The maximum gain contrast is achieved at approximately 15 km of the fiber input while the minimum gain contrast is obtained around 75 km. This behavior is, as expected, due to the effect of the bi-directional First-order Raman amplification scheme. From here onward, the gain contrast keeps increasing until the end of the fiber.

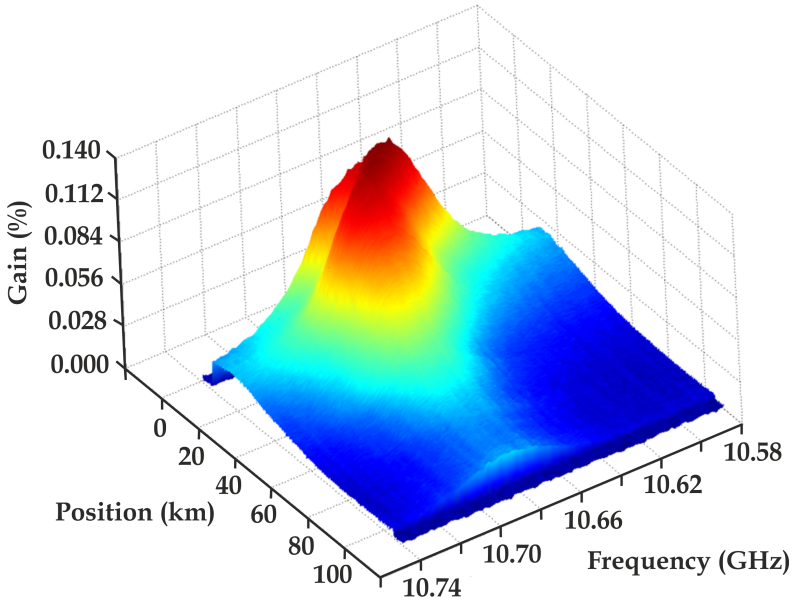

Figure 4.4: *Illustration of the full gain sweep over 100 km of SMF with 2 meter resolution from 10.58 GHz until 10.74 GHz [42].*

In order to test the proper performance of the employed BOTDA as a sensor, we decided to locate a hot-spot between the last two fiber spools. In this region ($\sim$ 75 km), where the gain contrast is minimal, it can be tested if the equipment performs properly even in the worst conditions. 2 meters of fiber were introduced in a water bath at 60 °C ($\pm$ 5 °C), with a room temperature of 20 °C. Figure 4.5 shows the frequency sweep performed around the hot-spot location. We can clearly see the hot-spot at the expected position, roughly 74.83 km. We can also observe the transition between the third and fourth fiber spool at approximately 74.80 km. The frequency difference between the hot-spot and the rest of the fiber arises from 10.67 GHz until 10.71 GHz, which equals to 40 MHz. Considering the sensitivity of 1 MHz/°C in the Brillouin shift, gives us a temperature variation of 40 °C, which is in good agreement with the expected temperature difference.

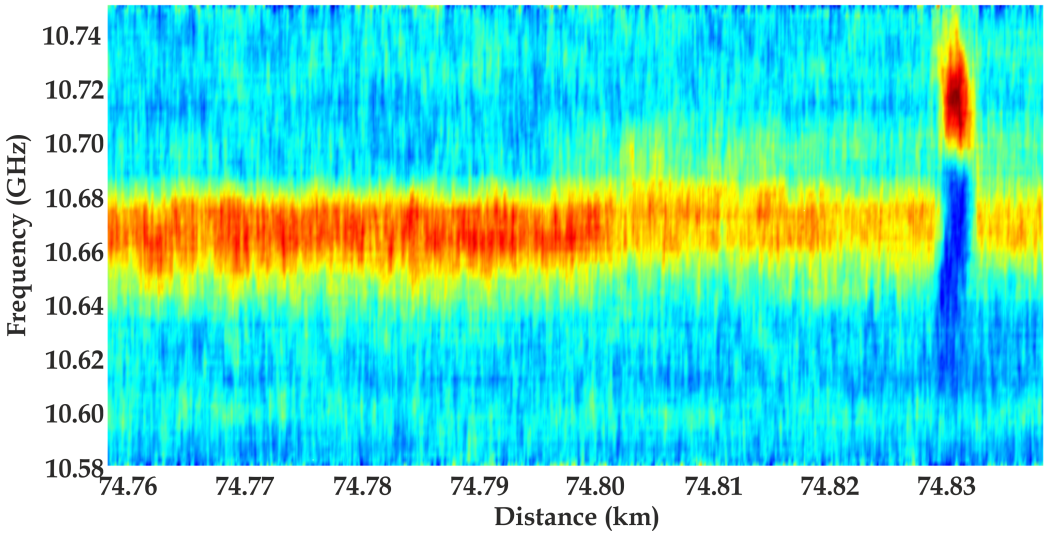

Figure 4.5: *Brillouin gain sweep from 10.58 GHz until 10.75 GHz around the hot-spot location at the lowest gain region ($\sim$ 75 km) [42].*

4.4 Extending the Real Remoteness of Long Range BOTDA Systems

In the previous developed experimental setup (subsection 4.3.1), the achieved sensing distance ranged 100 km. If this length is applied into a linear monitoring application, e.g. long pipelines or offshore monitoring, the real remoteness of the system is actually half of the total length; 50 km for the cited particular case. This arises since pump and probe signals must propagate in counter-propagating directions along the optical fiber, and therefore, the BOTDA interrogation unit requires access to both fiber ends. As some of the mentioned applications require to linearly monitor distances above 75 km, which means a total length of at least 150 km, the probe wave reaching the receiver will be highly attenuated, and therefore, no sensing capabilities or an extremely degraded sensing performance is expected. To overcome such issues it has already been proposed the use of bi-directional in-line EDFAs in terms of optical power increase along the whole optical fiber [103, 104], partially compensating the fiber loss on both probe and pump Brillouin waves. However, in several applications for ultra-long remote sensing, no electrical power is available at the farthest point for optical amplifiers.

In order to overcome the cited problem, we propose the use of a sensing scheme that doubles the fiber length connected to the BOTDA sensing unit while only half of it is employed for sensing purposes [103]. Under this design, known as the "Linear Sensing Fiber Configuration" [46,47], the first half of the fiber is used for distributed sensing aims (called "sensing fiber" from now on) while the second half is utilized to drive the probe to the farthest point in the sensing fiber (labeled as "carry-over fiber"). As we already know, it is possible to increase the sensing range of BOTDA sensors until 100/120 km through First- or Second-order Raman amplification [42, 44, 45] and/or S-code or Bipolar pulse coding [48, 50, 105]. It will be totally attainable to apply the cited techniques in the proposed very long linear scheme, although the high probe attenuation and the limited sensitivity of the optical detection stage make the design and power optimization much more challenging when compared to the use of the typical scheme. One of the main limitations in such terms is the origin of spontaneous Brillouin scattering, due to its additional loss induction to the probe wave. Also, it has been reported that a power symmetry among the two probe sidebands provides strong robustness against pump depletion in long fiber schemes [62]. Thus, the impact of any potential probe power imbalance in ultra-long range sensing is highly detrimental.

In this section, an ultra-long range BOTDA sensor in a linear configuration without any powered elements in the sensing loop is implemented based on the optimized design of a "seeded" Second-order distributed Raman amplification scheme [106,107] in combination with the optical pulse coding technique [48,77,78]. While Raman amplification is used to increase the probe power beyond the minimum detectable level, the pulse coding enhances the probe power contrast resulting from the Brillouin gain, thus enhancing the Signal to Noise Ratio (SNR) of the measurements [48].

4.4.1 Proposed Sensing Scheme

In the proposed linear sensing configuration, the probe signal cumulates twice the effect of fiber attenuation, which actually makes a big difference when compared to the basic fiber configuration. For instance, to extend the remoteness of the sensor up to 120 km, the longest sensing distance with a BOTDA reported so far [108], our proposal will require a 240 km fiber-loop. Under such a condition, the probe signal is attenuated by about 48 dB while propagating along the entire optical fiber before reaching the receiver. As a consequence, the CW probe power at the receiver is expected to be reduced by 24 dB when compared to the power measured in the basic configuration. This situation actually imposes a significant technical challenge to the design and implementation of the proposed ultra-long range BOTDA system.

It is worth mentioning that the maximum probe power inside the fiber is limited by the onset of amplified spontaneous Brillouin scattering. The threshold for this phenomenon is about 7 dBm (5 mW) in standard optical fibers [62]. Considering that fact, in a 120 km linear scheme (240 km fiber loop), the maximum probe power arriving to the sensing fiber segment will be -17 dBm (20 μW) after suffering 24 dB of attenuation all along the carry-over fiber. Obviously, before reaching the receiver, this low probe power level is expected to be further reduced until $\sim$ -41 dBm (70 nW) (another 24 dB of attenuation), which results in a power level that is difficult to detect even if a low-power preamplifier is used. Therefore, in order to compensate for this additional attenuation of the probe signal, distributed Raman amplification provides a suitable solution to push the maximum

power levels of the pump and probe signals within the fiber allowing the probe signal to reach the minimum power levels required by the pre-amplifier at the receiver to produce an acceptable optical SNR at the photo-detector. However, the power levels involved in such long sensing fiber configuration need a dedicated optimization, as we will see in the forthcoming section, especially the ones occurring inside the carry-over fiber since the nonlinear effects occurring within it will have a significant impact on the power distribution of the signals propagating along the useful sensing fiber.

The proposed scheme is based on combining First- and Second-order Raman amplification together with pulse coding as shown in Figure 4.6.

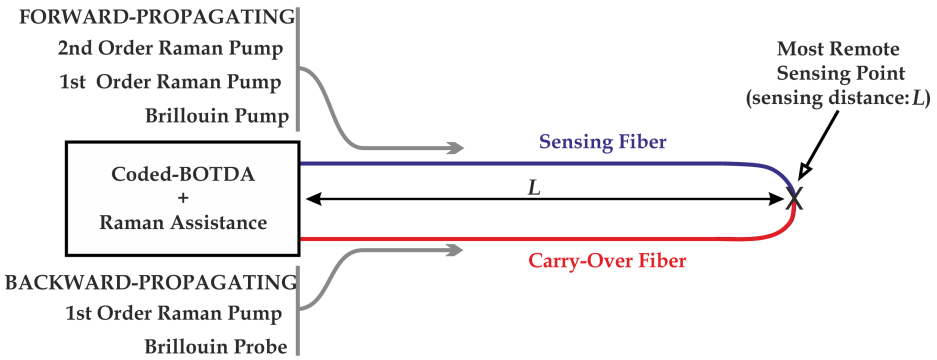

Figure 4.6: *Schematic diagram of the proposed ultra-long range BOTDA based on the linear sensing fiber configuration [47].*

The use of First-order distributed Raman amplification combined with optical pulse coding in BOTDA systems was proposed by Jia *et al.* in [109], although, it has never been combined the codification of the pump pulses together with Second-order Raman amplification schemes. On one hand, in order to increase the maximum distance reached by the coded Brillouin pump, a "seeded" Second-order Raman amplification scheme is implemented to amplify the pulse sequences [106, 107]. In this scheme, widely used in telecommunication systems [106, 107], a low-power First-order Raman pump at 1455 nm acts as a seed that is amplified by a high-power Second-order Raman pump at 1365 nm. Under this configuration, the maximum Brillouin pump power is shifted to a more distant location along the sensing fiber, around 30 km, an extension estimated to be about 15 km with respect to direct First-order Raman amplification. In terms of RIN transfer, the co-propagating nature (same direction as the pump wave, counter-propagating to the detected probe wave) of the Raman pumps produce and averaging of the noise over the whole amplifier transit time, resulting in an almost negligible impact of the RIN on the sensor performance due to the low cut-off frequency of the pump-to-signal RIN transfer function of the Brillouin scattering process in that configuration [49]. Also, the "seeded" nature of the First-order Raman pump (low power configured) helps to reduce the remaining RIN transfer to the detected signal. On the other hand, it has already been demonstrated in the previous section (4.3) the necessity to provide Raman amplification on the probe side to secure a good performance of the BOTDA sensor. In counter-propagating assistance (in opposite direction to the pump wave, co-propagating to the detected probe), a highly efficient pump-to-signal RIN transfer occurs [70], which means that the assistance in the probe side has to be performed using low-RIN Semiconductor Laser (SL) to minimize the pump RIN transfer to the probe signal. The use of Second-order Raman assistance to the probe wave is not recommended as it would result in a high and efficient pump RIN transfer, degrading significantly the SNR of the measurements.

Another important aspect of the proposed scheme is the use of pump pulses with Return-to-Zero (RZ) modulation format [110]. It is well known that RZ pulses are required to apply optical pulse coding in BOTDA sensors, suppressing bit patterning effects resulting from pre-excited acoustic waves [111]. It turns out that, in the case of Raman assistance, RZ pulses also have the advantage to minimize the Raman cross-gain modulation occurring when the counter-propagating Raman pump is depleted. Actually, a pulse separation of at least 50 ns is normally required to secure a complete decay of the acoustic wave amplitude between pulses of the code sequence. This time interval is much longer than the maximum walk-off between Raman pumps at 1450 nm and the Brillouin pump-probe signals at 1550 nm [70], which is of about 16 ns in conventional SMFs. Therefore, if the Couenter-propagating Raman pump at 1450 nm is depleted by the amplification of a single Brillouin pump pulse, no impact on the amplification of the following pulses from the same sequence is expected.

4.4.2 Power Requirements

Based on the analysis of requirements developed in section 4.2, it is important to control the power levels of the employed signals. In this case, the optimization will involve the First- and Second-order Raman pumps as well as the coded RZ-pulse sequence employed for the Brillouin pump wave.

The optimization procedure for the forward propagating signals must be carried out experimentally by knowing that, as a result of the First- and Second-order Raman amplification, the maximum Brillouin pump power occurs at about 15-30 km distance respectively, as shown in Figure 4.7. The maximum Brillouin pump power along the fiber can be estimated by monitoring the power of the Brillouin pump at the far fiber end in order to both maximize the Brillouin pump power at the end of the sensing fiber and to avoid that the maximum power exceeds the threshold of nonlinear effects. Considering the pulse shaping used, the maximum Brillouin pump power allowed in the system is limited by the threshold of MI, which is about 20-23 dBm (100-200 mW) (see subsection 3.3.1).

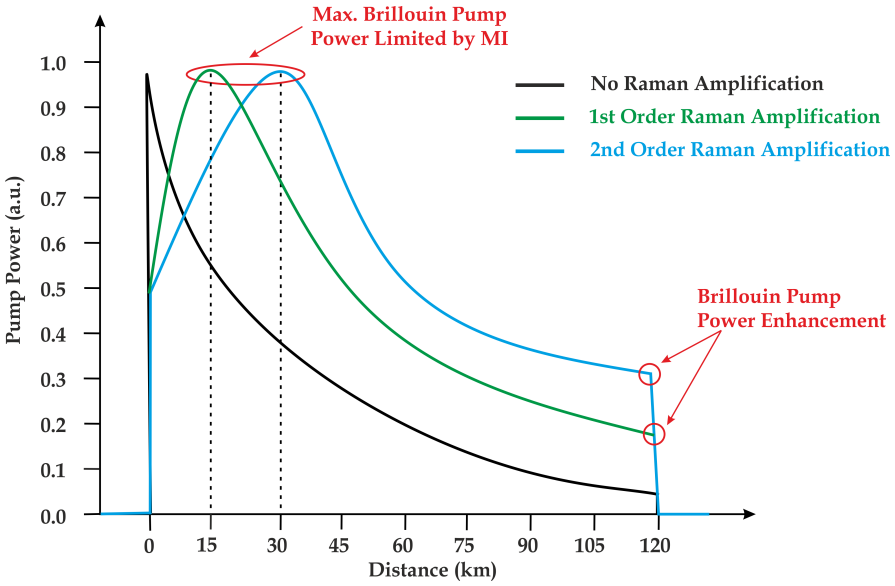

Figure 4.7: *Representation of the Brillouin pump power evolution along the sensing fiber under no amplification and assisted by First- and Second-order Raman amplification [47].*

In the case of the backward propagating Raman pump, it is adjusted to provide the highest possible probe power level at the end of the most distant sensing point as shown in Figure 4.8, but at the same time to make pump depletion negligible (subsection 3.3.2).

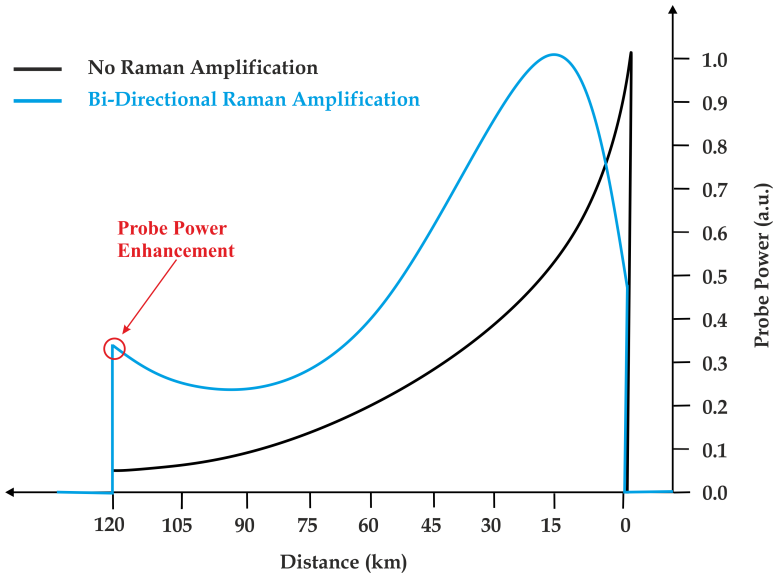

Figure 4.8: *Depiction of the Brillouin probe power evolution along the entire optical fiber loop assisted with and without First-order Raman amplification in the linear sensing fiber configuration [47].*

4.4.3 Experimental Setup

The whole work was developed at the GFO laboratory of the EPFL (Lausanne - Switzerland) as a collaboration with Dr. Marcelo A. Soto, Prof. Luc Thévenaz and Omnisens.

Figure 4.9 shows the experimental setup implemented to realize extremely long range distributed measurements along 120 km sensing distance, using a 240 km fiber-loop, and a spatial resolution of 5 meters. A LD operating at 1550 nm is the only optical source needed for the generation of Brillouin interacting signals in the system which is split into distinct branches to generate the coded pump signal and the probe signal.

The high-power pump signal is obtained using an EDFA and an EOM which modulates the CW laser light according to the Simplex-code (S-codes) sequences [77,78]. In this case the EDFA is placed before the EOM to avoid distortions in the pulse sequences [48] and configures a peak Brillouin pump input power of 7.5 dBm (5.6 mW). To induce Raman amplification along the optical fiber, the coded pulse sequences are coupled with two depolarized fiber Raman lasers through a 30/70 coupler respectively: a low-power seed First-order Raman pump at 1455 nm and a high-power Second-order Raman pump at 1365 nm configured at 16.0 dBm (40 mW) and 29.8 dBm (955 mW) respectively. All the selected power levels, referred at the input of the sensing fiber, avoid completely the appearance of MI, as stated in subsection 4.4.2. The probe signal is obtained using the well-known double-sideband technique [32], in which two equally spaced sidebands are generated by intensity modulation of the CW laser light. Thus, by adjusting the Radio Frequency (RF) modulation frequency on the EOM, the Brillouin Gain Spectrum (BGS) can be easily scanned. To minimize the Polarization Dependent Gain (PDG) of the distributed Raman amplification along the fiber, two orthogonally-multiplexed low-

RIN SLs at 1455 nm have been coupled with the probe signal using a Raman pump unit that provides a PDG lower than 0.5 dB. The avoidance of the phenomena mentioned in subsection 4.4.2, spontaneous Brillouin scattering and depletion, has been satisfied using an input probe signal of -12.9 dBm (51 μW) per sideband and a backward propagation Raman pump of 28.1 dBm (645 mW). Slightly higher power levels might be required to optimize the probe SNR at the receiver but, unfortunately, the low-RIN Raman pump module used in this experiment limits the maximum power launched into the carry-over fiber.

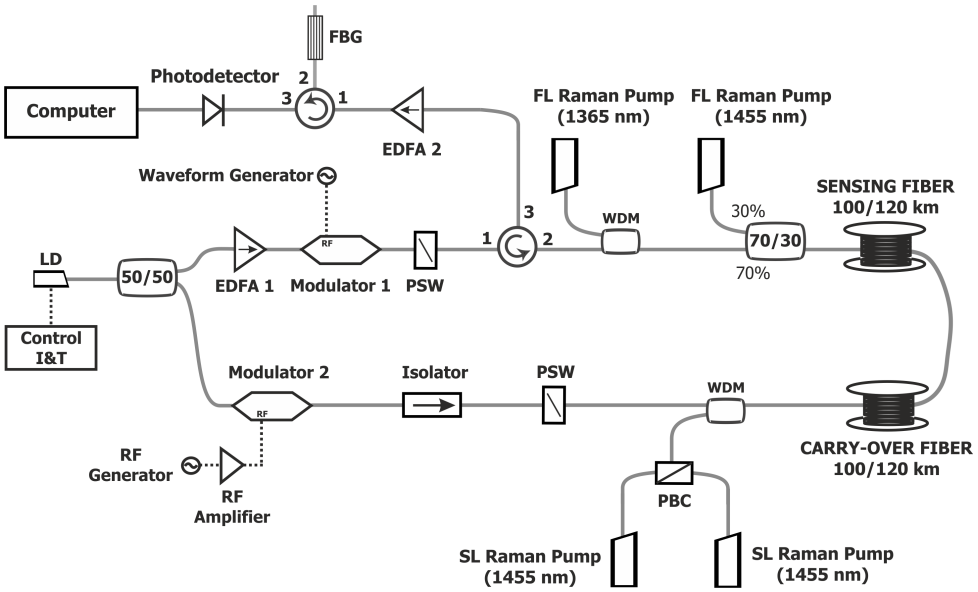

Figure 4.9: *Schematic representation of the experimental setup of the BOTDA sensor based on seeded Second-order Raman assistance and pulse coding [46,47]. LD: Laser Diode; I&T: Current and Temperature; EDFA: Erbium Doped Fiber Amplifier; PSW: Polarization Switch; WDM: Wavelength Division Multiplexer; RF: Radio Frequency; PBC: Polarization Beam Combiner: SL: Semiconductor Laser; FL: Fiber Laser; FBG: Fiber Bragg Grating.*

The optical fiber consists of several drums of standard SMF, with a total length of 240 km. Polarization diversity schemes, based on Polarization Switches (PSW), have been used in both pump and probe branches to reduce the polarization dependence of the BGS measurements. Before the receiver, an EDFA operating in linear-gain regime is inserted to increase the power level of the coded probe signal reaching the photodetector. A narrowband FBG is used to select one of the probe sidebands and to filter out other unwanted frequency components, such as the ASE noise from the EDFA, the Rayleigh signal generated by the coded Brillouin pump, the residual carrier of the probe and the second probe sideband. The data acquisition is carried through an acquisition card connected to a computer.

The 240 km long fiber-loop has been implemented to make possible measurements up to 120 km away from the interrogation unit. The first fiber half, which corresponds to 120 km of the sensing section, is composed by one 20 km fiber spool and two 50 km fiber drums (named as Fiber A, B and C respectively hereafter). The BFS for the fibers employed for sensing purposes was 10.68 GHz for Fiber A and 10.66 GHz for Fibers B and C at room temperature and zero strain. Note that although sensing fibers with slightly different BFS have been used in this experiment, the frequency difference ($\sim$ 20 MHz) is within the Brillouin gain spectral width. The remaining 120 km, which acted as carry-over fiber,

had a completely different BFS in order to clearly visualize the end of the sensing fiber at 120 km distance. In this case three spools were employed too with frequencies from 10.85 GHz to 10.90 GHz. Regarding the pulse codification, RZ S-codes with 255 bit have been applied in this case, offering a SNR enhancement or coding gain of 9 dB with respect to the single pulse case [77, 78]. The whole bit duration is set to 100 ns, while the single pulse duration is set to 50 ns resulting in a 5 m spatial resolution. Each coded BOTDA trace has been averaged 8 times, resulting in 2040 equivalent time averaged traces for each scanned frequency.

4.4.4 Results

Figure 4.10 shows a comparison between the experimental BOTDA trace (blue continuous line) at 10.66 GHz and the trace obtained by numerical simulations (red dashed line) using the mathematical models developed in subsections 3.3.4.1 and 3.3.4.2. It is important to point out that despite the extremely long optical fiber used in this case, it is still possible to distinguish the end of the sensing fiber at 120 km. The SNR at 120 km has been measured to be $\sim$ 6.5 dB, corresponding to a Brillouin gain of 0.03 %. Thus, the obtained SNR at 120 km distance is high enough to provide reliable measurements of temperature- and strain-dependent variations of the BGS.

Although a PSW is employed at each of the pump-probe branches of the setup to minimize the impact of Brillouin PDG, the measurements indicate that BOTDA traces turn out to be slightly affected by polarization noise when extremely long sensing fibers are used. Actually, it has been found that the used polarization diversity scheme, very common in standard BOTDA sensors, does not perform as expected with such a long optical fiber link. It is believed that this issue results from residual polarization noise coming from the finite ER of the two polarization switches which may lead to non-orthogonal states of polarization after propagation over several tens of km. In particular, it is observed that the residual polarization noise rises when the Brillouin gain increases, i.e. when longer code sequences are used, and has a larger impact at 30 km distance where the Brillouin pump reaches its maximum power, as shown in Figure 4.10.

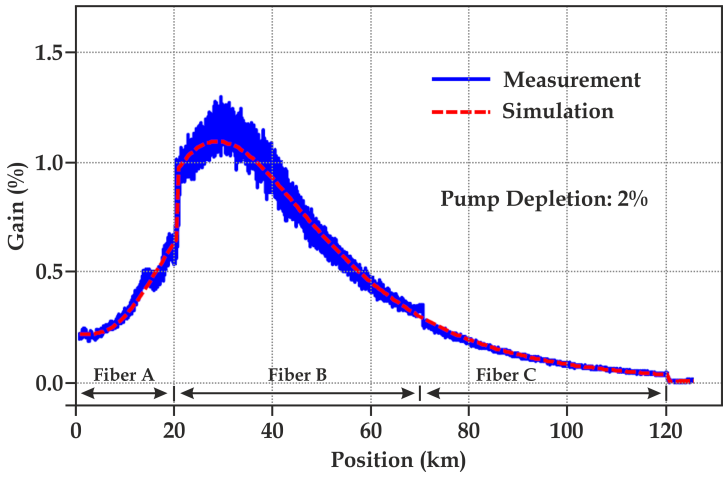

Figure 4.10: *Experimental and theoretical results of the Brillouin gain profile at 10.66 GHz for a 240 km-long fiber loop with 5 meter resolution [46, 47].*

The BFS along the fiber has been obtained by fitting the measured BGS at every fiber location, as shown in Figure 4.11. It can be observed that using a pulse sequence of 255 bits, the polarization noise has a negligible impact on the BFS estimation. The standard deviation over the last meters of fiber which corresponds to the lowest SNR region, has been calculated to be 1.9 MHz, corresponding to a temperature-strain resolution of 1.9 °C/38 $\mu\epsilon$ at 120 km distance. The pump depletion is estimated by measuring the power difference of the residual coded Brillouin pump with and without Brillouin interaction, which in this case is calculated to be 2.0 %, low enough to induce no biasing on the BFS measurements [109].

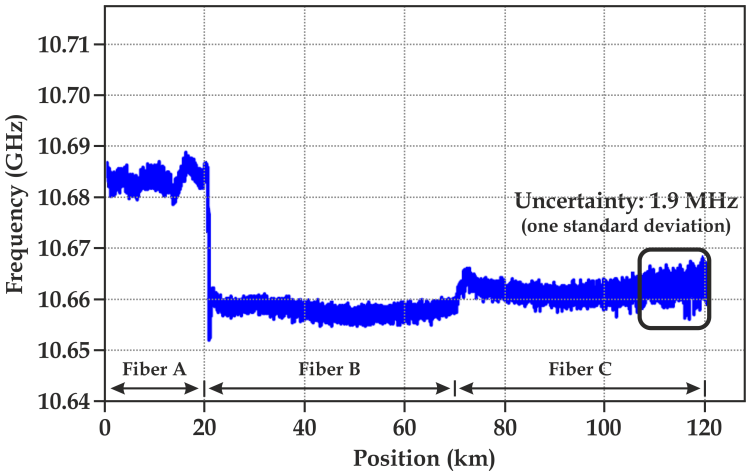

Figure 4.11: *Experimental BFS profile along 120 km sensing distance, exhibiting a maximum frequency uncertainty of 1.9 MHz [46, 47].*

Finally, measurements under extreme SNR conditions have been carried out; in this case a section of 5 m of fiber is heated up to 45°C at a 120 km distance, while the rest of the fiber is maintained at a controlled room temperature of 25 °C. Figure 4.12 shows the measured temperature profile for the last 100 m of fiber, where it can be clearly observed the 5 m hot-spot at 45 °C. It is important to mention that this result constitutes the first demonstration of distributed measurements at a real 120 km distance away from the interrogating unit using a BOTDA sensor with no repeaters along the entire optical fiber.

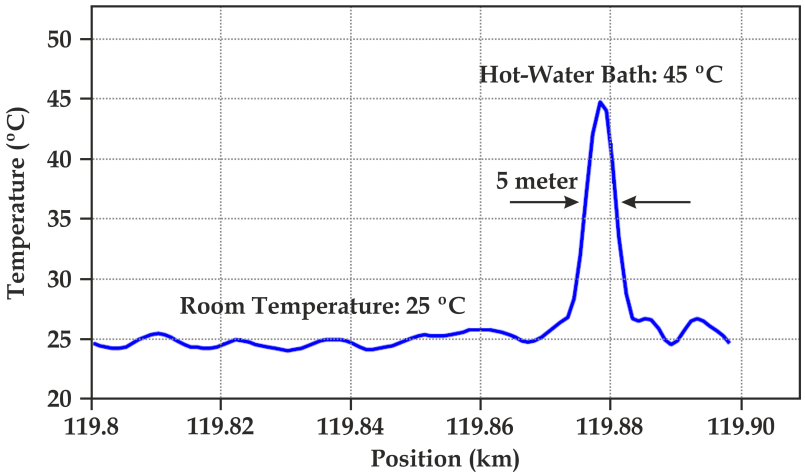

Figure 4.12: *Experimental representation of the detection of a 5 m hot-spot at the lowest gain region (∼ 120 km) over a 240 km-loop fiber length [46, 47].*

4.5 Conclusions and Open Lines

In this chapter we have shown the use of the techniques known so far to enlarge the sensing range of BOTDA systems; First- and Second-order Raman amplification and pulse coding [46, 47].

As it has been demonstrated, it is possible to enlarge the sensing range of such systems until 100 km through bi-directional First-order Raman assistance maintaining a fairly good resolution of 2 meters. It is also possible to arrive until 120 km if the proposed Raman amplification scheme is combined with pulse coding [50]. For the previous case it was necessary the use of SL-based Raman pumps with low-RIN transfer. These devices are the gate for extending the range of BOTDA systems as well as novel detection schemes as the ones described in section 5.1.

When the required application needs to locate the employed fiber in a linear configuration, the useful fiber length is divided by two. Therefore, applications beyond 60 km will require a total fiber length greater than 120 km. Under such conditions it will be necessary to apply the proposed sensing length known as "Linear Sensing Fiber Configuration" which is described in subsection 4.4.1. As the fiber lengths are greatly incremented, the use of combined First- and Second-order Raman amplification as well as pulse coding is required. In the cited scheme it is critical the optimization of the Raman pumps to maximize the system performance, avoiding nonlinear effects in the fiber. Finally, it is believed that further extension of the sensing range needs a novel conceptual step since the implemented system shows very little margin to increase power levels, including the Raman pump power, and to extend the code length.

Chapter 5

RIN Reduction in Long Range Raman-Assisted BOTDA Systems

5.1 Introduction

In chapter 4, it has been identified the necessity of using Raman pumps when enhancing the range of standard Brillouin Optical Time Domain Analysis (BOTDA) systems. For such purpose, the use of Raman Fiber Lasers (RFL) has been proved more effective for long or ultra-long setups since nowadays provide higher power levels and consequently are able to assist greater distances. Unfortunately, these pumps produce time-dependent variations on the acquired gain signal, known as Relative Intensity Noise (RIN - see subsection 3.3.5) [70], that damage the performance of the BOTDA.

It is important to realize that RFLs show a spectrum composed of many modes with a periodic spacing. This periodic mode spacing, which is normally in the hundreds of kHz or few MHz range for typical fiber lasers, leads to the appearance of some quasi-periodic intensity perturbations which may not be removed even after the usual trace averaging procedure, in particular, when the mode spacing happens to be a multiple of the pump pulse repetition rate, as shown in Figure 5.1(a). Since the RFL shows a chain of modes in the spectrum, its output displays some quasi-periodic intensity perturbations in multiple frequencies of the free spectral range of the laser. These quasi-periodic perturbations are transferred to the probe signal and may not be easily averaged out in the acquisition procedure if the acquisition trigger period is a multiple of the cavity round-trip time as depicted in Figure 5.1(b).

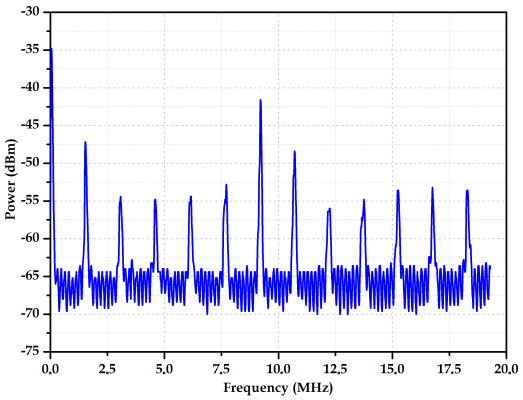

(a)

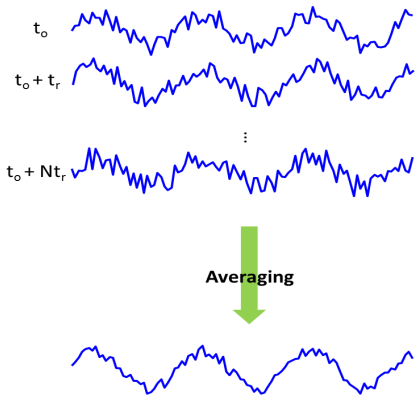

(b)

Figure 5.1: *Electrical Spectrum Analyzer (ESA) spectrum of the RIN noise of a 1455 nm RFL (a) and representation of the averaging procedure of RIN transferred Raman amplified signals (b) [44].*

Due to its nature, RIN transfer has been identified as a major impairment in BOTDA systems when Raman assistance elements are employed [39, 42, 49]. Thus it will be necessary to employ different measuring or data treatment techniques to avoid or reduce the cited detrimental effect.

In this chapter, we propose two different alternatives; the use of a Vector-BOTDA (VBOTDA) [112, 113] and a "de-noising" technique [44]. A VBOTDA is a BOTDA based technology that transfers the detected probe wave to a high frequency region ($>$ 500 MHz) where the RIN effect is less harmful. The de-noising procedure is based on a numerical treatment process that removes the quasi-periodic noise elements transferred to the retrieved probe wave. The effectiveness of the de-noising technique was tested in terms of resolution improvement through the application of the Differential Pulse-width Pair (DPP) technique (see subsection 3.4.3).

5.2 Vector-BOTDA

A standard BOTDA detects the probe wave in a low frequency range, from Direct Current (DC) to a few hundreds of MHz. This precise frequency range is exactly the same in which RIN transfer from the Raman pumps to the probe is maximized. Therefore, this makes extremely difficult to distinguish the target Stimulated Brillouin Scattering (SBS) signal from RIN transfer or other low frequency noise perturbations.

In a VBOTDA, the probe wave is transferred to a high frequency region (> 500 MHz), where the effect of RFL perturbations is considerably reduced. The use of this measuring technique in terms of low-frequency noise diminution was first demonstrated in 2010 by Dossou *et al.* [114]. That is why we propose the application of this measuring technique to reduce the effect of RIN transfer. Its effectiveness lies in the large walk-off times between the Raman pumps and the BOTDA signals induced by chromatic dispersion (see subsection 2.3.1) which amounts several periods of the carrier frequency in the VBOTDA. This causes any noise perturbation in the Raman pump to slip along several signal periods, amplifying the whole signal more homogeneously and reducing significantly its deleterious effect.

In a different way to standard BOTDA systems described all over this thesis dissertation, in a VBOTDA the probe wave is obtained through phase modulation, instead of intensity modulation. As the probe wave needs to be transferred to a high frequency region and also be swept in order to fully recover the spectrum of the interaction (see subsection 3.2.1), two frequencies are necessary. This can be developed with a unique phase modulator driven by two frequencies [114] or through two phase modulators commanded by one frequency each, as employed in our experimental development (see subsection 5.2.1). If two frequencies are driven within a unique modulator, a non-linear intermodulation arises leading to the apparition of new frequencies, degrading the performance of the system. Therefore, by using two modulators there is no mixing among the driving frequencies.

In addition to gain measurements, in a VBOTDA phase measurements can also be obtained. Several phase-related techniques have already been reported such as vector SBS measurements in a continuous way through Optical Vector Analyzers (OVA) [115], or the use of phase modulators for distributed high resolution sensing purposes [93, 116], where the intensity pulse of the pump is replaced by a phase pulse.

In all cases, unlike in a VBOTDA, no phase measurements were reported, which is one possible path for plausible real time measurements [117–119]. Also, the use of phase measurements, as recently has been reported by Urricelqui *et al.* [120], can be employed in order to avoid the appearance of non-local effects [29] in terms of pulse depletion.

5.2.1 VBOTDA Modulation Scheme

As stated, in our VBOTDA the probe wave is obtained through two phase modulators. These devices are going to be driven by one frequency each: a Local Oscillator Frequency (F_{LO}), fixed at 750 MHz for our particular case, far enough from the RIN transfer region and without significant chromatic dispersion impairments, and the so-called Scan Frequency (F_S), which is swept around 10 GHz. In this way, as represented in Figure 5.2, the probe wave spectrum is therefore going to be formed by the following frequency couples: $\pm(F_{LO})$, $\pm(F_S)$, $\pm(F_S - F_{LO})$ and $\pm(F_S + F_{LO})$.

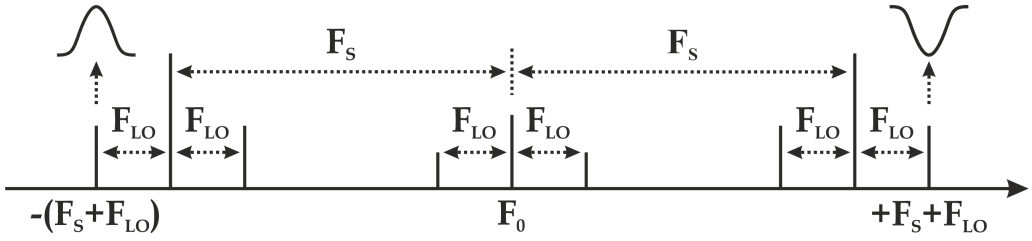

Figure 5.2: *Schematic representation of probe wave phase modulation sidebands present on the VBOTDA scheme [113]. F_0: Original Master Frequency; F_{LO}: Local Oscillator Frequency; F_S: Scan Frequency.*

The experiment is tuned so that the frequency couple $\pm(F_S + F_{LO})$ will be located around the Brillouin shift of the fiber (F_{BGS}), and the scanning of F_S will allow to scan this frequency over the Brillouin gain of the fiber under test. Under no Brillouin gain, the detected beat note between F_S and $F_S + F_{LO}$ is completely compensated by the beat note between F_S and $F_S - F_{LO}$ since they have opposite phases. Yet, if F_S is arranged so that $F_S + F_{LO}$ is located around the Brillouin Gain Spectrum (BGS) of the fiber, then the $-(F_S + F_{LO})$ sideband will be amplified and $+(F_S + F_{LO})$ attenuated. The phase modulation imbalance will then produce an intensity beat note at F_{LO}. The detection of the amplitude of the intensity modulated F_{LO} frequency as a function of time through a high-bandwidth photo-detector will provide both phase and amplitude information of the BGS [114].

5.2.2 Experimental Setup

The whole work was developed at the PhLAM laboratory of the University of Lille 1 (Villeneuve d'Asq - France) as a collaboration with Prof. Pascal Szriftgiser.

The developed experimental setup, which can be observed in Figure 5.3, is mainly based on introducing a First-order bi-directional Raman amplification module to the VBOTDA developed in [114]. Its operation principle is similar to a standard BOTDA: a pulsed pump wave interacts locally with a frequency shifted continuous counter-propagating probe wave through SBS. As usual, both pump and probe signals are obtained from the same master source, which in this case is a low-noise $\sim$ 500 kHz linewidth Laser Diode (LD) emitting at 1550 nm.

The pump wave is achieved by pulsing the continuous output of the LD with 200 ns pulses in this case (20 meter resolution) and afterwards amplified through an Erbium Doped Fiber Amplifier (EDFA) to obtain pulses with $\sim$ 5.44 dBm (3.5 mW) peak power. The pulse width has been chosen to increase the contrast over the elevated DC leaked component, which arose since it was no possible to employ high Extinction Ratio (ER) pulsing elements, such as SOAs [44, 121]. The low peak power is set so as to achieve results comparable, in terms of gain, to the ones obtained in previous subsections (4.3.2, 4.4.4), $\sim$ 1 %. The probe wave is obtained through the modulation scheme proposed in subsection 5.2.1 and, in this case, it is also amplified to obtain a power level of $\sim$ -13.97 dBm (40 μW). The selected power levels ensure a proper trade-off between the detected signal level and the prevention of the already known undersired effects. Together with the pump and probe waves, a RFL emitting at 1455 nm and relatively high RIN figure ($\sim$ -110 dBc/Hz) is introduced so bi-directional distributed Raman amplification is produced as well as noise transfer on the detected probe wave, so the effectiveness of the technique can be demonstrated.

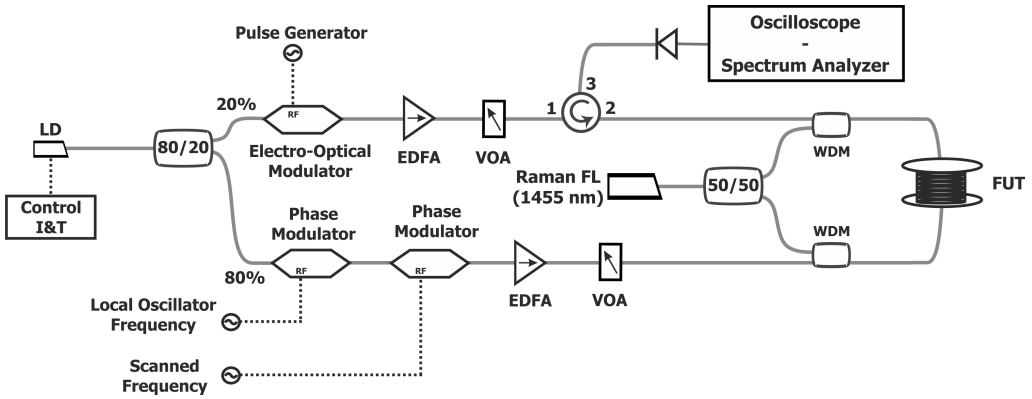

Figure 5.3: *Setup of the First-order Raman-assisted VBOTDA [113]. LD: Laser Diode; I&T: Current and Temperature; RF: Radio Frequency; EDFA: Erbium Doped Fiber Amplifier; VOA: Variable Optical Attenuator; FL: Fiber Laser; WDM: Wavelength Division Multiplexer; FUT: Fiber Under Test.*

As it has been said before, the employed setup has a considerable DC power level leakage due to the impossibility to minimize both the DC component of the generated pulses as well as the carrier frequencies of the phase modulators. Also, it has to be considered the amount of modulated signals present within the fiber (see Figure 5.2). This last issue could be avoided by using a unique sideband phase modulation scheme [37], although depletion in this case would be maximized. These setbacks degraded the performance of the setup forcing us to employ low power pump signals with considerably long pulse widths (200 ns). Although this could be seen as a drawback, it does not affect the main conclusions of this work as it does not affect the demonstration of the reduction of the RIN transfer effects caused by the Raman assistance. The complete setup can also be considered as an opening gate to real-time measurements in long range BOTDA systems thanks to the steep linear phase response of the interaction around the center frequency [118].

5.2.3 Results

5.2.3.1 RIN Reduction

The verification of the RIN transfer reduction was developed by comparing the whole frequency spectrum of the non-modulated probe signal under Raman amplification with the normalized spectral power density of the probe wave noise without Raman assistance. As a simple test, the bi-directional Raman amplification was set at 27.4 dBm (550 mW); 24.4 dBm (275 mW) on the probe side. Figure 5.4 displays the detected RIN noise in the probe wave as a function of the frequency.

As it can be clearly seen, at low frequencies (< 200 MHz), where a standard BOTDA operates, the probe RIN level increases around 30 dB when the Raman pump is on (blue trace). By setting the probe wave to a 750 MHz modulation the noise increase produced by the Raman pump is reduced to 20 dB, which implies a 10 dB reduction in terms of transferred RIN noise. As the frequency increases, the noise is reduced even more (15 dB reduction at 1 GHz), however at higher frequencies the chromatic dispersion effect introduces a non-negligible Phase to Amplitude Modulation (PM-AM) conversion in the probe signal [1]. This implies a trade-off between RIN effects and chromatic dispersion effects. A good balance is found at $F_{LO} = 750$ MHz.

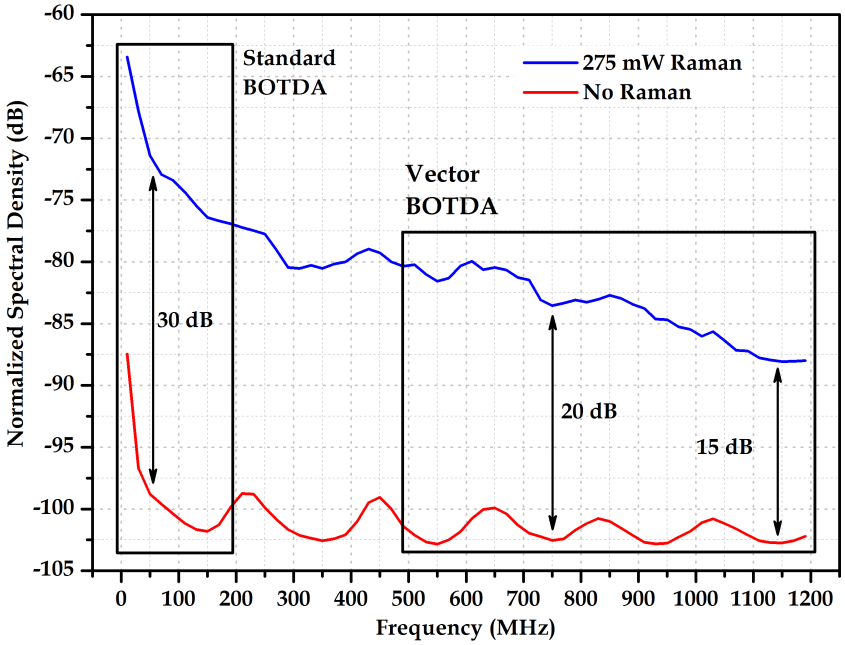

Figure 5.4: *Comparison of the spectral power density of the noise of the probe wave without Raman assistance and with 24.4 dBm (275 mW) of Raman amplification at each branch [113].*

In the experimental setup from Figure 5.3, the overall Raman gain introduced in the probe is roughly 17 dB. In conventional BOTDA conditions, the RIN increase, measured with the squared Fast Fourier Transform (FFT^2), is 30 dB, which implies roughly 15 dB noise amplitude growth, and therefore the Raman gain only introduces a 2 dB improvement in overall Signal to Noise Ratio (SNR). In the VBOTDA region, the noise amplitude growth goes down to 10 dB, implying a 7 dB growth in optical SNR, which should lead to a clear improvement in performance.

5.2.3.2 Sensor Performance

Once the RIN transfer reduction was proved and 750 MHz selected as the proper modulation for our purposes, the performance of the Raman-assisted VBOTDA as a sensor was tested. 84.5 km of fiber were monitored, formed by three spools spanning 40 km, 42.5 km and 2 km respectively, of which the first two had a maximum Brillouin Frequency Shift (BFS) of 10.86 GHz at room temperature ($\sim$ 20 °C) and the last one (2 km) had a BFS of 10.88 GHz (20 MHz difference from the first two spools). The sensor performance was checked by introducing the last 2 km of the total length in a temperature controlled oven at 60 °C and keeping the remaining 82.5 km of fiber at 20 °C constant controlled temperature. The 40 °C temperature difference is translated as approximately 40 MHz frequency shift (1 MHz/°C); thus, we expect to observe a 20 meter transition of 60 MHz (20 MHz + 40 MHz) at the 82.5 km position from 10.86 GHz until 10.92 GHz.

In Figure 5.5, the whole 84.5 km demodulated amplitude traces (82.5 km + 2 km) are shown, at the frequencies of 10.86 GHz and 10.92 GHz, which correspond to the BGS at 20 °C and 60 °C respectively. The acquisition is done with 500 averages. A clear gain shift in the end of the fiber is noticeable, and the contrast between the heated and non-heated sections is clearly visible.

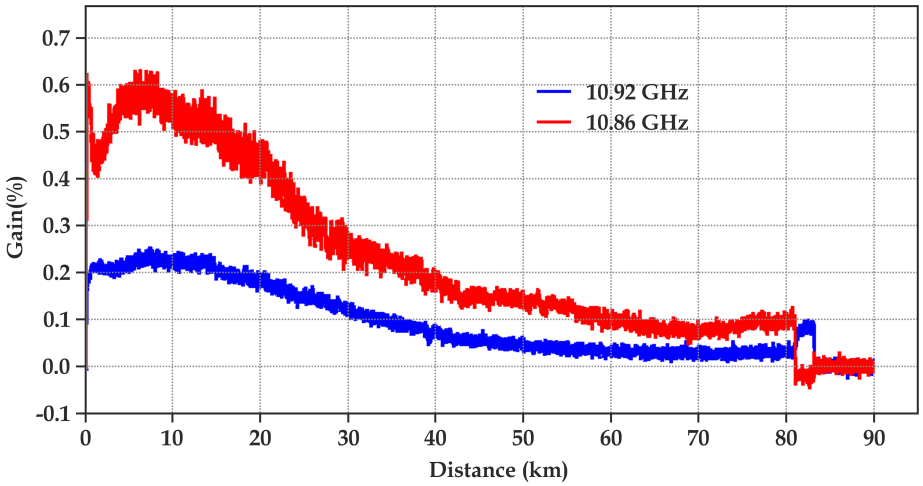

Figure 5.5: *Experimental spectrum analyzer with zero-span mode measurements for 84.5 km SMF for 10.86 GHz and 10.92 GHz [113].*

Based on previous results obtained with standard BOTDA systems over similar sensing distances (between 75 and 100 km) [39, 44], and similar gain values (< 1 %), it can be concluded that the RIN transfer is considerably reduced since the results have a neat determination with a relatively low number of averages. The fact that we could not increase the pump power significantly implied a significant loss in terms of achievable resolution. Similar gain values can be obtained with a high extinction ratio pulsing method (> 40 dB), a tenfold increase in peak power and a tenfold reduction in pulse width. However, the measurement of such low gain values would require thousands of averages in a conventional Raman-assisted BOTDA [39, 44].

A detailed gain and phase sweep of the transition between the heated and non-heated sections is represented in Figures 5.6 (a) and (b) respectively, where a complete switch of the gain position can be seen around the position of 82.5 km. The full gain switch is achieved in 20 meters, confirming the aforementioned resolution values. The detailed resolution representation can be observed in Figures 5.7 a) and b), results obtained from a 200 meter oscilloscope span. All the measurement were developed trying to obtain neat traces with the minimum number of averages possible, so as to illustrate the good RIN transfer capabilities of the setup. In this case 512 averages were employed, which is less than 10 times lower than the number of averages employed with standard BOTDA sensors for similar sensing distances and gain values [39, 44].

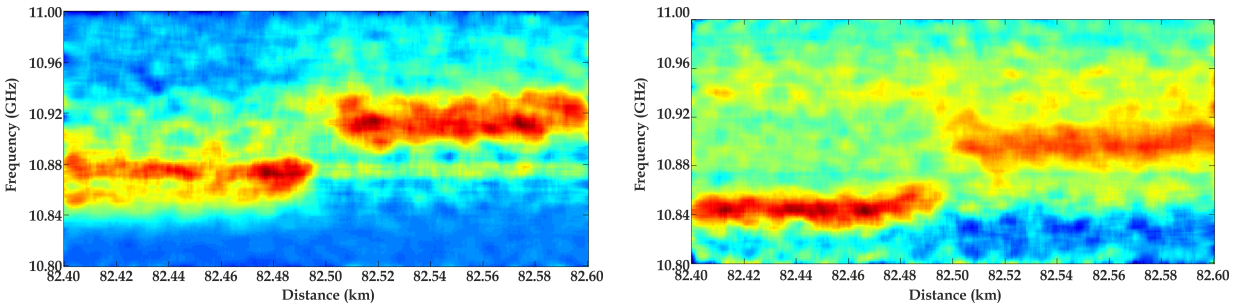

Figure 5.6: *Brillouin gain (a) and phase (b) measurements around the heated fiber section ($\sim$ 82.5 km) from 10.80 GHz until 11.00 GHz [113].*

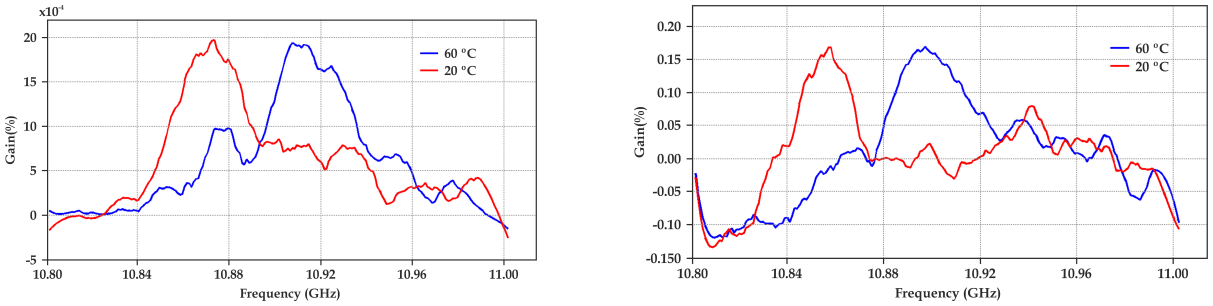

Figure 5.7: *Experimental gain (a) and phase (b) gain representations at 20 °C and 60 °C from 10.80 GHz until 11.00 GHz [113].*

It is noticeable that the frequencies from the phase measurement show maximums that are slightly lower than the ones obtained from the gain trace. This arises since the phase shift at the maximum gain frequency experiences a steep switch from maximum to minimum phase around the maximum frequency, the maximum phase shift being approximately 20 MHz lower than the peak gain. As it is visible, the frequency difference perfectly matches the expected 60 MHz.

5.3 De-Noising Procedure

In the Introduction of this chapter 5.1, it was mentioned the quasi-periodic nature of the RIN noise in case of RFL pumping and the difficulty to remove it with standard averaging techniques. One possibility to avoid RIN effects is precisely to employ this periodic feature. As RIN transfer from RFL pumps manifests as peaks in the probe spectrum, that can be eliminated using numerical processing techniques. This procedure, that we will call "de-noising" [44], takes into account the fact that the frequency positions of the periodic perturbations introduced by the RIN are not strictly fixed since the Raman laser cavity is long and thermal drifts may favor different mode beating frequencies. In our case, a digital filtering algorithm has been put forward to eliminate this quasi-periodic noise in the traces. This algorithm is based on obtaining the FFT of the Raman amplified signal where the RIN transfer effect appears as discrete peaks. That nature can be observed in Figure 5.8, where it is appreciable that the cited peaks can be easily removed with a digital filtering technique. The use of this algorithm can be completely justified when employing a BOTDA as a sensor since, conventionally, they are not made to detect any periodic strain or temperature variations. On the contrary, they are normally adapted to detect and measure hot-spots or particularly strained sections of short length (e.g. pipeline leaks, cracks in structures, etc.), anyway non-periodic variations of the Brillouin shift. Sharp peaks in the trace spectra corresponding to periodic trace variations can therefore be safely detected and eliminated in the processing step without affecting the measurement results. As we will see in forthcoming sections, the results from the point of view of hot-spot detection are notably better with this simple procedure.

In this case, the procedure to remove the quasi-periodic noise in the trace has been implemented as follows: in the initial step, a FFT of the raw trace, and its preceding and succeeding traces in the frequency scan is performed. These spectra are averaged and over the resulting spectrum a peak search algorithm is applied, which detects the frequency

positions showing a much larger energy over the four closest frequency bins. The threshold for this classification is established as 1 % of the zero-frequency component of the FFT. The located undesired frequencies and their corresponding symmetric in the spectrum are set to zero in the FFT trace. After this, the averaged trace is recovered again through an inverse FFT. Obviously, this procedure introduces an additional numerical noise in the trace, although its amplitude is very small. The overall result is an improvement of the signal quality. Furthermore, unlike other techniques, this procedure has no impact on the phase and therefore leaves the positional information of the trace fully preserved. If desired, it is also possible to execute an additional low-pass filtering at the cut-off frequency of the detector to ensure that any out-of-band noise in the acquisition is suppressed.

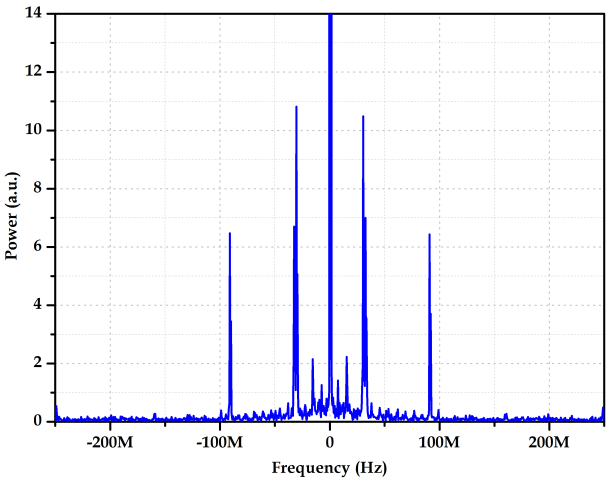

Figure 5.8: *Experimental representation of the FFT of the Raman amplified RIN transferred signal [44].*

5.3.1 Experimental Setup

The experimental setup is depicted in Figure 5.9. It is based on a BOTDA Gain configuration and it is very similar to the Raman assited BOTDA scheme described in 4.3.1, except for a couple of differences.

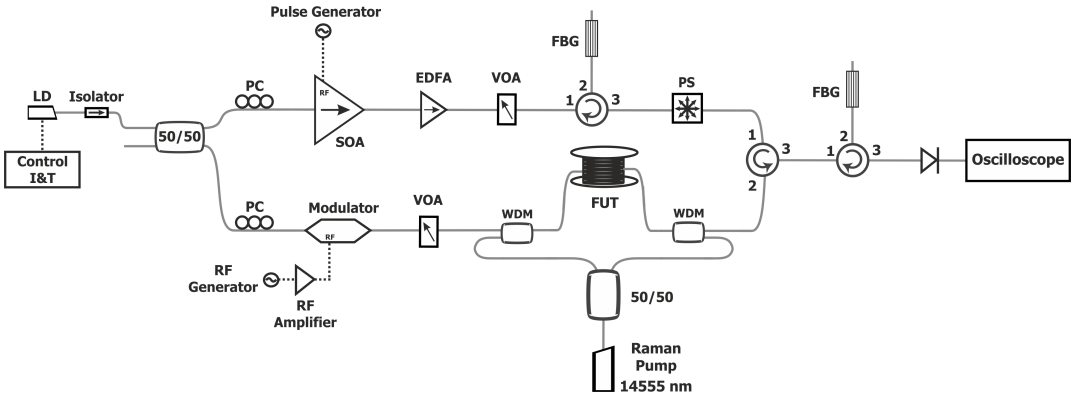

Figure 5.9: *Schematic representation of the experimental setup for the DPP BOTDA system [44]. LD: Laser Diode; I&T: Current and Temperature; PC: Polarization Controller; RF: Radio Frequency; SOA: Semiconductor Optical Amplifier; EDFA: Erbium Doped Fiber Amplifier; VOA: Variable Optical Attenuator; WDM: Wavelength Division Multiplexer; FBG: Fiber Bragg Grating; FUT: Fiber Under Test; PS: Polarization Scrambler.*

The first difference comes from the fact that the pump pulses are generated through a Semiconductor Optical Amplifier (SOA) instead of an Electro Optic Modulator (EOM) and a Non-linear Optical Loop Mirror (NOLM). This makes the setup easier to operate while the ER remains very high (> 50 dB) [121] and also helps to reduce one amplification stage in the detection stage, which improves the SNR of the measurement. The measurements were developed through the DPP technique so, in addition, the high ER of these pulses helps to improve the spectral purity in the measurements as shown in the numerical results of Minardo *et al.* [94]. The second difference comes from the use of a shorter wavelength LD, which presents a central wavelength at 1548.5 nm. In essence this does not have any impact on the experiment except that the filtering in detection is also shifted and the Brillouin shift curve is up-shifted with respect to the values reported in 4.3.2 for the same fiber spools.

Besides these novelties, the setup and the methodology to determine the adequate power settings are exactly the same as the ones employed previously in subsection 4.2.1. In this case 1, 0.8 and 0.5 meter resolutions were obtained. These differential measurements were accomplished by subtracting traces with 65 and 55 ns pump pulses for the case of 1 meter resolution (10 ns difference equals 1 meter resolution), 65 and 57 ns pulses for 0.8 meter resolution and 65 and 60 ns for 0.5 meters. The fall time of the pump pulses are reported to have a negative influence in the resolution of the system [94]. In all our cases, the fall times are below 2 ns, which theoretically should not have a significant impact on the achievable resolutions. The obtained gain traces are normalized to their respective pulse widths, which ensures that the gain subtraction is robust against small pump power variations. This procedure is correct as long as pump depletion effects can be considered negligible. In this particular case, the probe power is set below -10.45 dBm (90 μW), which ensures the avoidance of the appearance of spontaneous Brillouin scattering and depletion in case symmetric sidebands are employed [62].

The employed sensing fiber is composed by four Single Mode Fiber (SMF) spools of 25 km each with an effective area of 70 μm^2 and a similar BFS located at approximately 10.7 GHz for the emitting laser wavelength at $\sim$ 1548.5 nm. As the length of the employed pulses range between 65 and 55 ns, the power level of the Brillouin pump could be raised up to a value roughly 3 times higher than the ones employed in section 4.3 as the width of the pulses is approximately 3 times larger for the mentioned 2 meter resolution configuration (20 ns pulses). This is possible since the effect of Self-Phase Modulation (SPM) scales with the inverse of the pump pulse width (see equation 4.3) and therefore their power can be raised 3 times without adding any extra spectral broadening. Combining the peak power increase and the pulse width extend, the gain values recorded in the experiments of this work are roughly 10 times larger than the ones recorded in 4.3.2, as it will be shown below. The probe power is also increased obeying to a careful setting of the modulator working point to minimize the power imbalance between the two sidebands. As stated in subsection 3.3.2, with perfectly symmetric sidebands, the probe power can be theoretically raised up to a value close to the SBS threshold without entering into undesired depletion problems. All these variations lead to a > 10 dB increase in trace SNR. In summary, the peak power of pump and probe were set at 7.78 dBm (6 mW) and -10.9 dBm (81 μW) respectively, which as stated are in perfect agreement with the necessity of achieving the 100 km sensing range target and also in order to avoid any undesired effect that can damage the performance of our BOTDA system based on the tips provided in section 4.2. The Raman configuration was bi-directional, with 27 dBm (500 mW) of total pump power, $\sim$ 24 dBm (250 mW) per pump/probe branch.

5.3.2 Results

5.3.2.1 DPP Measurements

Figure 5.10 shows a gain trace recorded for the complete fiber length with a pulse width of 65 ns. The Raman pump power used is below the value necessary for a good compensation of the losses. However, this ensures a good behavior of the setup in terms of RIN transfer.

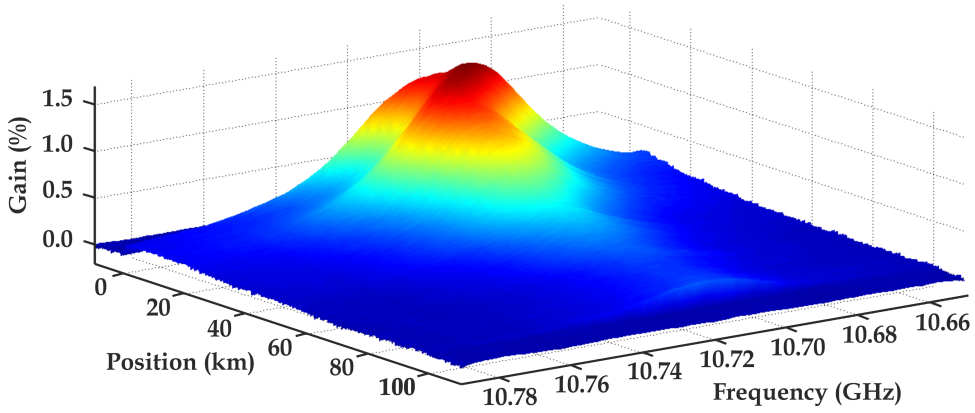

Figure 5.10: *Illustration of the full gain sweep over 100 km of Smf with 65 ns pulses from 10.66 GHz to 10.78 GHz [44].*

In this case, as it arose with the results obtained in 4.3.2, the minimum gain of the 100 km measurement was located in the 75 km approximately. Thus to validate the performance of our high-resolution long range BOTDA as a sensor, even in the worst conditions, a hot-spot was introduced between the last two fiber spools ($\sim$ 75 km), where the gain contrast is minimal. 1 meter of fiber was introduced in a water bath at 60 °C ($\pm$ 5 °C), with a room temperature of 20 °C. Figures 5.11(a) and 5.11(b) (65 and 55 ns pulses respectively) show the gain trace sweep around the hot-spot location for a probe frequency shift ranging from 10.66 GHz up to 10.78 GHz. As it can be seen, the BFS of the fiber is set at approximately 10.71 GHz all along the 100 meter span analyzed and at the hot-spot region, it can be seen that the gain at 10.71 GHz is reduced and a significant part of the gain is recorded at higher offset frequencies ($\sim$ 10.75 GHz). The distance over which this gain variation arises spans over the pulse length, not the actual fiber length (1 meter), being therefore longer for the gain sweep acquired with longer pulse length. The traces are not de-noised and therefore a periodic noise is visible at some positions.

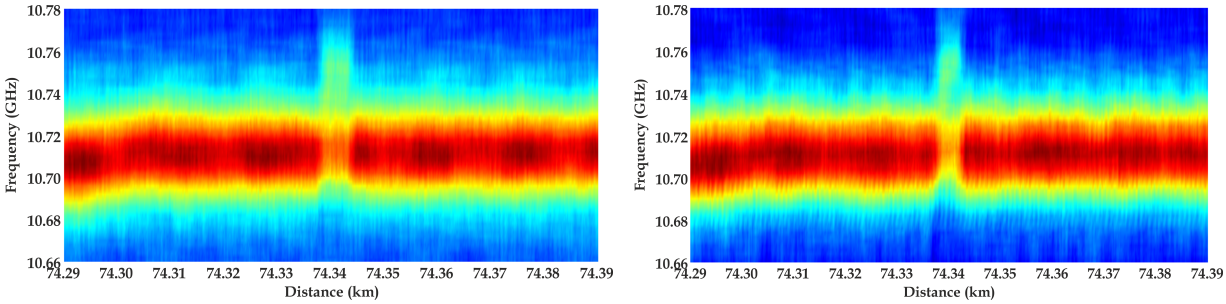

(a) (b)

Figure 5.11: *Brillouin gain sweep from 10.66 GHz until 10.78 GHz around the hot-spot location at the lowest gain region ($\sim$ 75 km) for 65 ns (a) and 55 ns (b) pulses [44].*

The result of the subtraction of these two traces is shown in Figure 5.12(a). A 1 meter hot-spot is clearly visible, in 74.343 km. The maximum gain clearly switches from the value of 10.71 GHz to 10.75 GHz. The 40 MHz frequency difference equals to 40 °C variation(1 MHz/°C), which actually matches with the expected temperature change.

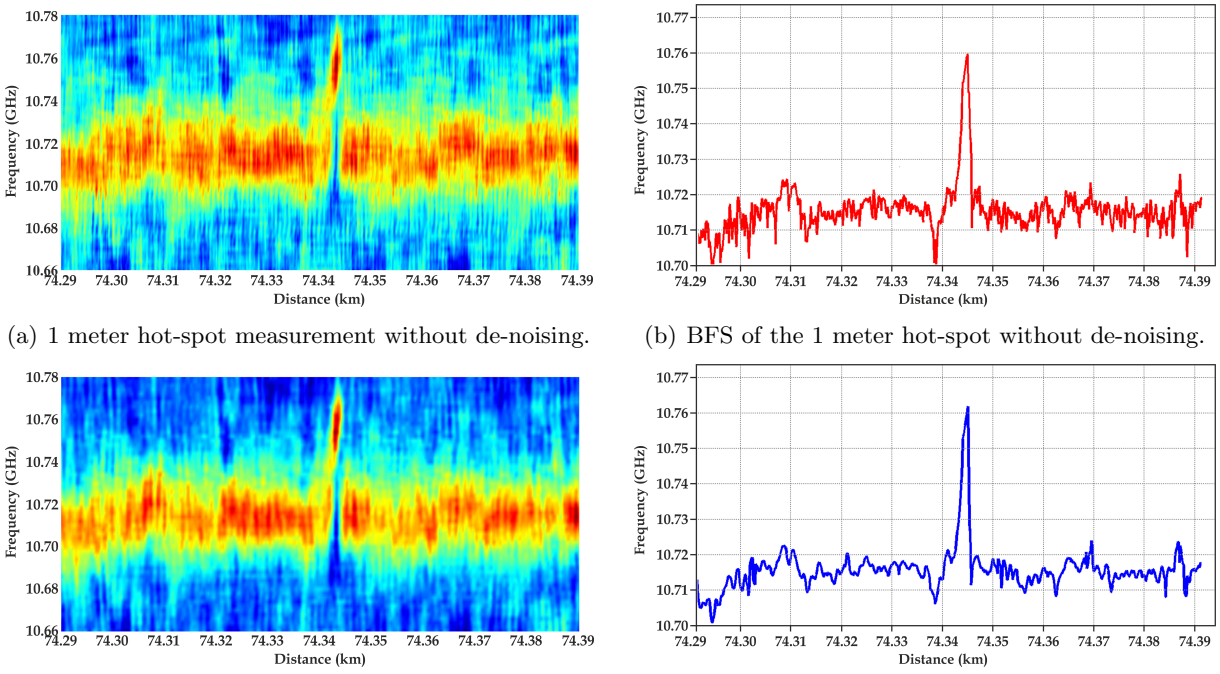

(a) 1 meter hot-spot measurement without de-noising.

(b) BFS of the 1 meter hot-spot without de-noising.

(c) 1 meter hot-spot measurement with de-noising.

(d) BFS of the 1 meter hot-spot with de-noising.

Figure 5.12: *Result of the subtraction between the 65 ns and 55 ns Brillouin gain traces for 1 meter hot-spot with and without the de-noising procedure applied [44].*

In Figure 5.12(a) it is appreciable a periodic noise all over the trace which corresponds to the RIN transfer from the Raman pump, which considerably degrades the quality of the measurement. That effect can be fully appreciated in Figure 5.12(b), where the BFS of the measurement is depicted. The Root Mean Square (RMS) frequency difference between consecutive traces equals 4 MHz, which is equivalent to 4 °C/80 $\mu\epsilon$ of uncertainty, a value far below from expectations. Thus, the de-noising procedure is applied to the obtained results and the result can be observed in Figure 5.12(c). It can be clearly seen that the contrast of the resulting gain trace sweep is upgraded, showing the efficiency of the developed procedure. In Figure 5.12(d) the BFS of the de-noised trace is represented, and in this case the RMS frequency difference is in the order of 2.5 MHz, which ensures a maximum uncertainty of 2.5 °C/50 $\mu\epsilon$. In conclusion, it can be said that our simple de-noising procedure helps to reduce the measurement uncertainty in $\sim$ 1.5 °C/30 $\mu\epsilon$.

In a second experiment, an attempt to perform the first sub-metrical resolution measurement over 100 km was developed. 0.8 meters of fiber were introduced in the hot bath and measured with 65 ns and 57 ns pulses, so the 8 ns pulse-width difference should provide 0.8 meter resolution. Figure 5.13(a) shows the result of the subtraction of both traces over a 50 meter span measurement with the de-noising procedure already applied. As it can be seen, the 0.8 meter hot-spot is perfectly detectable at the expected frequency position ($\sim$ 10.76 GHz). Figure 5.13(b) represents the BFS of the subtraction and in this case, compared to the case of 1 meter resolution, the RMS frequency difference between consecutive sweeps is in the order of 5 MHz, quite higher than before even though the de-

noising procedure is applied, which determines an RMS uncertainty in the measurement of roughly 5 °C/100 $\mu\epsilon$.

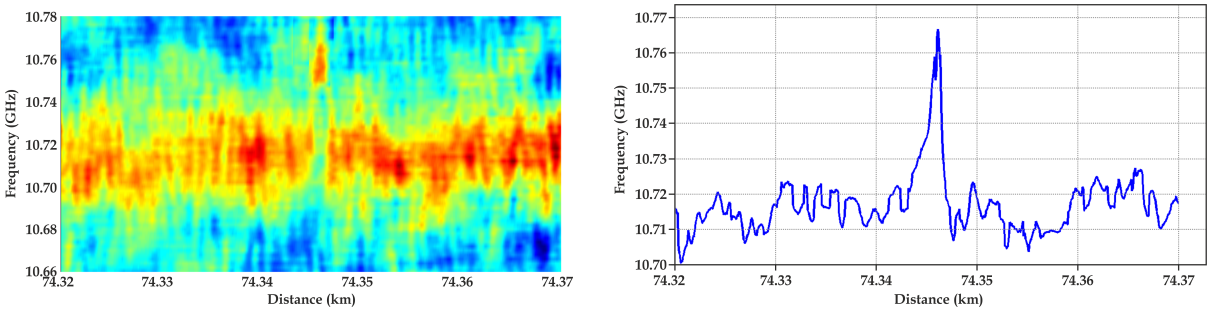

(a) 0.8 meter hot-spot measurement with de-noising.

(b) BFS of the 0.8 meter hot-spot with de-noising.

Figure 5.13: *Result of the subtraction between the 65 ns and 57 ns Brillouin gain traces for the 0.8 meter hot-spot [44].*

By comparing the results for 1 meter and for 0.8 meter resolution, it is noticeable a considerable decrease in the quality of the measurement in terms of noise, even when the de-noising procedure is applied. This noise problem becomes certainly impossible to handle at lower resolution values with the actual experimental arrangement. This is due to the simultaneous occurrence of two problems: first, the detection bandwidth has to be correspondingly increased, which implies an equivalent increase in noise bandwidth; second, the energy of the trace difference becomes smaller. To push further down the resolution, we decided to use Semiconductor Laser (SL) pumping on the probe side of our BOTDA. This type of lasers has much lower RIN values than RFLs, typically -140 dBc/Hz, and their positive use in BOTDAs has already been confirmed by Soto et al. in [49]. The choice of a SL pumping just in the probe instead of on the pump side relies on the fact that RIN transfer issues are minimized in the most critical direction.

5.3.2.2 Further Improvement Using a Semiconductor Laser

The employed experimental setup is depicted in Figure 5.14, and, as commented previously, the only difference regarding the initial development (Figure 5.9) is the introduction of a SL in the probe side of the scheme.

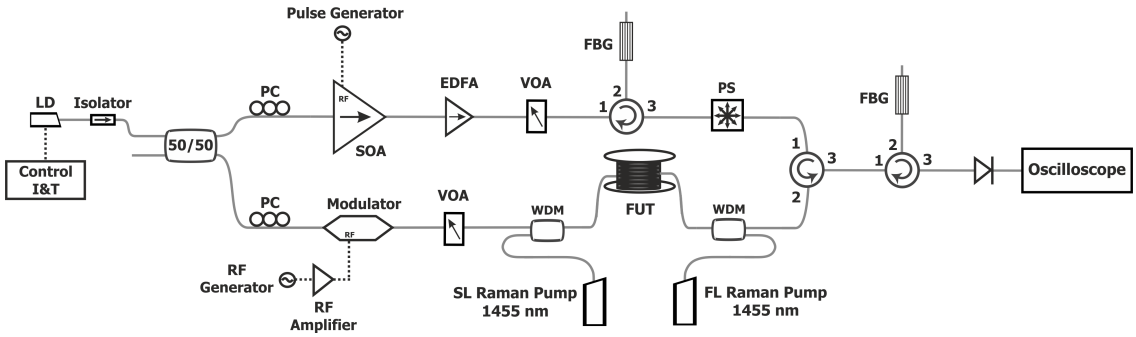

Figure 5.14: *Schematic representation of the experimental setup of the DPP BOTDA system with a SL pump in the probe side [44]. LD: Laser Diode; I&T: Current and Temperature; PC: Polarization Controller; RF: Radio Frequency; SOA: Semiconductor Optical Amplifier; EDFA: Erbium Doped Fiber Amplifier; VOA: Variable Optical Attenuator; WDM: Wavelength Division Multiplexer; FBG: Fiber Bragg Grating; FUT: Fiber Under Test; PS: Polarization Scrambler; SL: Semiconductor Laser; FL: Fiber Laser.*

As it was done previously, in this case 0.5 meter fiber length were introduced in the hot bath and two measurements were developed with 65 and 60 ns pulse widths. As stated at the beginning of the section, the power levels for the pump and probe waves were left unaltered, being 7.78 dBm (6 mW) and -10.9 dBm (81 μW) respectively. In the case of the bi-directional Raman pumping scheme, the idea was to keep similar power values to the previous cases so the obtained results are comparable. The Raman power supplied to the pump branch with the RFL was set at $\sim$ 24 dBm (250 mW) while the SL for the probe side emitted a total power of 23.6 dBm (230 mW), the maximum output supplied by the employed device. Although the amplification branches are slightly unbalanced, it is acceptable when comparing with previous results as the power difference is below 10 %.

In Figure 5.15(a) (100 m span measurement) it can be seen the subtraction between the obtained traces and once the de-noising procedure is applied. It is noticeable that the detection of the hot-spot is performed properly and that in this position ($\sim$ 74.34 km) the gain completely switches from 10.71 GHz to 10.76 GHz. The measurement quality is clearly better than the case of 0.8 meter explained before. In terms of measurement uncertainty, through the depiction of the BFS of the curve (see Figure 5.15(b)), the RMS for consecutive traces is obtained which in this case is 3 MHz. This value equals to 3 °C/60 $\mu\epsilon$ of temperature/strain determination uncertainty which as expected is below the 0.8 meter resolution measurements. Obviously, the uncertainty is still greater than the one achieved for 1 meter resolution, 2.5 °C/50 $\mu\epsilon$, but the improvement can be considered significant. In this case, this frequency uncertainty is essentially affected by three parameters: the trace noise whose main cause is still RIN transfer due to Raman amplification, the frequency step in our measurement, 2 MHz, and the gain bandwidth which is $\sim$ 30 MHz in this case.

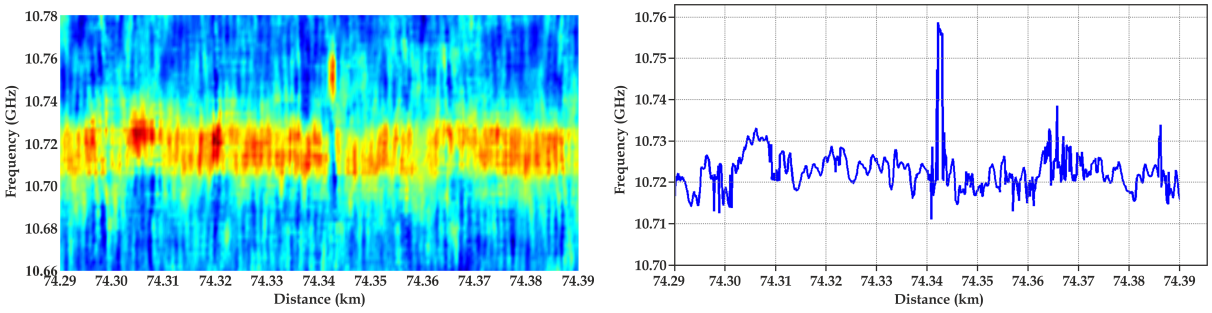

(a) 0.5 meter hot-spot measurement with de-noising.

(b) BFS of the 0.5 meter hot-spot with de-noising.

Figure 5.15: *Result of the subtraction between the 65 ns and 60 ns Brillouin gain traces for the 0.5 meter hot-spot with the de-noising procedure applied [44].*

The representation of the gain profile at the exact position of the hot-spot provides information about spectral purity issues due to imperfect ER in the employed pump pulses [94]. In Figures 5.16(a) and (b) the gain sweep for 1 meter and 0.5 meter resolution are depicted. As it can be observed, at the position of the hot-spot frequency ($\sim$ 10.76 GHz) there is a considerable gain increase, while at the section of the un-shifted maximum frequency ($\sim$ 10.71 GHz) there is almost a complete absence of gain which proves the good ER of the pulse generation section.

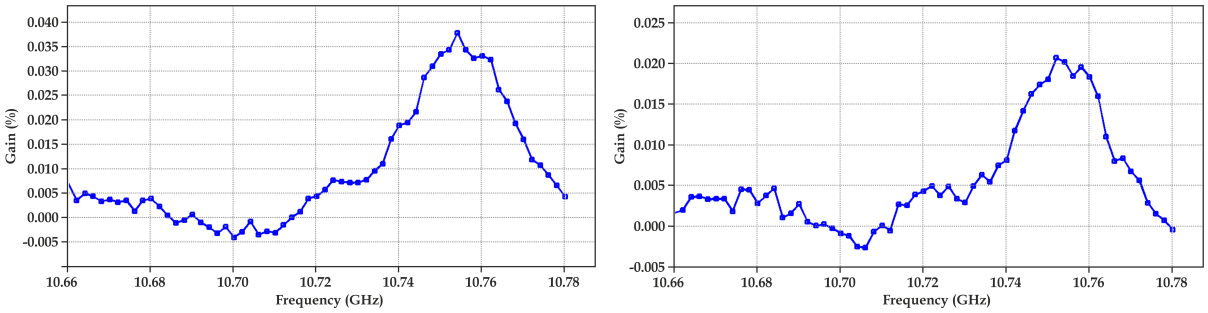

(a) (b)

Figure 5.16: *Gain profile at the hot-spot region for 1 meter (a) and 0.5 meter resolution (b) [44].*

5.4 Conclusions and Open Lines

As we have seen in this chapter, the detrimental effect of RIN transfer is not easily removable with simple averaging procedures due to its quasi-periodical nature in the case of RFL pumping. In order to reduce or remove it, as we have seen in this chapter, it is necessary to develop or apply either different measuring schemes or mathematical filtering procedures.

Firstly, we have proposed the use of a VBOTDA, that compared to a standard BOTDA uses a high-frequency modulated probe wave (500 MHz $< f <$ 1 GHz) that allows to reduce the RIN transfer effect over 10 dB. Further reduction could be achieved at higher frequencies, although a trade-off remains to be found since chromatic dispersion causes some undesired PM-AM conversion in the probe wave at higher frequencies, which reduces the dynamic range of the measurement [122]. In addition to the impairments due to chromatic dispersion, it is also remarkable the deleterious effect on the measurement noise caused by Four-Wave Mixing (FWM) [123, 124] among the different probe wave components. It should be considered that the spectral components in the probe wave are polarization-aligned and close in frequency. Under these these conditions FWM is maximized, as the phase mismatch vanishes [1].

Secondly, a novel numerical de-noising technique has been presented, which removes almost entirely the noise transferred from the Raman amplification pumps to the detected amplified probe wave. By analyzing the FFT of the detected signals it is possible to distinguish the frequency pattern of the transferred noise and remove it mathematically without distorting the target signal. Through this simple procedure, it is viable to reduce the uncertainty of the measurements in $\sim$ 1.5 MHz, which helped to be able to measure a 0.5 meter hot-spot in a 100 km fiber length through the DPP technique with just 3 MHz uncertainty in the determination.

The combination of both techniques could be the gate for real-time ultra-long range BOTDA systems with sub-metrical resolutions. For further improvement, it should be necessary to apply slightly different modified modulation or detection schemes since it is necessary to deal with associated issues such as chromatic dispersion and FWM.

Chapter 6

Conclusions and Open Lines

6.1 Conclusions

The main conclusions of the presented thesis dissertation are the following ones:

- All the linear and non-linear effects necessary to develop long and ultra-long range Brillouin Optical Time Domain Analysis (BOTDA) systems have been studied. A special focus has been given to the Stimulated Brillouin and Raman Scattering effects, as they constitute the basis of the treated distributed fiber optic sensors.

- A proper state of the art on BOTDA setups and range and resolution enhancing techniques has been addressed. Also, all of the non-desired effects that arise when trying to enlarge the range and resolution of BOTDA systems have been identified; Self-Phase Modulation (SPM), Modulation Instability (MI), depletion and Relative Intensity Noise (RIN) transfer.

- A refined First-order Raman-assisted BOTDA has been developed with the intention of validating its effectiveness as a long range measuring technique. The optimization has been done using simple analytical models. Also, a brand-new Second-order Raman-assisted pulse coded BOTDA system has been assembled to be able to range extremely long linear sensing configurations (120 km) and therefore provide sensing solutions to exceptionally challenging infrastructures.

- Two different Relative Intensity Noise (RIN) reduction techniques have been tested. The first one is a novel numerical procedure, called "de-noising", that eliminates the detected non-desired peaks of the periodical noise introduced to the detected signal by the employed Raman Fiber Lasers (RFL). The second one is the Vector BOTDA (VBOTDA), a Brillouin scattering measuring technique that modulates the detected signal to a high frequency carrier far from the frequency range where the RIN transfer effects are more deleterious.

6.2 Original Contributions

These are the original contributions developed to the thesis dissertation:

- A 100 km range First-order Raman-assisted BOTDA with 2 meter resolution and 1.2 °C/24 $\mu\epsilon$ measurement uncertainty in terms of temperature and strain has been developed using simple analytical modelling. This constitutes the validation of the proposed technique for range increase.

- In collaboration with the EPFL and the company Omnisens, for the first time to the best of our knowledge, a combination among Second-order Raman amplification and pulse coding on a BOTDA system has been produced. In this way a 240 km linear sensing scheme (120 km sensing distance) with 5 meter resolution and 1.9 °C/38 $\mu\epsilon$ of temperature/strain uncertainty has been achieved.

- A novel numerical RIN transfer "de-noising" technique has been developed that allows to reduce the detrimental effect that arises on the detected BOTDA signals when high power RFLs are employed to enhance the sensing distance.

- The resolution enhancer DPP technique has been applied over a First-order Raman-assisted BOTDA together with the "de-noising" procedure. This provided sub-metric resolutions over sensing distances of tens of kilometers. In our particular case, a 100 km sensing length system with 0.5 meter resolution and 1.9 °C/38 $\mu\epsilon$ of temperature/strain uncertainty was accomplished.

- In collaboration with the University of Lille 1, for the first time to the best of our knowledge, First-order Raman amplification has been applied to a VBOTDA. This combination allowed us to reduce the detrimental effect of RIN transfer in more than 10 dB.

6.3 Open Lines

After the studies and experiments developed over this thesis dissertation, we propose the following research open lines for the future:

- Raman assistance has been established as one of the preferred options for range extension purposes. Unfortunately, for the current demanded ranges the devices that provide optimum amplification levels are based on RFLs, that have a large RIN figure. Therefore, it is necessary to research on new amplification pumps based on Semiconductor Lasers (SL) to avoid the noise issues of RFLs as much as possible.

- Based on the previous statement, as it is still not possible to fully eliminate the RIN transfer, it is required to continue testing and or developing new detecting schemes that could reduce the deleterious effect of RIN transfer, such as VBOTDA, heterodyne detection or balanced detection. In particular, balanced detection in the probe signal might be a very convenient route to explore.

- Even though the effectiveness of pulse coding has been demonstrated for range enlarging, it is still not commonly employed in commercial systems, so it could be interesting to research new coding techniques easily applicable to the commercial development of BOTDA systems.

- The commonly employed mechanism for mitigating the polarization effect over the detected Brillouin signal, the Polarization Scrambler (PS), is based on small moving plates that introduces noise to the detected signal degrading its quality. Therefore, it is necessary to develop a mechanism that is not based on mechanical actuation to reduce the cited issue.

- All the BOTDA systems presented during this thesis dissertation require long measuring times to properly determine inhomogeneities at the position where the retrieved gain lower. Therefore, some applications that require a fast determination of the presented problem could not be satisfied. That is why it is necessary to develop dynamic measurement technique for the Brillouin Frequency Shift (BFS) determination that could be applicable for long range and high resolution systems.

- The resolution enhancer DPP technique requires to develop two full Brillouin Gain Spectrum (BGS) maps. This actually doubles the measuring, considerably reducing the scope of applications of the current systems. Thus, it will be necessary to put

into practice new resolution enhancing techniques that are applicable on long range systems.

- At the conclusion of the research stage of this thesis work, our research team got involved in an implementation project for the development of a Raman-assisted BOTDA field test equipment. That intention coincided with the fact that the spin-off company named Focus, created among research personnel from the Spanish National Research Council (CSIC) and the University of Alcalá (UAH), was granted with funding from the Entrepreneurs Fund of the Repsol Foundation in order to develop a pre-commercial long range distributed sensor prototype. Thus, since December 2012, I have been fully involved in the elaboration of a commercial Raman-assisted BOTDA system, that ranges 100 km with 2 meter resolution, which is currently fully operative doing the first monitoring tests over an oil pipeline departing from the Cartagena (Spain) petrol refinery property of Repsol.

Bibliography

[1] G. P. Agrawal, *Nonlinear Fiber Optics - 3rd Edition.* Academic Press, 2001.

[2] C. D. Heras-Vila, "Estudio de efectos ópticos no lineales en fibras monomodo. Medidas del índice de refracción no lineal," Ph.D. dissertation, Universidad de Zaragoza, 2003.

[3] E. G. Sauter, *Nonlinear Optics.* Wiley Interscience, 1996.

[4] S. Martin-Lopez, "Generación de supercontinuo en fibras ópticas monomodo con fuentes de bombeo continuo," Ph.D. dissertation, Universidad Complutense de Madrid, 2006.

[5] R. Paschotta, *Field Guide to Lasers.* Spiral Bound, 2008.

[6] E. G. Neumann, *Single-Mode Fibers.* Springer-Verlag, 1988.

[7] R. W. Boyd, *Nonlinear Optics - 3rd Edition.* Academic Press, 2008.

[8] M. Gonzalez-Herraez, "Desarrollo de técnicas no lineales para la medida de la distribución longitudinal de dispersión cromática en fibras ópticas monomodo," Ph.D. dissertation, Universidad Politécnica de Madrid, 2004.

[9] L. Thévenaz, Ed., *Advanced Fiber Optics - Concepts and Technology.* EPFL Press, 2011.

[10] I. L. Fabelinskii, *Molecular Scattering of Light.* Plenum Press, 1968.

[11] M. Facchini, "Distributed optical fiber sensors based on Brillouin scattering," Ph.D. dissertation, École Polytechnique Fédérale de Lausanne, 2002.

[12] M. J. Damzen, V. I. Vlad, V. Babin, and A. Mocofanescu, *Stimulated Brillouin Scattering: Fundamentals and Applications.* Institute of Physics Publishing, 2003.

[13] M. N. Islam, *Raman Amplifiers for Telecommunications I - Physical Principles.* Springer-Velag, 2004.

[14] M. A. Soto, "Advanced techniques for distributed optical fiber sensors based on Raman and Brillouin scattering," Ph.D. dissertation, Scuola Superiore Sant' Anna di Studi Universitari e di Perfezionamento, 2011.

[15] M. Niklés, "La diffusion Brillouin dans les fibres optiques: étude et application aux capteurs distribués," Ph.D. dissertation, École Polytechnique Fédérale de Lausanne, 1997.

[16] S. Foaleng-Mafang, "Brillouin echoes for advanced distributed sensing in optical fibres," Ph.D. dissertation, École Polytechnique Fédérale de Lausanne, 2011.

[17] M. O. van Deventer, "Polarization properties of stimulated Brillouin scattering in single-mode fibers," *J. Lightwave Technol.*, vol. 12, no. 4, pp. 585–590, 1994.

[18] R. G. Smith, "Optical power handling capacity of low loss optical fibers as determined by stimulated Raman and Brillouin scattering," *App. Optics*, vol. 11, no. 11, pp. 2489–2494, 1972.

[19] M. Niklés, L. Thévenaz, and P. A. Robert, "Brillouin gain spectrum characterization in single-mode optical fibers," *J. Lightwave Technol.*, vol. 15, no. 10, pp. 1842–1851, 1997.

[20] T. Horiguchi and M. Tateda, "BOTDA - Nondestructive measurement of single-mode optical fiber attenuation characteristics using Brillouin interaction: Theory," *J. Lightwave Technol.*, vol. 7, no. 8, pp. 1170–1176, 1989.

[21] ——, "Optical-fiber-attenuation investigation using stimulated Brillouin scattering between a pulse and a continuous wave," *Opt. Lett.*, vol. 14, no. 8, pp. 408–410, 1989.

[22] M. K. Barnoski and S. M. Jensen, "Fiber waveguides: a novel technique for investigating attenuation characteristics," *App. Optics*, vol. 15, no. 9, pp. 2112–2115, 1976.

[23] T. Kurashima, T. Horiguchi, and M. Tateda, "Distributed-temperature sensing using stimulated Brillouin scattering in optical silica fibers," *Opt. Lett.*, vol. 15, no. 18, pp. 1038–1040, 1990.

[24] T. Horiguchi, T. Kurashima, and M. Tateda, "A technique to measure distributed strain in optical fibers," *IEEE Photon. Technol. Lett.*, vol. 2, no. 5, pp. 352–354, 1990.

[25] X. Bao, D. J. Webb, and D. A. Jackson, "32-km distributed temperature sensor based on Brillouin loss in an optical fiber," *Opt. Lett.*, vol. 18, no. 18, pp. 1561–1563, 1993.

[26] ——, "Combined distributed temperature and strain sensor based on Brillouin loss in an optical fiber," *Opt. Lett.*, vol. 19, no. 2, pp. 141–143, 1994.

[27] Y. Dong, L. Chen, and X. Bao, "System optimization of a long-range Brillouin-loss-based distributed fiber sensor," *Appl. Opt.*, vol. 49, no. 27, pp. 5020–5025, 2010.

[28] X. Bao, J. Dhliwayo, N. Heron, D. J. Webb, and D. A. Jackson, "Experimental and theoretical studies on a distributed temperature sensor based on Brillouin scattering," *J. Lightwave Technol.*, vol. 13, no. 7, pp. 1340–1348, 1995.

[29] A. Minardo, R. Bernini, L. Zeni, L. Thévenaz, and F. Briffod, "A reconstruction technique for long-range stimulated Brillouin scattering distributed fibre-optic sensors: Experimental results," *Meas. Sci. Technol.*, vol. 16, no. 4, pp. 900–908, 2005.

[30] M. Niklés, "Fibre optic distributed scattering sensing system: Perspectives and challenges for high performance applications," presented at the Third European Workshop on Optical Fiber Sensors, 66190D, Italy, 2007.

[31] C. A. Galindez-Jamioy and J. M. Lopez-Higuera, "Brillouin distributed fiber sensors: An overview and applications," *Journal of Sensors*, vol. 2012, Article ID 204121, 17 pages, 2012.

[32] M. Niklés, L. Thévenaz, and P. A. Robert, "Simple distributed fiber sensor based on Brillouin gain spectrum analysis," *Opt. Lett.*, vol. 21, no. 10, pp. 758–760, 1996.

[33] F. Rodriguez-Barrios, S. Martin-Lopez, A. Carrasco-Sanz, P. Corredera, M. L. Hernanz, and M. Gonzalez-Herraez, "Raman-assisted distributed Brillouin sensor in optical fiber for strain and temperature monitoring in civil engineering applications," presented at the 9th International Symposium on Measurement Technology and Intelligent Instruments, San Petersburg, Russia, 2009.

[34] G. Meltz, W. W. Morey, and W. H. Glenn, "Formation of Bragg gratings in optical fibers by transverse holographic method," *Opt. Lett.*, vol. 14, no. 15, pp. 823–825, 1989.

[35] T. Kawanishi and M. Izutsu, "Linear single-sideband modulation for high-SNR wavelength conversion," *IEEE Photon. Technol. Lett.*, vol. 16, no. 6, pp. 1534–1536, 2004.

[36] M. Sagues, "Aplicaciones de la correspondencia entre el dominio óptico y eléctrico establecida por la modulación óptica en banda lateral única," Ph.D. dissertation, Universidad Pública de Navarra, 2009.

[37] A. Zornoza, M. Sagues, and A. Loayssa, "Self-heterodyne detection for SNR improvement and distributed phase-shift measurements in BOTDA," *J. Lightwave Technol.*, vol. 30, no. 8, pp. 1066–1072, 2012.

[38] D. M. Nguyen, B. Stiller, M. W. Lee, J. C. Beugnot, H. Maillotte, A. Mottet, J. Hauden, and T. Sylvestre, "Distributed Brillouin fiber sensor with enhanced sensitivity based on anti-Stokes single-sideband suppressed-carrier modulation," *IEEE Photon. Technol. Lett.*, vol. 25, no. 1, pp. 94–96, 2013.

[39] F. Rodriguez-Barrios, S. Martin-Lopez, A. Carrasco-Sanz, P. Corredera, J. D. Ania-Castañon, L. Thévenaz, and M. Gonzalez-Herraez, "Distributed Brillouin fiber sensor assisted by first-order Raman amplification," *J. Lightwave Technol.*, vol. 28, no. 15, pp. 2162–2172, 2010.

[40] M. A. Soto, G. Bolognini, F. D. Pasquale, and L. Thévenaz, "Simplex-coded BOTDA fiber sensor with 1 m spatial resolution over a 50 km range," *Opt. Lett.*, vol. 35, no. 2, pp. 259–261, 2010.

[41] X. Angulo-Vinuesa, S. Martin-Lopez, J. Nuño, P. Corredera, J. D. Ania-Castañon, L. Thévenaz, and M. Gonzalez-Herraez, "Hot spot detection over 100 km with 2 meter resolution in a Raman-assisted Brillouin distributed sensor," in *Proc. of SPIE Vol. 7753*, 2011, p. 775309.

[42] ——, "Raman-assisted Brillouin distributed temperature sensor over 100 km featuring 2 m resolution and 1.2 ^{o}C uncertainty," *J. Lightwave Technol.*, vol. 30, no. 8, pp. 1060–1065, 2012.

[43] X. Angulo-Vinuesa, S. Martin-Lopez, P. Corredera, and M. Gonzalez-Herraez, "100km BOTDA temperature sensor with sub-meter resolution," in *Proc. of SPIE Vol. 8421*, 2012, p. 842117.

[44] ——, "Raman-assisted Brillouin optical time-domain analysis with sub-meter resolution over 100 km," *Opt. Express*, vol. 20, no. 11, pp. 12 147–12 154, 2012.

[45] S. Martin-Lopez, M. Alcon-Camas, F. Rodriguez-Barrios, P. Corredera, J. D. Ania-Castañon, L. Thévenaz, and M. Gonzalez-Herraez, "Brillouin optical time-domain analysis assisted by second-order Raman amplification," *Opt. Express*, vol. 18, no. 18, pp. 18 769–18 778, 2010.

[46] X. Angulo-Vinuesa, M. A. Soto, S. Martin-Lopez, S. H. Chin, J. D. Ania-Castañon, P. Corredera, E. Rochat, M. Gonzalez-Herraez, and L. Thévenaz, "Brillouin optical time-domain analysis over a 240 km-long fiber loop with no repeater," in *Proc. of SPIE Vol. 8421*, 2012, p. 8421C9.

[47] M. A. Soto, X. Angulo-Vinuesa, S. Martin-Lopez, S. H. Chin, J. D. Ania-Castañon, P. Corredera, E. Rochat, M. Gonzalez-Herraez, and L. Thévenaz, "Extending the real remoteness of long-range Brillouin optical time-domain fiber analyzers," *J. Lightwave Technol.*, vol. 32, no. 1, pp. 152–162, 2014.

[48] M. A. Soto, G. Bolognini, F. D. Pasquale, and L. Thévenaz, "Long-range Brillouin optical time-domain analysis sensor employing pulse coding techniques," *Meas. Sci. Technol.*, vol. 21, no. 9, p. 094024, 2010.

[49] M. A. Soto, G. Bolognini, and F. D. Pasquale, "Optimization of long-range BOTDA sensors with high resolution using first-order bi-directional Raman amplification," *Opt. Express*, vol. 19, no. 5, pp. 4444–4457, 2011.

[50] M. A. Soto, M. Taki, G. Bolognini, and F. D. Pasquale, "Simplex-coded BOTDA sensor over 120-km SMF with 1-m spatial resolution assisted by optimized bidirectional Raman amplification," *IEEE Photon. Technol. Lett.*, vol. 36, no. 2, pp. 277–279, 2011.

[51] A. Hasegawa and K. Tai, "Effects of modulational instability on coherent transmission systems," *Opt. Lett.*, vol. 14, no. 10, pp. 512–514, 1989.

[52] M. N. Alahbadi, Y. T. Cho, T. P. Newson, P. C. Wait, and A. H. Hartog, "Influence of modulation instability on distributed optical fiber sensors based on spontaneous Brillouin scattering," *J. Opt. Soc. Am. B*, vol. 21, no. 6, pp. 1156–1160, 2004.

[53] H. F. Martins, S. Martin-Lopez, P. Corredera, P. Salgado, O. Frazao, and M. Gonzalez-Herraez, "Modulation instability-induced fading in phase-sensitive optical time-domain reflectometry," *Opt. Lett.*, vol. 38, no. 6, pp. 872–874, 2013.

[54] G. V. Simaeys, P. Emplit, and M. Haelterman, "Experimental demonstration of the Fermi-Pasta-Ulam recurrence in a modulationally unstable optical wave," *Phys. Rev. Lett.*, vol. 87, no. 3, p. 033902, 2001.

[55] D. Alasia, "Advanced trends in nonlinear optics applied to distributed optical-fibre sensors," Ph.D. dissertation, Ecole Polytechnique Fédérale de Lausanne, 2006.

[56] D. Alasia, M. Gonzalez-Herraez, L. Abrardi, S. Martin-Lopez, and L. Thévenaz, "Detrimental effect of modulation instability on distributed optical fibre sensors using stimulated Brillouin scattering," in *Proc. of SPIE Vol. 5855*, 2005, pp. 587–590.

[57] G. V. Simaeys, P. Emplit, and M. Haelterman, "Experimental study of the reversible behavior of modulational instability in optical fibers," *J. Opt. Soc. Am. B*, vol. 19, no. 3, pp. 477–486, 2002.

[58] T. Horiguchi, K. Shimizu, M. T. T. Kurashima and, and Y. Koyamada, "Development of a distributed sensing technique using Brillouin scattering," *J. Lightwave Technol.*, vol. 13, no. 7, pp. 1296–1302, 1995.

[59] E. Geinitz, S. Jetschke, U. Röpke, S. Schröter, R. Willsch, and H. Bartelt, "The influence of pulse amplification on distributed fibre-optic Brillouin sensing and a method to compensate for systematic errors," *Meas. Sci. Technol.*, vol. 10, no. 2, pp. 112–116, 1999.

[60] A. Minardo, R. Bernini, and L. Zeni, "A simple technique for reducing pump depletion in long-range distributed Brillouin fiber sensors," *IEEE Sensors J.*, vol. 9, no. 6, pp. 633–634, 2009.

[61] Q. Cui, S. Pamukcu, A. Lin, W. Xiao, and J. Toulouse, "Performance of double sideband modulated probe wave in BOTDA distributed fiber sensor," *Microw. Opt. Technol. Lett.*, vol. 52, no. 12, pp. 2713–2717, 2010.

[62] L. Thévenaz, S. Foaleng-Mafang, and J. Lin, "Effect of pulse depletion in a Brillouin optical time-domain analysis system," *Opt. Express*, vol. 21, no. 12, pp. 14 017–14 035, 2013.

[63] S. Foaleng-Mafang and L. Thévenaz, "Impact of Raman scattering and modulation instability on the performances of Brillouin sensors," in *Proc. of SPIE Vol. 7753*, 2011, p. 77539V.

[64] Y. T. Cho, M. N. Alahbadi, M. J. Gunning, and T. P. Newson, "50-km single-ended spontaneous-Brillouin-based distributed-temperature sensor exploiting pulsed Raman amplification," *Opt. Lett.*, vol. 28, no. 18, pp. 1651–1653, 2003.

[65] ——, "Enhanced performance of long range Brillouin intensity based temperature sensors using remote Raman amplification," *Meas. Sci. Technol.*, vol. 15, no. 8, pp. 1548–1552, 2004.

[66] M. N. Alahbadi, Y. T. Cho, and T. P. Newson, "100 km distributed temperature sensor based on coherent detection of spontaneous Brillouin backscatter," *Meas. Sci. Technol.*, vol. 15, no. 8, pp. 1544–1548, 2004.

[67] ——, "150-km-range distributed temperature sensor based on coherent detection of spontaneous Brillouin backscatter and in-line Raman amplification," *J. Opt. Soc. Am. B*, vol. 22, no. 6, pp. 1321–1324, 2005.

[68] J. D. Ania-Castañon, "Quasi-lossless transmission using second-order Raman amplification and fibre Bragg gratings," *Opt. Express*, vol. 12, no. 19, pp. 4372–4377, 2004.

[69] D. E. McCumber, "Intensity fluctuations on the output of CW laser oscillator," *Phys. Rev. Lett.*, vol. 141, no. 1, pp. 306–322, 1966.

[70] C. R. S. Fludger, V. Handerek, and R. J. Mears, "Pump to signal RIN transfer in Raman fiber amplifiers," *J. Lightwave Technol.*, vol. 19, no. 8, pp. 1140–1148, 2001.

[71] R. H. Stolen and E. P. Ippen, "Raman gain in glass optical waveguides," *Appl. Phys. Lett.*, vol. 22, no. 6, pp. 276–278, 1973.

[72] J. Bromage, "Raman amplification for fiber communications systems," *J. Lightwave Technol.*, vol. 22, no. 1, pp. 79–93, 2004.

[73] M. Alcon-Camas and J. D. Ania-Castañon, "RIN transfer in 2nd-order distributed amplification with ultralong fiber lasers," *Opt. Express*, vol. 18, no. 23, pp. 23 569–23 575, 2010.

[74] B. Bristiel, S. Jiang, P. Gallion, and E. Pincemin, "New model of noise figure and RIN transfer in fiber Raman amplifiers," *IEEE Photon. Technol. Lett.*, vol. 18, no. 8, pp. 980–982, 2006.

[75] V. Kalavally, I. D. Rukhlenko, M. Premaratne, and T. Win, "Analytical study of RIN transfer in pulse-pumped Raman amplifiers," *J. Lightwave Technol.*, vol. 27, no. 20, pp. 4536–4543, 2009.

[76] P. S. Moharir and A. Selvarajan, "Optical Barker codes," *Electron. Lett.*, vol. 10, no. 9, pp. 154–155, 1974.

[77] M. D. Jones, "Using Simplex codes to improve OTDR sensitivity," *IEEE Photon. Technol. Lett.*, vol. 15, no. 7, pp. 822–824, 1993.

[78] D. Lee, H. Yoon, P. Kim, J. Park, and N. Park, "Optimization of SNR improvement in the noncoherent OTDR based on Simplex codes," *J. Lightwave Technol.*, vol. 24, no. 1, pp. 322–328, 2006.

[79] M. A. Soto, G. Bolognini, and F. D. Pasquale, "Enhanced simultaneous distributed strain and temperature fiber sensor employing spontaneous Brillouin scattering and optical pulse coding," *IEEE Photon. Technol. Lett.*, vol. 21, no. 7, pp. 450–452, 2009.

[80] D. Lee, H. Yoon, N. Y. Kim, H. Lee, and N. Park, "Analysis and experimental demonstration of Simplex coding technique for SNR enhancement of OTDR," presented at the Lightwave Technologies in Instrumentation and Measurement Conference, 2004.

[81] M. A. Soto and L. Thévenaz, "Modeling and evaluating the performance of Brillouin distributed optical fiber sensors," *Opt. Express*, vol. 21, no. 25, pp. 31 347–31 366, 2013.

[82] W. Li, X. Bao, Y. Li, and L. Chen, "Differential pulse-width pair BOTDA for high spatial resolution sensing," *Opt. Express*, vol. 16, no. 26, pp. 21 616–21 625, 2008.

[83] A. Fellay, L. Thévenaz, M. Facchini, M. Niklés, and P. Robert, "Distributed sensing using stimulated Brillouin scattering: Towards ultimate resolution," presented at the 12th International Conference on Optical Fiber Sensors, 1997.

[84] S. Foaleng-Mafang, F. Rodriguez-Barrios, S. Martin-Lopez, M. Gonzalez-Herraez, and L. Thévenaz, "Detrimental effect of self-phase modulation on the performance of Brillouin distributed fiber sensors," *Opt. Lett.*, vol. 36, no. 2, pp. 97–99, 2011.

[85] V. Lecoeuche, D. J. Webb, C. N. Pannell, and D. A. Jackson, "25 km Brillouin based single-ended distributed fibre sensor for threshold detection of temperature or strain," *Opt. Commun.*, vol. 168, no. 1-4, pp. 95–102, 1999.

[86] H. Izumita, Y. Koyamada, S. Furukawa, and I.Sankawa, "The performance limit of coherent OTDR enhanced with optical fiber amplifiers due to optical nonlinear phenomena," *J. Lightwave Technol.*, vol. 12, no. 7, pp. 1230–1238, 1994.

[87] A. Minardo, R. Bernini, and L. Zeni, "Differential techniques for high-resolution BOTDA: An analytical approach," *IEEE Photon. Technol. Lett.*, vol. 24, no. 15, pp. 1295–1297, 2012.

[88] A. W. Brown, B. G. Colpitts, and K. Brown, "Dark-pulse Brillouin optical time-domain sensor with 20-mm spatial resolution," *J. Lightwave Technol.*, vol. 25, no. 1, pp. 381–386, 2007.

[89] K. Y. Song, S. Chin, N. Primerov, and L. Thévenaz, "Time-domain distributed fiber sensor with 1 cm spatial resolution based on Brillouin dynamic grating," *J. Lightwave Technol.*, vol. 28, no. 14, pp. 2062–2067, 2010.

[90] C. A. Galindez-Jamioy and J. M. Lopez-Higuera, "Decimeter spatial resolution by using differential preexcitation BOTDA pulse technique," *IEEE Sensors J.*, vol. 11, no. 10, pp. 2344–2348, 2011.

[91] L. Thévenaz and S. Foaleng-Mafang, "Distributed fiber sensing using Brillouin echoes," in *Proc. of SPIE Vol. 7004*, 2008, p. 70043N4.

[92] J. C. Beugnot, M. Tur, S. Foaleng-Mafang, and L. Thévenaz, "Distributed Brillouin sensing with sub-meter spatial resolution: Modeling and processing," *Opt. Express*, vol. 19, no. 8, pp. 7381–7397, 2011.

[93] S. Foaleng-Mafang, J. C. Beugnot, and L. Thevenaz, "Optimized configuration for high-resolution distributed sensing using Brillouin echoes," in *Proc. of SPIE Vol. 7503*, 2009.

[94] A. Minardo, R. Bernini, and L. Zeni, "Numerical analysis of single pulse and differential pulse-width pair BOTDA systems in the high spatial resolution regime," *Opt. Express*, vol. 19, no. 20, pp. 19 233–19 244, 2011.

[95] A. Minardo, L. Zeni, and R. Bernini, "Differential pulse-width pair BOTDA with fast fall-time pulses," 2011.

[96] R. G. Hunsperger, *Integrated Optics: Theory and Technology*. Springer, 2009.

[97] S. Yang and X. Bao, "High extinction ratio pulse generation from FM modulated signal by using dispersion imbalanced fiber loop mirror," presented at the Optical Fiber Communication Conference, 2006.

[98] N. J. Doran and D. Wood, "Nonlinear-optical loop mirror," *Opt. Lett.*, vol. 13, no. 1, pp. 56–58, 1988.

[99] N. P. Barnes and B. M. Walsh, "Amplified spontaneous emission-application to Nd:YAG lasers," *IEEE J. Quantum Electron.*, vol. 35, no. 1, pp. 101–109, 1999.

[100] K. J. Aaström and T. Hägglund, *PID Controllers: Theory, Design, and Tuning*. ISA, 1995.

[101] J. Wu, Y. Li, C. Lou, and Y. Gao, "Optimization of pulse compression with an unbalanced nonlinear optic mirror," *Opt. Commun.*, vol. 180, no. 1-3, pp. 43–47, 2000.

[102] A. Zadok, A. Eyal, M. Tur, and L. Thévenaz, "Polarization attributes of stimulated Brillouin scattering slow light in fiber," in *Proc. of SPIE Vol. 7949*, 2011, p. 79490A1.

[103] Y. Dong, L. Chen, and X. Bao, "Extending the sensing range of Brillouin optical time-domain analysis combining frequency-division multiplexing and in-line EDFAs," *J. Lightwave Technol.*, vol. 30, no. 8, pp. 1161–1167, 2012.

[104] D. M. Nguyen, B. Stiller, M. W. Lee, J. C. Beugnot, H. Maillotte, and T. Sylvestre, "Sensitivity enhancement in long-range distributed Brillouin fiber sensor using an anti-Stokes single-sideband probe and a bidirectional EDFA," pp. 1–4, 2012.

[105] M. A. Soto, S. L. Floch, and L. Thévenaz, "Bipolar optical pulse coding for performance enhancement in BOTDA sensors," *Opt. Express*, vol. 21, no. 14, pp. 16 390–16 397, 2013.

[106] S. Faralli, G. Bolognini, G. Sacchi, S. Sugliani, and F. D. Pasquale, "Bidirectional higher order cascaded Raman amplification benefits for 10-Gb/s WDM unrepeated transmission systems," *J. Lightwave Technol.*, vol. 23, no. 8, pp. 2427–2433, 2005.

[107] S. Faralli, G. Bolognini, M. A. Andrade, and F. D. Pasquale, "Unrepeated WDM transmission systems based on advanced first-order and higher order Raman-copumping technologies," *J. Lightwave Technol.*, vol. 25, no. 11, pp. 3519–3527, 2007.

[108] M. A. Soto, G. Bolognini, and F. D. Pasquale, "Long-range simplex-coded BOTDA sensor over 120 km distance employing optical preamplification," *Opt. Lett.*, vol. 36, no. 2, pp. 232–234, 2011.

[109] X. H. Jia, Y. J. Rao, K. Deng, Z. X. Yang, L. Chang, C. Zhang, and Z. L. Ran, "Experimental demonstration on 2.5-m spatial resolution and 1°C temperature uncertainty over long-distance BOTDA with combined Raman amplification and optical pulse coding," *IEEE Photon. Technol. Lett.*, vol. 23, no. 7, pp. 435–437, 2011.

[110] D. J. Morris, *Pulse Code Formats for Fiber Optical Data Communication.* CRC Press, 1983.

[111] M. A. Soto, G. Bolognini, and F. D. Pasquale, "Analysis of pulse modulation format in coded BOTDA sensors," *Opt. Express*, vol. 18, no. 14, pp. 14 878–14 892, 2010.

[112] X. Angulo-Vinuesa, D. Bacquet, S. Martin-Lopez, P. Corredera, P. Szriftgiser, and M. Gonzalez-Herraez, "Raman-assisted vector Brillouin optical time domain analysis," in *Proc. of SPIE Vol. 8794*, 2013, p. 87943A.

[113] ——, "Relative Intensity Noise transfer reduction in Raman-assisted BOTDA systems," *IEEE Photon. Technol. Lett.*, vol. 26, no. 3, pp. 271–274, 2014.

[114] M. Dossou, D. Bacquet, and P. Szriftgiser, "Vector Brillouin optical time-domain analyzer for high-order acoustic modes," *Opt. Lett.*, vol. 35, no. 22, pp. 3850–3852, 2010.

[115] A. Loayssa, R. Hernández, D. Benito, and S. Galech, "Characterization of stimulated Brillouin scattering spectra by use of optical single-sideband modulation," *Opt. Lett.*, vol. 29, no. 6, pp. 638–640, 2004.

[116] Y. Antman, N. Primerov, J. Sancho, L. Thevenaz, and A. Zadok, "Localized and stationary dynamic gratings via stimulated Brillouin scattering with phase modulated pumps," *Opt. Express*, vol. 20, no. 7, pp. 7807–7821, 2012.

[117] Y. Peled, A. Motil, L. Yaron, and M. Tur, "Slope-assisted fast distributed sensing in optical fibers with arbitrary Brillouin profile," *Opt. Express*, vol. 19, no. 21, pp. 19 845–19 854, 2011.

[118] J. Urricelqui, A. Zornoza, M. Sagues, and A. Loayssa, "Dynamic BOTDA measurements based on Brillouin phase-shift and RF demodulation," *Opt. Express*, vol. 20, no. 24, pp. 26 942–26 949, 2012.

[119] Y. Peled, A. Motil, and M. Tur, "Fast Brillouin optical time domain analysis for dynamic sensing," *Opt. Express*, vol. 20, no. 8, pp. 8584–8591, 2012.

[120] J. Urricelqui, M. Sagues, and A. Loayssa, "BOTDA measurements tolerant to non-local effects by using a phase-modulated probe wave and RF demodulation," *Opt. Express*, vol. 21, no. 4, pp. 17 186–17 194, 2013.

[121] M. J. Conelly, *Semiconductor Optical Amplifiers.* Kluwer Academic press, 2002.

[122] W. K. Marshall, B. Crosignani, and A. Yariv, "Laser phase noise to intensity noise conversion by lowest-order group-velocity dispersion in optical fiber: Exact theory," *Opt. Lett.*, vol. 25, no. 3, pp. 165–167, 2000.

[123] O. Aso, M. Tadakuma, and S.Namiki, "Four-wave mixing in optical fibers and its applications," *Furukawa Review*, vol. 19, pp. 63–68, 2000.

[124] K. Inoue, "Four-Wave Mixing in an optical fiber in the zero-dispersion wavelength region," *J. Lightwave Technol.*, vol. 10, pp. 1553–1561, 1992.

Appendix A

List of Symbols

Symbol	Physical Meaning	Units
α	*Fiber Attenuation*	dB/km or km^{-1}
β	*Fiber Propagation Constant*	m^{-1}
β_1	*Group Velocity Inverse*	ps/km
β_2	*Group Velocity Dispersion*	ps^2/km
γ	*Nonlinear Constant*	1/W·km
ϵ, ϵ_0	*Electric Permittivity in the Medium, in Vacuum*	F/m
λ	*Wavelength*	nm
λ_0	*Zero Dispersion Wavelength*	nm
ν_B	*Brillouin Frequency Shift*	GHz
τ_g	*Group Delay*	ps
ω	*Angular Frequency*	rad/s
$\Delta\epsilon$	*Strain Difference*	MHz/%
$\Delta\nu_B$	*FWHM of the Brillouin Spectral Linewidth*	MHz
ΔT	*Temperature Difference*	MHz/°C
$\chi^{(i)}$	*Linear/Non-Linear Susceptibility*	$(m/V)^{i-1}$
A_{eff}	*Effective Area*	μm^2
c	*Speed of Light in Vacuum*	m/s
$C_{\nu_B\epsilon}$	*Strain-Frequency Conversion Constant*	MHz/%
$C_{\nu_B T}$	*Temperature-Frequency Conversion Constant*	MHz/°C
g_B	*Brillouin Gain*	m/W
g_R	*Raman Gain*	m/W
L	*Length*	km
L_{eff}	*Effective Length*	km
n	*Refractive Index*	-
n_2	*Non-linear Refractive Index*	-
P	*Optical Power*	dBm or mW
v_a	*Acoustic Velocity*	m/s
v_g	*Group Velocity*	m/s

Appendix B

List of Acronyms

Acronym	Meaning
AM	*Amplitude-Modulated*
AOM	*Acousto Optic Modulator*
ASE	*Amplified Spontaneous Emission*
BFS	*Brillouin Frequency Shift*
BGS	*Brillouin Gain Spectrum*
BOTDA	*Brillouin Optical Time Domain Analysis*
BPS	*Brillouin Phase Shift*
CSIC	*Spanish National Research Council*
CW	*Continuous Wave*
DC	*Direct Current*
DPP	*Differential Pulse-width Pair*
EDFA	*Erbium Doped Fiber Amplifier*
EOM	*Electro Optic Modulator*
EPFL	*École Polytechnique Fédérale de Lausanne*
ER	*Extinction Ratio*
ESA	*Electrical Spectrum Analyzer*
FBG	*Fiber Bragg Grating*
FFT	*Fast Fourier Transform*
FL	*Fiber Laser*
FPU	*Fermi-Pasta-Ulam*
FUT	*Fiber Under Test*
FWHM	*Full-Width at Half Maximum*
FWM	*Four-Wave Mixing*

Acronym	Meaning
GFO	*Group for Fiber Optics*
I&T	*Current and Temperature*
LD	*Laser Diode*
MI	*Modulation Instability*
NLSE	*Non-Linear Schrödinger's Equation*
NOLM	*Non-linear Optical Loop Mirror*
OTDR	*Optical Time Domain Reflectometry*
OVA	*Optical Vector Analyzer*
PC	*Polarization Controller*
PDG	*Polarization Dependent Gain*
PhLAM	*Laboratoire de Physique des Lasers, Atomes et Molécules*
PI	*Proportional-Integrator*
PM-AM	*Phase to Amplitude Modulation*
PS	*Polarization Scrambler*
PSW	*Polarization Switch*
RF	*Radio Frequency*
RFL	*Raman Fiber Laser*
RFS	*Raman Frequency Shift*
RIN	*Relative Intensity Noise*
RMS	*Root Mean Square*
RZ	*Return-to-Zero*
SBR	*Signal to Background Ration*
SBS	*Stimulated Brillouin Scattering*
SL	*Semiconductor Laser*
SMF	*Single Mode Fiber*
SNR	*Signal to Noise Ratio*
SOA	*Semiconductor Optical Amplifier*
SPM	*Self-Phase Modulation*
SRS	*Stimulated Raman Scattering*
S-codes	*Simplex Codes*
UAH	*University of Alcalá*
VBOTDA	*Vector-BOTDA*
VOA	*Variable Optical Attenuator*
WDM	*Wavelength Division Multiplexing*